

Superstructure Optimization with Embedded Neural Networks for Sustainable Aviation Fuel Production

Alexander Klimek^a, Christoph Plate^{bc}, Sebastian Sager^{bc}, Kai Sundmacher^{ad}, and Caroline Ganzer^{*a}

^aMax Planck Institute for Dynamics of Complex Technical Systems, Department of Process Systems Engineering, Sandtorstr. 1, 39106 Magdeburg, Germany.

^bMax Planck Institute for Dynamics of Complex Technical Systems, Mathematical Optimization and Machine Learning Group, Sandtorstr. 1, 39106 Magdeburg, Germany.

^cOtto von Guericke University, Chair of Mathematical Algorithmic Optimization, Universitätsplatz 2, 39106 Magdeburg, Germany.

^dOtto von Guericke University, Chair for Process Systems Engineering, Universitätsplatz 2, 39106 Magdeburg, Germany.

* corresponding author; E-mail: cganzer@mpi-magdeburg.mpg.de

ABSTRACT

This study presents a multi-objective optimization framework for sustainable aviation fuel (SAF) production, integrating artificial neural networks (ANNs) within a mixed-integer quadratically constrained programming (MIQCP) formulation. By embedding data-driven surrogate models into the mathematical optimization structure, the proposed methodology addresses key limitations of conventional superstructure-based approaches, enabling simultaneous optimization of discrete process choices and continuous operating parameters. The framework captures variable input and output stream compositions, facilitating the joint optimization of target product composition and system design. Application to Fischer-Tropsch (FT) kerosene production demonstrates that cost-minimizing configurations under unconstrained CO₂ emissions are dominated by the fossil-based autothermal reforming (ATR) route. Imposing carbon emission constraints necessitates the integration of biomass gasification and direct air capture coupled with carbon sequestration (DAC-CS), resulting in substantially reduced net emissions but higher production costs. At the zero-emission limit, hybrid configurations combining ATR and biomass gasification achieve the lowest costs (~2.38 \$/kg_{kerosene}), followed closely by biomass gasification-only (~2.43 \$/kg), both of which outperform the ATR-only pathway with DAC-CS (~2.65 \$/kg). In contrast, DAC-only systems relying exclusively on atmospheric CO₂ and water electrolysis are prohibitively expensive (~10.8 \$/kg). The results highlight the critical role of process adaptability: configurations exploiting flexible process parameters, facilitated by embedded ANNs, consistently outperform fixed setups, achieving up to 20 % cost savings. Sensitivity analyses elucidate the influence of process conditions, such as FT reactor pressure and gasification temperature, on economic and environmental performance.

Keywords: Sustainable Aviation Fuel, Superstructure Optimization, Surrogate Modeling, Artificial Neural Networks

1 Introduction

The defossilization of aviation represents a formidable challenge in the global transition toward net zero greenhouse gas (GHG) emissions. In 2019, civil aviation was responsible for over 900 million metric tons of CO₂-equivalent emissions, accounting for approximately 10 % of global transportation-related emissions.¹ Forecasts anticipate a four- to six-fold increase in air traffic over the coming decades, driven by population growth, urbanization, and globalization.^{2,3} Whilst H₂-fueled aircrafts and electrification may present viable options at small scale and for niche applications, it is expected that long-chain liquid sustainable aviation fuels (SAFs) are crucial at large scale.⁴

SAFs are hydrocarbon-based fuels synthesized from renewable carbon (C) and H₂ sources via certified thermochemical or biochemical conversion pathways. Unlike alternative propulsion technologies, SAFs are compatible with existing aircraft engines, fuel handling systems, and airport infrastructure. As such, they can serve as drop-in replacements for conventional jet fuels (e.g., Jet-A1), facilitating a smoother and less disruptive transition to low-carbon aviation. The American Society for Testing and Materials (ASTM) International has codified the production and compositional criteria for SAFs under Standard D7566, with multiple conversion pathways such as Fischer-Tropsch Synthetic Paraffinic Kerosene (FT-SPK), Hydroprocessed Esters and Fatty Acids (HEFA-SPK), and Alcohol-to-Jet Synthetic Paraffinic Kerosene (ATJ-SPK) having already received certification for commercial deployment.^{2,5,6}

However, the design of economically and environmentally optimal SAF production pathways remains a multi-dimensional optimization problem. This complexity arises from the wide array of feasible raw material sources, including biomass, captured CO₂, and renewable H₂, as well as the multiplicity of intermediate chemistries (e.g., syngas, methanol, FT liquids) and energy integration schemes.⁷ These process network synthesis problems are further complicated by nonlinear thermodynamic relationships, discrete design choices, and sustainability constraints such as CO₂ emissions and land use. Identifying viable SAF production configurations requires a systematic modeling approach that accounts for process interdependencies and interactions among material and energy flows as well as emissions.³

Recent techno-economic analyses have assessed various power-to-liquid production routes, revealing significant cost disparities and efficiency trade-offs. For instance, Salem⁸ emphasizes the wide cost range of methanol-to-jet (MtJ) pathways (650 € to 4,630 € per tonne) primarily driven by the price of H₂ and CO₂. Sacchi et al.⁹ present a time-dependent life-cycle assessment comparing fossil jet fuel with DAC-CS offsets to synthetic jet fuel from DAC and electrolysis. They show that climate outcomes depend strongly on the carbon footprint of electricity, with synthetic fuels reducing CO₂ storage needs if powered by low-carbon electricity. Do et al.¹⁰ develop a techno-economic framework to evaluate CO₂-to-fuel pathways, including aviation fuels, using process simulation and optimization to assess various technologies and scenarios. Meanwhile, Albrecht et al.¹¹ demonstrate that the viability of different SAF pathways depends heav-

ily on electricity prices, with biomass-to-liquid favored under higher electricity prices. Comparative studies by Bube et al.^{7,12} and Voß et al.¹³ indicate that MtJ offers higher kerosene selectivity and lower energy input, while hybrid routes based on biomass and electrolytic H₂ achieve higher C efficiency at a premium cost. Eyberg et al.¹⁴ underline the persistent economic gap with fossil jet fuel, suggesting that policy support and technological advancements will be pivotal.

A growing body of research has applied optimization-based approaches to the design and integration of SAF production pathways, adopting a variety of system boundaries and modeling strategies. Gonzalez-Garay et al.³ formulate a superstructure optimization of solar-powered SAF production based on Aspen Plus®¹⁵ simulations, using fixed operating conditions and lumped component modeling. Demirhan et al.¹⁶ develop a multi-scale optimization framework for fuels, chemicals, and power generation, incorporating multiple H₂ production routes and policy incentives. Martín and Grossmann¹⁷ and Zhang et al.¹⁸ analyze renewable fuels and power integration in Spain using linear models with temporal discretization. Kenkel et al.¹⁹ integrate Power-to-Jet and Biomass-to-Jet production in a refinery superstructure including algae-based feedstocks, while Restrepo-Flórez and Maravelias²⁰ extend ethanol upgrading studies with a richer representation of fuel components and property constraints. Niziolek et al.²¹ examine municipal solid waste conversion to fuels and chemicals via a broad reaction network, and Wu et al.²² present a systematic representation framework for process superstructures based on unit-port connectivity. Finally, Wang et al.²³ propose a multiobjective Mixed-Integer Nonlinear Programming (MINLP) model for biomass gasification-based hydrocarbon biorefineries, integrating economic and environmental criteria. Across all these studies, simplifications are common in the treatment of component mixtures, operating conditions, and carbon management. Most approaches rely on lumped components and linear process models, fixed operating parameters, and predetermined stream compositions. Limited consideration of biomass, atmospheric carbon, and carbon capture further restricts flexibility in design. As a result, opportunities remain to advance modeling frameworks that incorporate nonlinear process behavior, detailed mixture representations, variable operating conditions, broader feedstock options, and emissions management strategies to more fully capture the trade-offs in SAF production.

Surrogate modeling has become a vital tool in chemical process engineering, especially for enabling tractable optimization of complex systems. As summarized by McBride and Sundmacher,²⁴ commonly used surrogate models include polynomials, Gaussian processes (Kriging), ANNs, and radial basis functions. While Kriging dominates surrogate-based optimization studies, ANNs are increasingly used for high-dimensional, nonlinear problems. Surrogates are typically trained via sequential data generation from simulation platforms such as Aspen Plus®.¹⁵ Several studies have explored the integration of surrogate models into superstructure or flowsheet optimization. Fahmi and Cremaschi²⁵ embed ANNs trained on Aspen Plus®¹⁵ simulation data in a superstructure to optimize a biodiesel production, modeling complex process behaviors like conversion and utility demand. Their disjunctive programming formulation leads to a MINLP

solved efficiently in GAMS. Similarly, Henao and Maravelias²⁶ propose a generalized framework for surrogate-based superstructure optimization, replacing detailed unit models with ANNs. They emphasize the importance of sampling strategy, surrogate architecture, and variable selection, demonstrating optimization of CO₂ capture, distillation, and reaction systems using full-space ANN formulations in GAMS. To address scalability, Schweidtmann and Mitsos²⁷ develop a deterministic global optimization method using McCormick relaxations within reduced-space ANN formulations. This reduces optimization complexity significantly by avoiding explicit representation of ANN internals, a concept further elaborated by Schweidtmann et al.,²⁸ who distinguish between full-space and reduced-space formulations for embedding machine learning models in optimization tasks. These approaches show that deep ANNs, while accurate, increase computational cost unless an appropriate problem reformulation is applied. Granacher et al.²⁹ integrate ANNs, random forests, and Gaussian process surrogates within an active learning loop to optimize biomass-to-liquid process flowsheets. Complementary studies include Pedrozo et al.,³⁰ who used piecewise linear surrogates refined iteratively for ethylene production technology screening, and Hao et al.,³¹ who trained ANNs to replace carbon capture and utilization subsystem simulations, leading to faster multi-objective optimization. For a comprehensive literature overview regarding the mathematical complexity of embedding surrogate models in optimization problems, the reader is referred to Plate et al.³² In summary, the literature reveals a growing maturity in surrogate-assisted optimization frameworks. Still, challenges persist in ensuring optimization feasibility outside training domains, choosing appropriate surrogate architectures, and balancing model accuracy with computational tractability, particularly in complex flowsheet and SAF-related systems.

Superstructure optimization provides a rigorous mathematical framework for the identification of optimal SAF production routes from both an economic and environmental perspective. All potentially feasible processes and interconnections are embedded into a comprehensive network representation. The optimal design is then determined by solving an optimization problem, typically a Mixed-Integer Linear or Nonlinear Programming (MILP/MINLP) problem. However, conventional formulations often rely on oversimplified assumptions, such as treating streams as pure components, neglecting composition-dependent behavior, or linearizing inherently nonlinear phenomena.^{3,16,21,33,34} These approximations are particularly limiting for SAF synthesis, where product quality (defined by distributions of hydrocarbon chain lengths) and conversions are strongly composition-dependent.⁶

To address these limitations, we propose an advanced superstructure optimization framework. We explicitly model mixtures within the superstructure by including mass fractions as decision variables. Our formulation yields a Mixed-Integer Quadratically Constrained Programming (MIQCP) problem. Importantly, this structure remains compatible with global optimization using modern solvers such as Gurobi.³⁵ A key innovation of this work is the integration of artificial neural networks (ANNs) as surrogate models within the superstructure optimization. These embedded ANNs are trained on flowsheet simulations and capture

the nonlinear dependence of characteristic process variables, such as selectivity, conversion, and energy demand, as a function of operating conditions and inlet compositions. The primary contributions of this study can be summarized as follows:

- development of a novel MIQCP-based superstructure formulation that incorporates stream compositions and enables the optimization of mass fractions across processes,
- embedding of ANNs into the optimization problem to model nonlinear process behavior and include operating conditions as decision variables,
- application of the optimization framework to FT-based SAF production,
- demonstration that allowing greater degrees of freedom at the unit operation level, enabled through neural network surrogates, leads to superior overall system performance in terms of cost and CO₂ intensity.

The remainder of this paper is structured as follows. In Section 2, we introduce the complete MIQCP superstructure optimization formulation. The specific components and processes involved, including a description of detailed flowsheet simulations, for applying the novel optimization formulation are described in Section 3. Section 4 provides a comprehensive description of the training of ANNs, and their subsequent integration into the overarching superstructure optimization framework. Section 5 presents the results of the study, and the last section concludes with key findings and avenues for future work.

2 Superstructure optimization with mixtures

Figure 1 presents the generalized formulation adopted for modeling all processes within the superstructure network through the explicit definition of multiple inlet and outlet ports. This framework facilitates the integration of surrogate models, specifically ANNs, which are employed to capture the complex, nonlinear input–output relationships characteristic of steady-state process flowsheets. These ANNs are capable of describing the transformation of multiple chemical species entering the processes via distinct inlets and exiting through multiple outlet streams. Our framework is thus an extension of the underlying approaches by Ganzer and Mac Dowell³³ as well as Svitnič and Sundmacher.³⁴ Key innovations of our framework include:

- explicit consideration of multiple process inlet and outlet ports, enabling flexible representation of the connections between processes,
- representing streams as mixtures allowing for the optimization of compositions,
- integration of ANN-based surrogate models, thereby mapping nonlinear process behaviors while maintaining computational tractability.

The mathematical expressions used to formulate the MIQCP model are explained in detail below, with processes denoted by the index j , components by α , and inlet/outlet ports by i/o .

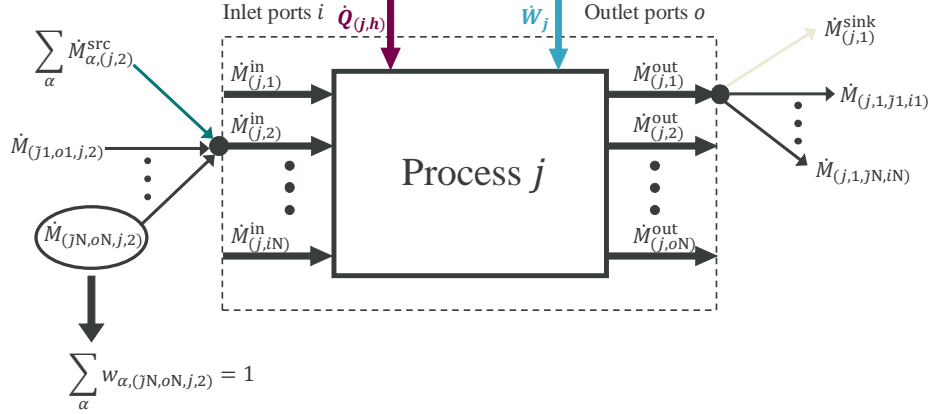


Figure 1 General modeling of all processes within the superstructure network. Each process is characterized by inlet and outlet ports through which mass flows can enter and exit the process. The general number of inlet or outlet ports is denoted by N. A process can contain several unit operations (e.g., compression, heating, reaction, separation). The process boundaries are indicated with solid lines, while the boundaries for balancing the inlet and outlet ports are shown with dashed lines.

2.1 Mass balance constraints

We establish generalized total mass balance equations for each inlet port (j, i) associated with every process in the superstructure network, expressed as:

$$\dot{M}_{(j,i)}^{\text{in}} = \sum_{(\tilde{j},o):(\tilde{j},o,j,i) \in \mathcal{J}^{\text{OI}}} \dot{M}_{(\tilde{j},o,j,i)} + \sum_{\alpha \in \mathcal{C}} \dot{M}_{\alpha,(j,i)}^{\text{src}} \quad \forall (j,i) \in \mathcal{J}^{\text{I}}, \quad (1)$$

as depicted in Figure 1. In this formulation, $\dot{M}_{(j,i)}^{\text{in}}$ denotes the total mass flow rate entering inlet port i of process j . The term $\dot{M}_{(\tilde{j},o,j,i)}$ refers to the mass flow rate transferred from outlet port o of process \tilde{j} to the specified inlet port (j, i) . External source contributions (i.e., mass inputs entering the system boundary) are represented by $\dot{M}_{\alpha,(j,i)}^{\text{src}}$, where α indexes the set of all species \mathcal{C} . The set \mathcal{J}^{OI} encompasses all admissible outlet-to-inlet port connections across the superstructure network, while \mathcal{J}^{I} defines the collection of all process inlet ports. A comprehensive overview of all sets involved in the formulation is provided in the Supplementary Information. Component-wise (partial) mass balances are additionally imposed for each process inlet port (j, i) , formulated as

$$w_{\alpha,(j,i)}^{\text{in}} \dot{M}_{(j,i)}^{\text{in}} = \sum_{(\tilde{j},o):(\tilde{j},o,j,i) \in \mathcal{J}^{\text{OI}}} w_{\alpha,(\tilde{j},o,j,i)} \dot{M}_{(\tilde{j},o,j,i)} + \dot{M}_{\alpha,(j,i)}^{\text{src}} \quad \forall (j,i) \in \mathcal{J}^{\text{I}}, \alpha \in \mathcal{C}, \quad (2)$$

where w_{α} denotes the mass fraction of species α within the associated total mass stream. The mass inflow of all non-source components from outside the system

boundaries is set to zero:

$$\dot{M}_{\alpha,(j,i)}^{\text{src}} = 0 \quad \forall (j,i) \in \mathcal{J}^I, \alpha \in \mathcal{C} \setminus \mathcal{C}^{\text{src}}, \quad (3)$$

where $\mathcal{C}^{\text{src}} \subseteq \mathcal{C}$ is the subset of components permitted to enter the system as external source streams. Furthermore, mass balance constraints are formulated to define the aggregate inlet stream characteristics for each process across all associated inlet ports. The total and partial mass flow rate entering process j is given by

$$\dot{M}_j^{\text{in,tot}} = \sum_{i:(j,i) \in \mathcal{J}^I} \dot{M}_{(j,i)}^{\text{in}} \quad \forall j \in \mathcal{J}, \quad (4)$$

$$w_{\alpha,j}^{\text{in,tot}} \dot{M}_j^{\text{in,tot}} = \sum_{i:(j,i) \in \mathcal{J}^I} w_{\alpha,(j,i)}^{\text{in}} \dot{M}_{(j,i)}^{\text{in}} \quad \forall j \in \mathcal{J}, \alpha \in \mathcal{C}, \quad (5)$$

where \mathcal{J} denotes the set of all processes in the superstructure. Eq. 2 and Eq. 5 can be regarded as mixing constraints.

An analogous formulation is employed for total and component-specific mass balances at each outlet port (j,o) in the process network. The total mass flow exiting an outlet port is expressed as

$$\dot{M}_{(j,o)}^{\text{out}} = \sum_{(\tilde{j},i):(j,o,\tilde{j},i) \in \mathcal{J}^{\text{OI}}} \dot{M}_{(j,o,\tilde{j},i)} + \dot{M}_{(j,o)}^{\text{sink}} \quad \forall (j,o) \in \mathcal{J}^O, \quad (6)$$

where $\dot{M}_{(j,o)}^{\text{sink}}$ represents the terminal outflow exiting the superstructure boundaries. The corresponding partial mass balances for each chemical species $\alpha \in \mathcal{C}$ are formulated as:

$$w_{\alpha,(j,o)}^{\text{out}} \dot{M}_{(j,o)}^{\text{out}} = \sum_{(\tilde{j},i):(j,o,\tilde{j},i) \in \mathcal{J}^{\text{OI}}} w_{\alpha,(j,o,\tilde{j},i)} \dot{M}_{(j,o,\tilde{j},i)} + w_{\alpha,(j,o)}^{\text{sink}} \dot{M}_{(j,o)}^{\text{sink}} \quad \forall (j,o) \in \mathcal{J}^O, \alpha \in \mathcal{C}, \quad (7)$$

for each possible outlet port (j,o) in the set \mathcal{J}^O . For consistency, the mass fraction of each component α within all connecting mass streams and external sink flows originating from outlet (j,o) is constrained to match the outlet composition:

$$w_{\alpha,(j,o,\tilde{j},i)} = w_{\alpha,(j,o)}^{\text{out}} \quad \forall (j,o,\tilde{j},i) \in \mathcal{J}^{\text{OI}}, \alpha \in \mathcal{C}, \quad (8)$$

$$w_{\alpha,(j,o)}^{\text{sink}} = w_{\alpha,(j,o)}^{\text{out}} \quad \forall (j,o) \in \mathcal{J}^O, \alpha \in \mathcal{C}. \quad (9)$$

This splitter formulation guarantees that mass fractions are consistently propagated across all material flow paths within and beyond system boundaries. The total mass flow exiting a process and distributed across all associated outlet ports is calculated via:

$$\dot{M}_j^{\text{out,tot}} = \sum_{o:(j,o) \in \mathcal{J}^O} \dot{M}_{(j,o)}^{\text{out}} \quad \forall j \in \mathcal{J}. \quad (10)$$

The component-wise distribution of the total outlet mass flow is described by:

$$w_{\alpha,j}^{\text{out,tot}} \dot{M}_j^{\text{out,tot}} = \sum_{o:(j,o) \in \mathcal{J}^O} w_{\alpha,(j,o)}^{\text{out}} \dot{M}_{(j,o)}^{\text{out}} \quad \forall j \in \mathcal{J}, \alpha \in \mathcal{C}. \quad (11)$$

To ensure conservation of mass, the total mass flow exiting each process must equal the total mass flow entering that process:

$$\dot{M}_j^{\text{out,tot}} = \dot{M}_j^{\text{in,tot}} \quad \forall j \in \mathcal{J}. \quad (12)$$

Due to the occurrence of chemical conversions within individual processes, the mass composition of process streams may be altered through the consumption or generation of chemical species. For those processes not represented via ANNs, a stoichiometry-based linear model is employed to approximate the relationship between reactants and products. Specifically, the component-wise total outlet mass flow is computed according to:

$$w_{\alpha,j}^{\text{out,tot}} \dot{M}_j^{\text{out,tot}} = w_{\alpha,j}^{\text{in,tot}} \dot{M}_j^{\text{in,tot}} + \nu_{\alpha,j} \Gamma_j \quad \forall j \in \mathcal{J} \setminus \mathcal{J}^{\text{ANN}}, \alpha \in \mathcal{C}, \quad (13)$$

where $\nu_{\alpha,j}$ is the stoichiometric coefficient representing the net production ($\nu_{\alpha,j} > 0$) or consumption ($\nu_{\alpha,j} < 0$) of component α in process j , and Γ_j denotes the scale of process j . The process scale Γ_j is calculated based on the production rate of a designated key component (α,j) associated with the process j , as follows:

$$\Gamma_j = w_{(\alpha,j)}^{\text{out,tot}} \dot{M}_j^{\text{out,tot}} \quad \forall (\alpha,j) \in \mathcal{C}^K, \quad (14)$$

where \mathcal{C}^K denotes the set of key components. For processes represented via ANNs (collected in the set \mathcal{J}^{ANN}), the outlet mass fractions are not computed from stoichiometric relations but are instead determined by the output of the corresponding trained machine learning models, which predict nonlinear mappings based on the given input variables. A detailed exposition of the ANN-based process modeling is provided in Section 4.

To ensure the physical consistency of mass composition across all process streams, equality constraints are imposed on the summation of component mass fractions in each relevant flow. These constraints are expressed as:

$$\sum_{\alpha \in \mathcal{C}} w_{\alpha,(j,i)}^{\text{in}} = y_j \quad \forall (j,i) \in \mathcal{J}^I, \quad (15)$$

$$\sum_{\alpha \in \mathcal{C}} w_{\alpha,(j,o)}^{\text{out}} = y_j \quad \forall (j,o) \in \mathcal{J}^O, \quad (16)$$

$$\sum_{\alpha \in \mathcal{C}} w_{\alpha,j}^{\text{in,tot}} = y_j \quad \forall j \in \mathcal{J}, \quad (17)$$

$$\sum_{\alpha \in \mathcal{C}} w_{\alpha,j}^{\text{out,tot}} = y_j \quad \forall j \in \mathcal{J}, \quad (18)$$

$$\sum_{\alpha \in \mathcal{C}} w_{\alpha,(j,o,\tilde{j},i)}^{\text{out,tot}} = y_j \quad \forall (j,o,\tilde{j},i) \in \mathcal{J}^{\text{OI}}. \quad (19)$$

The summation over all components $\alpha \in \mathcal{C}$ ensures that the total mass fractions in any given mass flow sum to unity whenever the associated process is operational. The binary decision variable $y_j \in \{0, 1\}$ encodes the status of process j , such that:

$$y_j = \begin{cases} 1, & \text{if process } j \text{ is installed,} \\ 0, & \text{otherwise,} \end{cases} \quad \forall j \in \mathcal{J}.$$

2.2 Energy balance

In addition to mass flows, processes within the superstructure are also characterized by the exchange of energy in the form of work (i.e., electricity) and heat, as illustrated in Figure 1. For all processes $j \in \mathcal{J} \setminus \mathcal{J}^{\text{ANN}}$, which are not modeled via ANNs, the work demand or generation rate \dot{W}_j is formulated as a linear function of the process scale Γ_j

$$\dot{W}_j = e_j \Gamma_j \quad \forall j \in \mathcal{J} \setminus \mathcal{J}^{\text{ANN}}, \quad (20)$$

where e_j denotes the specific work or electricity consumption/generation coefficient associated with process j . A negative value of e_j implies net electrical energy consumption, whereas a positive value indicates net generation. For processes represented by ANNs (i.e., $j \in \mathcal{J}^{\text{ANN}}$), the calculation of \dot{W}_j is addressed in detail in Section 4. Eq. 21 ensures that the sum of all generated and consumed work as well as the work that enters the system from outside (\dot{W}^{src}) or leaves the system (\dot{W}^{sink}) via the system boundaries is zero:

$$\sum_{j \in \mathcal{J}} \dot{W}_j + \dot{W}^{\text{src}} - \dot{W}^{\text{sink}} = 0. \quad (21)$$

2.3 Heat integration

Thermal integration constitutes a fundamental aspect of energy optimization in chemical process systems, as it enables the efficient redistribution of thermal energy between process streams. By facilitating internal system heat recovery, the dependence on external heating and cooling utilities is substantially reduced, thereby decreasing overall energy consumption, operating expenditures, and associated greenhouse gas emissions. This enhances both the thermodynamic efficiency and environmental sustainability of the network. The present heat integration framework builds upon the work by Ganzer and Mac Dowell,³³ and is extended herein to accommodate the simultaneous representation of multiple thermal sources and sinks within a single process. This generalization allows for a more accurate and flexible depiction of complex heat exchange scenarios.

All processes possessing the potential for thermal integration are aggregated into the set $\mathcal{J}^{\text{heat}}$. Furthermore, the set $\mathcal{J}^{\text{heat,s}}$ encompasses all distinct heat source and sink elements within these processes that are eligible for participation in inter-process heat exchange. For processes not represented by ANNs, the

thermal duty $\dot{Q}_{(j,h)}$ associated with each heat source or sink (j,h) is computed as a function of the process scale Γ_j according to the relation:

$$\dot{Q}_{(j,h)} = q_{(j,h)} \Gamma_j \quad \forall (j,h) \in \mathcal{J}^{\text{heat,s}} \setminus \mathcal{J}^{\text{ANN}}, \quad (22)$$

where $q_{(j,h)}$ denotes the specific heat load parameter for the respective heat source or sink. A positive value of $q_{(j,h)}$ indicates heat release (source), while a negative value corresponds to heat demand (sink). Thermal energy balances are established for all process-internal heat sources and sinks to ensure conservation of heat across inter-process exchanges. For each heat source (j,h) , the balance equation is expressed as:

$$\sum_{(\tilde{j},\tilde{h}) \in \mathcal{J}^{\text{heat,cold}}} \dot{Q}_{(j,h),(\tilde{j},\tilde{h})}^{\text{flow}} + \dot{Q}_{(j,h)}^{\text{sink}} = \dot{Q}_{(j,h)} \quad \forall (j,h) \in \mathcal{J}^{\text{heat,hot}} \setminus \{(\text{Gasification}, 2)\}, \quad (23)$$

where $\dot{Q}_{(j,h),(\tilde{j},\tilde{h})}^{\text{flow}}$ denotes the thermal energy transferred from heat source (j,h) to heat sink (\tilde{j},\tilde{h}) , and $\dot{Q}_{(j,h)}^{\text{sink}}$ represents the portion of thermal energy from source (j,h) that exits the system boundaries. Similarly, for each heat sink, the balance is given by:

$$\sum_{(\tilde{j},\tilde{h}) \in \mathcal{J}^{\text{heat,hot}}} \dot{Q}_{(\tilde{j},\tilde{h}),(j,h)}^{\text{flow}} + \dot{Q}_{(j,h)}^{\text{src}} = -\dot{Q}_{(j,h)} \quad \forall (j,h) \in \mathcal{J}^{\text{heat,cold}} \setminus \{(\text{Gasification}, 2)\}. \quad (24)$$

where $\dot{Q}_{(j,h)}^{\text{src}}$ accounts for the external thermal energy input required to satisfy the demand of sink (j,h) . The sets $\mathcal{J}^{\text{heat,hot}}$ and $\mathcal{J}^{\text{heat,cold}}$ contain all thermally active source and sink elements, respectively, within the superstructure network. A complete list of all processes participating in heat integration and all associated heat sources and sinks can be found in the Supplementary Information. Thermal energy exchanges between processes are constrained to be non-negative and are subject to upper bounds formulated using big- M constraints. Specifically, the inter-process heat transfer $\dot{Q}_{(j,h),(\tilde{j},\tilde{h})}^{\text{flow}}$ from a heat source (j,h) to a heat sink (\tilde{j},\tilde{h}) must satisfy:

$$\dot{Q}_{(j,h),(\tilde{j},\tilde{h})}^{\text{flow}} \leq z_{(j,h),(\tilde{j},\tilde{h})} M \quad \forall (j,h) \in \mathcal{J}^{\text{heat,hot}}, (\tilde{j},\tilde{h}) \in \mathcal{J}^{\text{heat,cold}}, \quad (25)$$

where M is a sufficiently large constant and $z_{(j,h),(\tilde{j},\tilde{h})} \in \{0,1\}$ is a binary decision variable that indicates whether a heat exchange link is active (i.e., equals 1 if heat is transferred, and 0 otherwise). Heat exchange is permitted only if both the supplying and receiving processes are operational. This is enforced by the following coupling constraints:

$$z_{(j,h),(\tilde{j},\tilde{h})} \leq y_j \quad \forall (j,h) \in \mathcal{J}^{\text{heat,hot}}, \quad (26)$$

$$z_{(j,h),(\tilde{j},\tilde{h})} \leq y_{\tilde{j}} \quad \forall (\tilde{j},\tilde{h}) \in \mathcal{J}^{\text{heat,cold}}. \quad (27)$$

Furthermore, to maintain the thermodynamic feasibility of heat exchange, a minimum temperature driving force is imposed. Specifically, heat can only be transferred from a source to a sink if the source temperature exceeds the sink temperature by at least a specified threshold ΔT^{\min} . This condition is represented as:

$$T_{(\tilde{j}, \tilde{h})} z_{(j,h),(\tilde{j},\tilde{h})} + \Delta T^{\min} z_{(j,h),(\tilde{j},\tilde{h})} \leq T_{(j,h)} z_{(j,h),(\tilde{j},\tilde{h})} \\ \forall (j,h) \in \mathcal{J}^{\text{heat,hot}}, (\tilde{j},\tilde{h}) \in \mathcal{J}^{\text{heat,cold}}. \quad (28)$$

Here, $T_{(j,h)}$ is the temperature level associated with the heat port (j,h) , which is either a constant parameter (see Supplementary Information) or is determined as a decision variable of the optimization problem (more details are given in Subsection 4.2).

The equality constraints specified in Eq. 23 and Eq. 24 are not applicable to the thermal interaction unit $(j,h) = \{\text{(Gasification, 2)}\}$, as this entity can function either as a heat source or a heat sink depending on the operating mode of the gasification step within the optimal system configuration. To accurately capture this dual-functionality within the superstructure optimization model, a dedicated set of constraints is introduced. Specifically, heat balance equations for the gasification process are reformulated as:

$$\sum_{(\tilde{j}, \tilde{h}) \in \mathcal{J}^{\text{heat,cold}}} \dot{Q}_{(\text{Gasification,2}),(\tilde{j},\tilde{h})}^{\text{flow}} + \dot{Q}_{(\text{Gasification,2})}^{\text{sink}} = \\ z_{(\text{Gasification,2})}^{\text{src,sink}} \dot{Q}_{(\text{Gasification,2})}, \quad (29)$$

$$\sum_{(\tilde{j}, \tilde{h}) \in \mathcal{J}^{\text{heat,hot}}} \dot{Q}_{(\tilde{j},\tilde{h}),(\text{Gasification,2})}^{\text{flow}} + \dot{Q}_{(\text{Gasification,2})}^{\text{src}} = \\ (1 - z_{(\text{Gasification,2})}^{\text{src,sink}}) (-\dot{Q}_{(\text{Gasification,2})}), \quad (30)$$

where the binary variable $z_{(\text{Gasification,2})}^{\text{src,sink}}$ is introduced to identify the operative mode of the gasification step: it assumes a value of 1 if $(j,h) = \{\text{(Gasification, 2)}\}$ functions as a heat source, and 0 if it acts as a heat sink. To ensure consistency in this binary characterization, the heat duty of the gasification step is further bounded as

$$\dot{Q}_{(\text{Gasification,2})} \leq z_{(\text{Gasification,2})}^{\text{src,sink}} M, \quad (31)$$

$$\dot{Q}_{(\text{Gasification,2})} \geq - (1 - z_{(\text{Gasification,2})}^{\text{src,sink}}) M. \quad (32)$$

Moreover, to avoid non-physical self-integration, the following constraint prohibits any thermal exchange from the gasification step to itself

$$z_{(\text{Gasification,2}),(\text{Gasification,2})} = 0. \quad (33)$$

A comprehensive explanation of this bidirectional thermal port within the gasification process is provided in Section 3.2.1.

2.4 Economic constraints

The overarching objective of the optimization framework is the minimization of the total annualized cost of the network, formally expressed as

$$K^{\text{tot}} = CR \sum_{j \in \mathcal{J}} K_j^{\text{cap}} + \sum_{\alpha \in \mathcal{C}} K_{\alpha}^{\text{op,comp}} + K^{\text{op,el}} + K^{\text{op,heat}}, \quad (34)$$

where K_j^{cap} denotes the CAPEX associated with the installation of process j , $K_{\alpha}^{\text{op,comp}}$ represents the operating cost linked to the procurement of compound α , and $K^{\text{op,el}}$ and $K^{\text{op,heat}}$ correspond to the annual electricity and heat-related operating costs, respectively. The term CR is the capital recovery factor, which annualizes the investment costs over the project lifetime:

$$CR = \frac{r(r+1)^{\theta}}{(r+1)^{\theta}-1}, \quad (35)$$

where a project lifetime of $\theta = 20$ years³ and an interest rate of $r = 7\%$ ³⁴ are assumed.

The CAPEX for processes that are not represented via ANNs, with the exception of the acid gas removal (AGR) process, is calculated based on the process scale Γ_j via:

$$K_j^{\text{cap}} = \beta_j \Gamma_j \quad \forall j \in \mathcal{J} \setminus \mathcal{J}^{\text{ANN}} \setminus \{\text{AGR}\}, \quad (36)$$

where β_j is the corresponding specific CAPEX of process j in \$/capacity. For ANN-represented processes, where the process scale Γ_j is undefined, and for processes where there is a lack of cost data based on the process scale, CAPEX is likewise estimated using the total inlet mass flow rate $\dot{M}^{\text{in,tot}}$. This total inlet mass flow rate is scaled by process-specific investment cost factors sourced from relevant literature.^{3,36,37} The specific constraints for the CAPEX calculation based on the total inlet mass flow rate can be found in the Supplementary Information.

OPEX associated with raw material procurement for each source component $\alpha \in \mathcal{C}^{\text{src}}$ are computed based on the total mass flow rates of these components entering the designated process inlet ports. The corresponding cost expression is formulated as

$$K_{\alpha}^{\text{op,comp}} = \tau \gamma_{\alpha}^{\text{src}} \sum_{(j,i) \in \mathcal{J}^{\text{I}}} \dot{M}_{\alpha,(j,i)}^{\text{src}} \quad \forall \alpha \in \mathcal{C}^{\text{src}}, \quad (37)$$

where $\tau = 8,760 \text{ h}$ denotes the annual plant operating time (assuming continuous year-round operation) and $\gamma_{\alpha}^{\text{src}}$ is the specific cost of raw material α in \$/kg. In a similar manner, the annual OPEX associated with external electricity and thermal energy supply are given by

$$K^{\text{op,el}} = \tau \gamma^{\text{el}} \dot{W}^{\text{src}}, \quad (38)$$

$$K^{\text{op,heat}} = \tau \gamma^{\text{heat}} \sum_{(j,h) \in \mathcal{J}^{\text{heat,cold}}} \dot{Q}_{\alpha,(j,h)}^{\text{src}}. \quad (39)$$

where γ^{el} and γ^{heat} denote the specific electricity and heat costs, respectively (in \$/kWh). A comprehensive summary of all economic parameters is provided in the Supplementary Information.

2.5 CO₂ balancing

In addition to the economic expenditures associated with the production of the kerosene fraction in the FT synthesis process, it is imperative to account for the total GHG emissions, quantified as CO₂ equivalents (CO₂-eq), arising from the entire production pathway. The minimization of these CO₂ emissions inherently conflicts with cost reduction, thereby introducing a multi-objective optimization problem involving a trade-off between economic and environmental performance metrics. The total CO₂ emissions, denoted as $\dot{M}^{\text{CO}_2,\text{tot}}$, are composed of several contributing factors

$$\begin{aligned}\dot{M}^{\text{CO}_2,\text{tot}} = & \sum_{\alpha \in \mathcal{C}^{\text{src}}} \dot{M}_{\alpha}^{\text{CO}_2,\text{src}} + \dot{M}^{\text{CO}_2,\text{sink}} + \tau \lambda^{\text{el}} \dot{W}^{\text{src}} \\ & + \tau \lambda^{\text{heat}} \sum_{(j,h) \in \mathcal{J}^{\text{heat,cold}}} \dot{Q}_{(j,h)}^{\text{src}}.\end{aligned}\quad (40)$$

The parameters λ^{el} and λ^{heat} represent the specific CO₂-eq emission intensities associated with electricity and heat provision, respectively, measured in kg_{CO₂-eq}/kWh. Detailed numerical values for these emission factors are provided in the Supplementary Information.

The emissions attributed to raw material inputs are determined by:

$$\dot{M}_{\alpha}^{\text{CO}_2,\text{src}} = \tau \lambda_{\alpha}^{\text{comp}} \sum_{(j,i) \in \mathcal{J}^{\text{I}}} \dot{M}_{\alpha,(j,i)}^{\text{src}} \quad \forall \alpha \in \mathcal{C}^{\text{src}}, \quad (41)$$

where $\lambda_{\alpha}^{\text{comp}}$ denotes the specific CO₂-eq emission factor associated with the supply chain and production of raw material α .

The term $\dot{M}^{\text{CO}_2,\text{sink}}$ captures the net mass flow rate of CO₂ that leaves the system boundary without being sequestered or utilized, and is computed as follows:

$$\begin{aligned}\dot{M}^{\text{CO}_2,\text{sink}} = & \tau \left(\sum_{(j,o) \in \mathcal{J}^{\text{O}} \setminus \{\text{CS},1\}} w_{\text{CO}_2,(j,o)}^{\text{sink}} \dot{M}_{(j,o)}^{\text{sink}} \right. \\ & + 1.571 \cdot \left(\sum_{(j,o) \in \mathcal{J}^{\text{O}} \setminus \{\text{FT},2\}} w_{\text{CO},(j,o)}^{\text{sink}} \dot{M}_{(j,o)}^{\text{sink}} \right) \\ & \left. + 2.743 \cdot \left(\sum_{(j,o) \in \mathcal{J}^{\text{O}} \setminus \{\text{FT},1\}} w_{\text{CH}_4,(j,o)}^{\text{sink}} \dot{M}_{(j,o)}^{\text{sink}} \right) \right).\end{aligned}\quad (42)$$

where the coefficients 1.571 and 2.743 represent the molecular weight ratios for the complete conversion of CO and CH₄, respectively, to CO₂, under the assumption that these species are fully oxidized upon release to the environment. The consideration of CO₂ emissions due to the C in the product streams is explained later in Subsection 2.7.

2.6 Process-specific constraints

Process-specific constraints are superimposed onto the general framework of the MIQCP formulation to enforce component-wise mass balances and ensure physicochemical feasibility of individual processes. These constraints restrict the admissible material flows such that only designated chemical species are permitted to enter or exit specific process streams in accordance with the underlying reaction stoichiometry and process function. For instance, within all electrolysis technologies, only H₂O is allowed as an input to the first inlet port, while the output streams are strictly limited to pure H₂ and pure O₂ at designated outlet ports. This behavior is mathematically enforced via the following constraints and binary variables:

$$w_{H_2O,(j,1)}^{\text{in}} = y_j, \quad \forall j = \{\text{AEC, PEMEC, SOEC}\}, \quad (43)$$

$$w_{H_2,(j,1)}^{\text{out}} = y_j, \quad \forall j = \{\text{AEC, PEMEC, SOEC}\}, \quad (44)$$

$$w_{O_2,(j,2)}^{\text{out}} = y_j, \quad \forall j = \{\text{AEC, PEMEC, SOEC}\}. \quad (45)$$

These equality constraints ensure that the component-specific flow indicators are activated exclusively when the associated electrolysis process is selected for installation. Similar constraints are used to model the remaining superstructure optimization processes, with a full list of equations provided in the Supplementary Information to this article.

To steer the optimization toward a desired production outcome, a fixed mass flow rate target is imposed on the primary outlet stream of the FT synthesis process. Specifically, the following constraint is introduced to enforce a fixed production rate:

$$\dot{M}_{(\text{FT},1)}^{\text{out}} = 3,000 \text{ kg/h.} \quad (46)$$

In addition to meeting this quantitative production benchmark, qualitative specifications pertaining to product composition are enforced to favor the generation of the C₈–C₁₆ kerosene hydrocarbon fraction. This compositional tuning is realized via inequality constraints that suppress the relative formation of undesired byproducts (namely, lighter gasoline-range hydrocarbons and heavier diesel-range compounds) by requiring their combined mass fractions (along with waste

water) not to exceed that of the kerosene fraction in the FT product stream

$$\sum_{\alpha \in \mathcal{C}^{\text{gasoline}}} w_{\alpha,(\text{FT},1)}^{\text{out}} + w_{\text{H}_2\text{O}_{\text{waste}},(\text{FT},1)}^{\text{out}} \leq \sum_{\alpha \in \mathcal{C}^{\text{kerosene}}} w_{\alpha,(\text{FT},1)}^{\text{out}}, \quad (47)$$

$$\sum_{\alpha \in \mathcal{C}^{\text{diesel}}} w_{\alpha,(\text{FT},1)}^{\text{out}} + w_{\text{H}_2\text{O}_{\text{waste}},(\text{FT},1)}^{\text{out}} \leq \sum_{\alpha \in \mathcal{C}^{\text{kerosene}}} w_{\alpha,(\text{FT},1)}^{\text{out}}. \quad (48)$$

These constraints collectively bias the optimization toward maximizing the yield of the kerosene-range hydrocarbons, thereby enhancing overall selectivity in favor of the target product fraction.

2.7 Post-optimization calculations

To rigorously attribute both cost and CO₂ emissions to the production of the C₈–C₁₆ kerosene fraction generated via the FT synthesis, a series of post-optimization calculations are employed. These computations utilize the optimal decision variables obtained from the solved MIQCP problem. The rationale for performing these evaluations *a posteriori* lies in the fact that integrating them directly into the optimization model would substantially increase the degree of nonlinearity, thereby exacerbating the computational complexity.

The total annual CO₂ emissions attributable to the production and combustion of the kerosene fraction are quantified via the following relationship:

$$\begin{aligned} \dot{M}^{\text{CO}_2, \text{tot, kerosene}} &= \frac{\delta^{\text{kerosene}}}{\delta^{\text{HC}}} \dot{M}^{\text{CO}_2, \text{tot}} + \tau \lambda^{\text{kerosene}} \dot{M}_{(\text{FT},1)}^{\text{out}} \\ &+ \tau \sum_{\alpha \in \mathcal{C}^{\text{kerosene}}} w_{\alpha,(\text{FT},1)}^{\text{sink}} \cdot \left(1.571 \cdot w_{\text{CO},(\text{FT},2)}^{\text{sink}} \dot{M}_{(\text{FT},2)}^{\text{sink}} \right) \end{aligned} \quad (49)$$

where emissions are allocated based on the energy-equivalent economic value of the kerosene fraction. This value is represented by the ratio of the specific energy content of the kerosene fraction, δ^{kerosene} , to the total specific energy content of all hydrocarbons produced by the FT process, δ^{HC} . These specific energy values are computed as weighted sums based on the mass fractions and specific lower heating values (δ_α) of the individual hydrocarbon components

$$\delta^{\text{kerosene}} = \sum_{\alpha \in \mathcal{C}^{\text{kerosene}}} w_{\alpha,(\text{FT},1)}^{\text{out}} \delta_\alpha, \quad (50)$$

$$\delta^{\text{HC}} = \sum_{\alpha \in \mathcal{C}^{\text{HC}}} w_{\alpha,(\text{FT},1)}^{\text{out}} \delta_\alpha. \quad (51)$$

Combustion-related CO₂ emissions are accounted for via the term $\lambda^{\text{kerosene}}$, which reflects the specific CO₂ emissions per kilogram of kerosene combusted and is defined as:

$$\lambda^{\text{kerosene}} = \sum_{\alpha \in \mathcal{C}^{\text{kerosene}}} w_{\alpha,(\text{FT},1)}^{\text{out}} \lambda_\alpha^{\text{comp}}, \quad (52)$$

assuming complete oxidation of the hydrocarbon constituents. Additionally, unconverted and purged CO from the second outlet port of the FT reactor is proportionally assigned to the kerosene product stream under the conservative assumption of complete atmospheric oxidation to CO₂.

In parallel with the emission allocation, total annualized production costs are similarly attributed to the kerosene fraction based on the same energy-weighted economic allocation principle

$$K^{\text{tot},\text{kerosene}} = \frac{\delta^{\text{kerosene}}}{\delta^{\text{HC}}} K^{\text{tot}}. \quad (53)$$

The total annual mass of kerosene-range hydrocarbons produced is computed as:

$$\dot{M}^{\text{sink},\text{kerosene}} = \tau \sum_{\alpha \in \mathcal{C}^{\text{kerosene}}} w_{\alpha,\text{(FT,1)}}^{\text{sink}} \dot{M}_{\text{(FT,1)}}^{\text{out}}. \quad (54)$$

From these values, the specific CO₂ emissions and specific production costs per unit mass of kerosene (in kg_{CO₂}/kg_{kerosene} and \$/kg_{kerosene}, respectively) are obtained through normalization by the annual kerosene output.

The economic viability and environmental effectiveness of alternative process configurations or technologies relative to a fossil-based benchmark can be quantitatively assessed through the metric of CO₂ abatement cost, denoted as $k_{\text{CO}_2}^{\text{ab}}$. This value is defined as the incremental cost per unit of CO₂ avoided and is computed according to the following relationship:⁸

$$k_{\text{CO}_2}^{\text{ab}} \left(\frac{\$}{\text{t}_{\text{CO}_2}} \right) = \frac{k_{\text{green kerosene}} - k_{\text{reference}} \left(\frac{\$}{\text{t}_{\text{kerosene}}} \right)}{\text{CO}_2 \text{ avoidance} \left(\frac{\text{t}_{\text{CO}_2}}{\text{t}_{\text{kerosene}}} \right)}, \quad (55)$$

where k represents the specific production cost (\$/kg_{kerosene}) and "abatement" is abbreviated as "ab". This metric enables a direct comparison across different pathways and technologies, facilitating the identification of the most cost-effective options.

A list of all parameters can be found in the Supplementary Information to this article.

3 Data set for Fischer-Tropsch sustainable aviation fuel

Conventional aviation fuels for commercial passenger aircraft, such as Jet A-1, are complex multicomponent mixtures comprising predominantly n-alkanes, iso-alkanes, cycloalkanes, and aromatic hydrocarbons.⁶ In contrast, SAFs derived from renewable feedstocks via FT synthesis exhibit a hydrocarbon distribution largely dominated by linear n-alkanes.² Owing to their limited compositional

diversity and associated physicochemical properties, these FT-derived SAFs typically require blending with conventional petroleum-based kerosene to meet the stringent performance and compatibility criteria for combustion in commercial aviation turbines. Given the methodological focus of the present study, the scope is restricted to the synthesis of n-alkanes in the carbon range C₁–C₃₀ as the representative FT product spectrum. Alternative production pathways and post-synthesis upgrading processes, such as hydrocracking and isomerization, are not considered within this work. The superstructure network for n-alkane synthesis via the FT route, encompassing raw material inputs, intermediate processing stages, and final product mixtures, is schematically illustrated in Figure 2. A brief overview of the components and subprocesses is provided in the following sections.

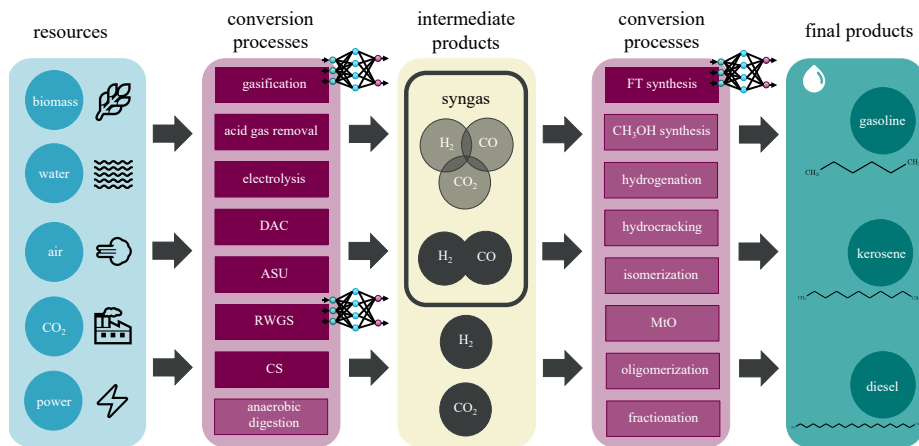


Figure 2 Superstructure network for the production of kerosene via Fischer-Tropsch (FT) synthesis. Processes that are represented by an artificial neural network (ANN) are indicated. Components and processes not considered in this study are greyed out. (DAC: direct air capture; ASU: air separation unit; RWGS: reverse water-gas shift; CS: carbon sequestration; FT: Fischer-Tropsch; MtO: Methanol-to-Olefins).

3.1 Components

In the context of the superstructure optimization, components are defined as all chemical species that may be consumed, produced, or transformed by the various processes within the system. These include species that either enter the system boundaries as external resources (designated as source components) or exit the network (referred to as sink components). Representative feedstocks considered in this work encompass three lignocellulosic biomass types (miscanthus, wheat straw, and pine chips), as well as inorganic inputs such as air and water. Syngas, comprising predominantly CO and H₂, is generated as an intermediate

mixture for subsequent synthesis. The product spectrum includes straight-chain alkanes (C_1 to C_{30}), which are modeled as final output components. To account for hydrocarbons beyond this range, a pseudo-component denoted as C_{30+} is introduced, aggregating all longer-chain n-alkanes. The system comprises a total of 47 distinct components; a comprehensive enumeration is provided in the Supplementary Information.

3.2 Processes

Processes convert one or more input components into a set of output components. Within the scope of this study, a total of eleven distinct processes are incorporated into the superstructure network. A key differentiation among these lies in the modeling approach: most processes are represented using simplified linearized formulations, commonly referred to as short-cut models, which approximate conversion mechanisms and have been the standard in nearly all previous work. In contrast, three processes whose behavior changes significantly for varying operating conditions and inlet compositions are described by ANNs, allowing a more detailed representation beyond the limits of linear approximations. A detailed description of these processes is provided in the following, the surrogate training and the integration of the ANNs are discussed later in Section 4. An overview and classification of all processes are presented in the Supplementary Information.

3.2.1 Processes represented by artificial neural networks

To achieve an optimal trade-off between the accurate representation of complex nonlinear process behavior through ANNs and the computational tractability of the overall superstructure optimization, only those processes which exhibit strong nonlinearities and where changes in operating conditions change the material flows in the superstructure are represented as ANNs. Aspen Plus[®]¹⁵ simulations serve as the basis for generating the datasets used to train the surrogate models. Specifically, the biomass gasification, reverse water-gas shift (RWGS), and FT synthesis processes are represented via rigorous flowsheet simulations to capture the dependence of their output compositions on varying operating conditions, such as temperature, pressure, and inlet compositions.

Biomass gasification. Gasification constitutes a complex, multi-step thermochemical conversion pathway wherein lignocellulosic biomass is transformed into a gaseous product mixture predominantly composed of H_2 , CO , CO_2 , and water vapor (H_2O). Minor constituents, including nitrogen (N_2), ammonia (NH_3), hydrogen chloride (HCl), hydrogen sulfide (H_2S), and condensable hydrocarbons such as tars, are also typically present as process-derived impurities.^{38,39} The overall gasification mechanism encompasses several sequential and overlapping reactions, notably pyrolysis, partial oxidation, and hydrogenation. Pyrolytic

decomposition generally occurs at temperatures below 600 °C, while partial oxidation and associated hydrogenation reactions proceed at significantly elevated temperatures, ranging from 700 to 1,600 °C. To avoid complete combustion of carbonaceous species to CO₂, the process operates under sub-stoichiometric oxygen conditions. The selection of the oxidizing medium – steam, air, pure O₂, or CO₂ – significantly alters the thermodynamic driving forces and dominant reaction pathways. For instance, steam-enhanced gasification promotes hydrogen formation via the water-gas shift equilibrium, whereas oxygen-enriched environments favor syngas generation with higher lower heating values. Additionally, CO₂-assisted gasification can enhance CO production through the Boudouard reaction. The physicochemical characteristics of the biomass feedstock (e.g., miscanthus, wheat straw, or pine chips) directly affect the yield and speciation of by-products, particularly nitrogen- and sulfur-containing compounds, which necessitate downstream gas-cleaning measures prior to FT synthesis.⁴⁰

Figure 3 shows the Aspen Plus®¹⁵ flowsheet of the biomass gasification process. Peng-Robinson-Boston-Mathias (PR-BM) is chosen as the global property

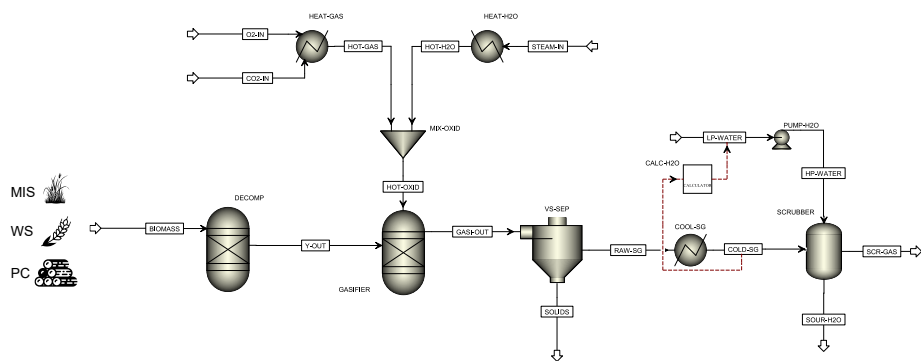


Figure 3 Aspen Plus®¹⁵ flowsheet simulation of the gasification process, taking into account three types of biomass. The gasification process is divided into three principal stages: thermal decomposition and gasification of the biomass feedstock, pretreatment of the gasifying agents, and subsequent gas purification (removal of solid components and other impurities). (MIS: miscanthus; WS: wheat straw; PC: pine chips).

method for this model.^{41,42} Biomass and ash are treated as non-conventional solids based on the proximate, ultimate and sulphur analyses, while Aspen Plus®¹⁵ proprietary methods DCOALIGT and HCOALGEN are used for density and enthalpy calculations.⁴³

The gasification process is conceptually divided into three principal stages: (i) thermal decomposition and gasification of the biomass feedstock, (ii) pretreatment of the gasifying agents, and (iii) subsequent gas purification. In this study, three distinct lignocellulosic biomass types (miscanthus, wheat straw, and pine chips), characterized by varying proximate and ultimate compositions (detailed in Table C.1. in the Supplementary Information), are considered to capture

feedstock heterogeneity. The initial decomposition phase involves pyrolyzing the biomass in an inert environment at 450 °C, in the absence of gasification agents. This devolatilization step is modeled using the RYield reactor module in Aspen Plus®,¹⁵ which disaggregates the biomass into volatile gaseous species and residual solid char as a function of its composition.^{40,43} Following the initial decomposition, the resultant biomass fragments are introduced into the gasification reactor alongside preheated oxidizing agents (namely steam, O₂, and/or CO₂) at an inlet temperature of 450 °C. Gasification is modeled using a thermodynamic equilibrium-based approach via an RGibbs reactor in Aspen Plus®,¹⁵ operating within a temperature range of 800 to 1,300 °C. The overall thermal nature of this stage, either exothermic or endothermic, is dependant upon both the reactor temperature and the molar quantities of oxidizing agents, thereby dictating whether auxiliary heat input is required. Post-gasification, residual solids are removed via a SSplit module, configured with a split fraction of one for solid species to ensure complete separation. The remaining gaseous stream is then cooled to 300 °C prior to undergoing a gas purification step, where a water scrubbing unit eliminates soluble contaminants, particularly ammonia (NH₃).⁴⁰ Inputs for the flowsheet simulation and subsequent training of the gasification ANN with the associated bounds can be found in Table 1.

Table 1 Inputs of the biomass gasification artificial neural network (ANN) with the corresponding upper and lower bounds. (MIS: miscanthus; WS: wheat straw; PC: pine chips).

ANN input	lower bound	upper bound
biomass type	{MIS, WS, PC}	{MIS, WS, PC}
steam-to-biomass ratio (mass-based)	0.01	1
CO ₂ -to-biomass ratio (mass-based)	0	1
O ₂ -to-biomass ratio (mass-based)	0.05	0.3
gasifier temperature	800 °C	1,300 °C

To incorporate the distinct biomass feedstocks within the gasification ANN via one-hot encoding, an auxiliary set of binary decision variables is introduced into the MIQCP formulation. These variables are defined as follows:

$$x_\alpha = \begin{cases} 1, & \text{if biomass type } \alpha \text{ is selected,} \\ 0, & \text{otherwise,} \end{cases} \quad \forall \alpha \in \mathcal{C}^{\text{biomass}},$$

where $\mathcal{C}^{\text{biomass}}$ denotes the set of biomass types (e.g., miscanthus, wheat straw, and pine chips).

To align with the generalized process configuration depicted in Figure 1, the gasification process flowsheet is designed with five distinct inlet ports: one for the biomass feedstock, three for the oxidizing agents (steam, O₂, and CO₂), and one for the water supply to the downstream scrubbing unit. The system also incorporates three outlet ports: a solid-phase discharge stream, a waste water stream from the scrubbing unit (containing dissolved contaminants), and a gas-phase product stream representing the cleaned synthesis gas exiting the process.

Thermal integration within the gasification subsystem is modeled through three heat exchange interfaces. The decomposition stage necessitates a thermal input at approximately 450 °C, while thermal energy is recuperated during the post-gasification cooling phase at 300 °C. Additionally, the gasification reactor itself may operate as either an exothermic or endothermic unit, functioning as a heat source or sink depending on the specific operating conditions and oxidant loading, as elaborated in Subsection 2.3.

Overall, the ability of the gasification process to operate under various conditions enables it to adapt to changing circumstances in the superstructure.

Reverse water-gas shift. CO₂ captured from air must undergo chemical activation prior to its utilization in the synthesis of long-chain hydrocarbons via FT synthesis. This activation is achieved through the RWGS process, wherein CO₂ is reacted with H₂ to form CO and H₂O. The RWGS reaction is endothermic, as described by the following stoichiometry:



and is typically favored at elevated temperatures in the range of 800 to 900 °C, where equilibrium conversion is thermodynamically enhanced.^{3,44} The resulting syngas can then be supplied to the FT synthesis.

The RWGS process flow diagram is presented in Figure 4. Following Bube et

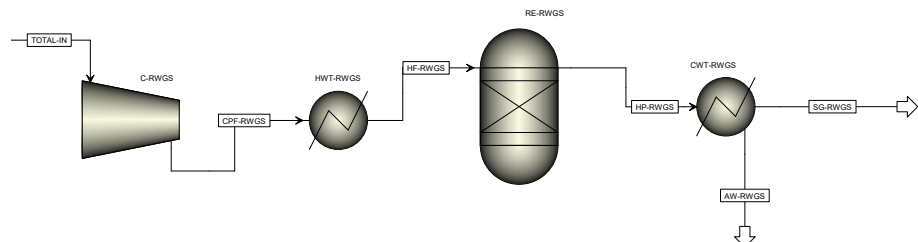


Figure 4 Aspen Plus®¹⁵ flowsheet simulation of the reverse water-gas shift (RWGS) process. The RWGS process consists of three parts: pretreatment of the feed mixture, the RWGS equilibrium reaction, and cooling of the reaction mixture and associated water separation.

al.,¹² the PR-BM equation of state is employed as the global property method to ensure accurate thermophysical property estimation across the relevant pressure and temperature regimes. A mixture of CO₂ and H₂ is first subjected to polytropic compression to attain the designated operating pressure of 20 bar. The compressed gas mixture is subsequently heated to the target reaction temperature. The endothermic RWGS reaction is simulated within an RGibbs reactor unit under thermodynamically ideal conditions, with reaction temperatures ranging from 850 to 1,000 °C. Continuous external heat input is required to sustain isothermal reactor operation. Nickel-based catalysts are typically employed in practical applications to enhance the reaction kinetics and facilitate favorable

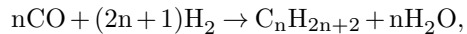
equilibrium conversion.^{12,44} Following the reaction, the effluent gas stream, comprising CO₂, H₂, CO, and H₂O, is cooled to near-ambient conditions, allowing for the removal of condensed water via phase separation. The inputs and the corresponding lower and upper bounds for the RWGS ANN are listed in Table 2.

Table 2 Inputs of the Reverse water-gas shift (RWGS) artificial neural network (ANN) with the corresponding upper and lower bounds.

ANN input	lower bound	upper bound
reactor temperature	850 °C	1,000 °C
H ₂ mass fraction in	0.02	0.25

From a process integration standpoint, the RWGS process comprises a single inlet (reactant mixture), two outlet ports (synthesis gas and liquid water), one heat sink (representing the aggregate thermal demand for both preheating and isothermal reactor operation), and one heat source (associated with post-reaction cooling and water condensation).

Fischer-Tropsch synthesis. FT synthesis encompasses a series of polymerization reactions whereby synthesis gas is catalytically converted predominantly into linear alkanes spanning a broad carbon number distribution, from light gaseous species such as methane (C₁) to high molecular weight waxes. This transformation can be represented by this generalized stoichiometric reaction:



where n denotes the carbon chain length.^{10,12} In industrial settings, minor fractions of alkenes and oxygenated hydrocarbons are concurrently produced due to reaction pathways and catalyst selectivity. The product distribution is modulated by catalyst composition, primarily cobalt- or iron-based catalysts, and reaction conditions, including temperature, pressure, and synthesis gas composition.⁴⁵ Within the present investigation, the FT synthesis output constitutes the principal target product stream, with a design objective to maximize yield within the C₈ to C₁₆ carbon range, corresponding to optimal hydrocarbon chain lengths for SAF applications.⁶

The chain length distribution of the FT synthesis exhibits significant variability as a function of pressure, temperature, and the H₂/CO feed ratio.^{46,47} To capture this complex, nonlinear behavior within the context of our optimization framework, an ANN is developed and trained utilizing simulation data generated from an Aspen Plus®¹⁵ model, as illustrated in Figure 5. Following the other two steady-state flowsheet simulations (gasification and RWGS), PR-BM is chosen as the global property method.¹²

Initially, high-purity synthesis gas is blended with recycled, unconverted CO and H₂ prior to undergoing compression. The compression stage is modeled as a multi-stage compression system incorporating interstage cooling, wherein the gas mixture is elevated to an operational pressure in the range of 30 to 55 bar, with

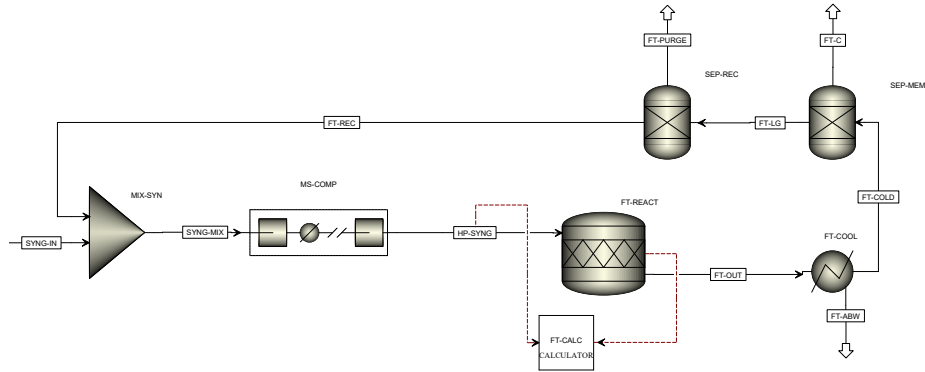


Figure 5 Aspen Plus[®]¹⁵ flowsheet simulation of the Fischer-Tropsch (FT) process. The FT process consists of the following steps: pretreatment of the synthesis gas mixture, the exothermic FT reaction, product separation (water removal, separation of light gas components from long-chain hydrocarbons), and recycling of the reactant components CO and H₂.

the discharge temperature regulated to align with the desired reaction temperature, set between 200 and 300 °C.⁴⁵ Subsequently, the gas stream enters the FT synthesis stage, where we assume cobalt-catalyzed, low-temperature FT synthesis due to its favorable kinetics and selectivity for long-chain paraffinic hydrocarbons. The FT reactor is modeled as a stoichiometric reactor (RStoic) within Aspen Plus[®],¹⁵ encompassing a detailed reaction scheme that accounts for the formation of linear n-alkanes ranging from C₁ to C₃₀. To approximate the contribution of higher molecular weight fractions, a lumped pseudo-component, denoted as C₃₀₊, is introduced. Minor by-products such as olefins and oxygenates are excluded from the model owing to their low yield under cobalt catalysis and limited relevance to SAF production.^{48,49} The hydrocarbon product distribution is computed based on an empirically derived chain growth probability parameter, utilizing the Anderson–Schulz–Flory (ASF) distribution model. This distribution is dependent on key operating variables, including reaction pressure, temperature, and syngas composition.^{48,49} Details of the custom Excel-calculator block routine integrated within our Aspen Plus[®]¹⁵ simulation are provided in the Supplementary Information. Post-reaction, the effluent is subjected to cooling to facilitate condensation and removal of the majority of water generated during synthesis. The product stream is subsequently separated from unreacted syngas using simplified split fraction models. A portion of the unconverted CO/H₂ stream is purged to prevent buildup within the system, while the remainder is recycled and remixed with fresh feed. Approximately 98 % of unreacted H₂ is recovered via recycling. The CO recycle rate is adjusted via a design specification by adapting the purge ratio to maintain the H₂/CO molar ratio at the FT reactor inlet within the valid range of the empirical FT reactor model. Table 3 shows the inputs considered for the FT ANN with the corresponding upper and lower

Table 3 Inputs of the Fischer-Tropsch (FT) artificial neural network (ANN) with the corresponding upper and lower bounds.

ANN input	lower bound	upper bound
reactor temperature	200 °C	300 °C
reactor pressure	30 bar	55 bar
H ₂ mass fraction in	0.115	0.15

bounds.

The overall FT process is characterized by one feed inlet, three distinct product outlet ports (product, water, purge), and two thermal interactions (the exothermic heat release associated with FT synthesis and the heat removal required for post-reaction cooling).

3.2.2 Linear processes

For the remaining processes, chemical conversions are modeled based on a linear shor-cut model according to Eq. 13. In the following, these processes are described in more detail.

Air separation unit. A cryogenic distillation (CRD)-based air separation unit (ASU) is incorporated into the network configuration to provide high-purity O₂ for integration into the gasification stage, thereby improving the quality of the resulting synthesis gas and enhancing overall thermodynamic and process efficiencies. The ASU operates at cryogenic temperatures, typically ranging from approximately –180 to –196 °C, to achieve phase separation of atmospheric air into its principal constituents.^{50,51} O₂ is recovered as the primary product, while N₂, which is not utilized within the system boundaries, is treated as a non-value-adding byproduct and subsequently discharged as waste. Key technical and economic parameters associated with the CRD, including its specific energy consumption, operational efficiency, and cost metrics, are provided in the Supplementary Information.

Direct air capture. Based on Svitnič and Sundmacher,³⁴ we consider the Climeworks low temperature DAC process to separate CO₂ from ambient air using electricity for fans and heat for desorption.^{52,53} Parameters for DAC, such as energy efficiency and costs, are listed in the Supplementary Information.

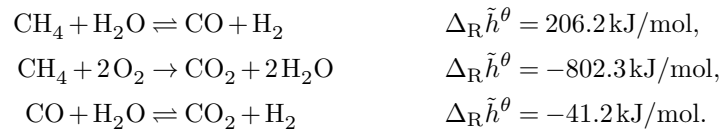
Water electrolysis. The production of high-purity H₂ via electrochemical water splitting follows this overall reaction:



Not only the H₂ can be used for fuel synthesis, but the produced O₂ can also be utilized as an oxidizing agent in the biomass gasification process. Three distinct

electrolysis technologies are included: alkaline electrolysis cells (AEC), proton exchange membrane electrolysis cells (PEMEC), and solid oxide electrolysis cells (SOEC). AEC systems utilize a concentrated aqueous solution of potassium hydroxide (KOH) as the electrolyte and incorporate porous diaphragms to separate the anode and cathode compartments. This configuration enables durable and economically favorable operation but is limited by lower achievable current densities and slower dynamic response characteristics. PEMEC systems employ a solid polymer electrolyte, which allows for elevated current densities, rapid transient behavior, and compact system architecture. However, these advantages come at the cost of increased capital expenditure due to the requirement for noble metal catalysts (e.g., platinum or iridium). SOEC technology operates under high-temperature conditions (700–900 °C) and utilizes dense ceramic electrolytes, commonly stabilized zirconia. This thermally assisted operation reduces the electrical energy demand by leveraging external heat sources, thereby enhancing overall efficiency. Nonetheless, the elevated temperatures impose significant material durability and system longevity constraints. Each electrolyzer variant presents specific trade-offs in terms of efficiency, capital intensity, and integration potential, which must be evaluated relative to system objectives and available energy resources.^{51,54,55} A comprehensive overview of their energy consumption metrics, economic parameters, and techno-economic assumptions is provided in the Supplementary Information.

Autothermal reforming. To facilitate a techno-economic and environmental comparison between sustainable liquid fuel production pathways and conventional fossil-based routes, this study incorporates an autothermal reforming (ATR) process for the generation of synthesis gas from methane (CH₄). The ATR process is selected based on its superior thermal efficiency relative to conventional steam methane reforming (SMR), as substantiated by Kim et al.⁵⁶ and Svitnic et al.⁵⁷ Operating under elevated temperatures (approximately 900 °C) and moderate to high pressures (10 bar⁵⁶ to 35 bar⁵⁸), the ATR process combines partial oxidation and steam reforming within a single reactor, enabling a thermally balanced system. The chemical reactions include:



The exothermic partial oxidation of methane provides the thermal energy necessary to drive the endothermic steam reforming reaction, thus enabling autothermal operation. The resultant syngas mixture is characterized by a H₂-enriched composition relative to CO, making it suitable for downstream synthesis processes.⁵⁶ The O₂ required for oxidation can be supplied via CRD or electrolysis, depending on process integration preferences. Detailed process parameters, assumptions, and performance indicators for the ATR configuration are documented in the Supplementary Information.

Acid gas removal. Due to the presence of undesirable constituents such as CO₂, H₂O, and trace contaminants including H₂S and NH₃ in the product gas streams generated by biomass gasification and RWGS, a gas purification step is required prior to utilization of these streams as synthesis gas in FT synthesis. To this end, an AGR process based on the Rectisol® approach is employed, following the design principles outlined by Liu et al.⁵⁹ In this process, chilled methanol is used as a physical solvent capable of selectively absorbing acid gases and polar impurities due to its high solubility characteristics at low temperatures. The Rectisol® technology enables near-complete removal of contaminants such as H₂S, NH₃, and CO₂, thereby producing a high-purity synthesis gas stream suitable for catalytic conversion in FT reactors.^{59–61} The extent of CO₂ removal can be tailored to meet downstream processing requirements.

Carbon sequestration. To incorporate the option of permanent carbon removal within the overall framework, a dedicated carbon sequestration (CS) process is integrated into the superstructure. This process facilitates the transport and subsequent sequestration of high-purity CO₂ streams originating from various upstream processes.¹⁶ The CS process is modeled to accommodate pure CO₂ as an input and is assumed to achieve complete containment of the captured carbon, thereby contributing to net emissions mitigation within the system boundaries. All assumptions related to the operational and economic parameters of the CS unit are detailed in the Supplementary Information.

4 Process representation via neural networks

To address the limitations inherent in conventional superstructure optimization, namely, the reliance on linear input–output representations and the a priori fixation of process operating conditions such as temperature and pressure, selected subprocesses within the network are embedded as ANNs via Aspen Plus®¹⁵ flowsheet simulations. While the incorporation of detailed mechanistic models that account for thermodynamic equilibria, reaction kinetics, and process efficiencies would enhance model fidelity, their direct integration into a MIQCP framework would introduce substantial nonlinearities, thereby impeding the tractability and solvability of the global optimization problem. To circumvent this challenge, ANNs are trained on data generated from Aspen Plus®¹⁵ simulations. These surrogate models are subsequently embedded within the optimization framework, enabling the representation of complex nonlinear process behavior while preserving the quadratically constrained nature and associated computational efficiency.

ANNs are extensively employed for data-driven function approximation and have been successfully applied across a broad range of scientific and engineering disciplines.^{62,63} Mathematically, a feed-forward ANN is structured as a sequence of $L \in \mathbb{N}$ layers, each performing an affine linear transformation of its input followed by the application of a nonlinear activation function $\sigma : \mathbb{R} \rightarrow \mathbb{R}$, which

is typically applied element-wise. The computational operation of each layer $l \in [L]$ is expressed as:

$$x^{(l)} = \sigma^{(l)} \left(W^{(l)} x^{(l-1)} + b^{(l)} \right) \quad \forall l \in [L], \quad (56)$$

where $x^{(0)} = x \in \mathbb{R}^{n_x}$ denotes the input vector to the network, and $W^{(l)} \in \mathbb{R}^{n_l \times n_{l-1}}$, $b^{(l)} \in \mathbb{R}^{n_l}$ represent the trainable weight matrix and bias vector associated with layer l .⁶⁴ In this study, the rectified linear unit (ReLU) function is employed as the activation function:

$$\text{ReLU}(x) = \max\{0, x\}, \quad (57)$$

which induces a piecewise affine linear mapping within the ANN. This structure renders ReLU-activated networks particularly suitable for integration into MILP formulations. The key principle is that each ReLU neuron can be expressed using linear constraints coupled with a binary decision variable, which encodes the activation status of the neuron – i.e., whether the input is positive (active segment) or non-positive (inactive segment). By explicitly modeling the selection of the active linear segment, the MILP formulation can exactly represent the ANN's nonlinear mapping.

The integration of ANNs into mathematical optimization frameworks necessitates the introduction of auxiliary decision variables and constraints to replicate the input–output mappings learned by the data-driven surrogate models. A principal advantage of ReLU-activated ANNs lies in their capacity to approximate complex nonlinear relationships while retaining compatibility with MILP formulations through so-called big- M reformulations. These reformulations are widely adopted in MILP to model binary decisions corresponding to activated and non-activated states in piecewise linear functions and can thus be applied to the ReLU activation. Assuming bounded pre-activation inputs for each neuron, i.e., $LB_i^{(l)} \leq W_i^{(j)} x^{(l-1)} + b_i \leq UB_i^{(l)}$, the ReLU activation for a single neuron i in layer l , given by $x_i^{(l)} = \text{ReLU}(W_i^{(l)} x^{(l-1)} + b_i)$, can be equivalently represented via the following set of MILP constraints:

$$\begin{aligned} x_i^{(l)} &\geq 0, \\ x_i^{(l)} &\geq W_i^{(l)} x^{(l-1)} + b_i, \\ x_i^{(l)} &\leq W_i^{(l)} x^{(l-1)} + b_i - LB_i^{(l)} \left(1 - \epsilon_i^{(l)} \right), \\ x_i^{(l)} &\leq UB_i^{(l)} \epsilon_i^{(l)}, \\ \epsilon_i^{(l)} &\in \{0, 1\}, \end{aligned} \quad (58)$$

where $W_i^{(l)}$ denotes the i -th row of the weight matrix in layer l , and $\epsilon_i^{(l)}$ is a binary variable that activates the appropriate affine segment of the piecewise function.^{32,65,66} This formulation enables the exact representation of the ReLU-based ANNs. Consequently, the surrogate models serve as an efficient mechanism

for embedding the nonlinear thermodynamic and kinetic behavior derived from Aspen Plus®¹⁵ simulations, without exacerbating the overall nonlinearity of the MIQCP formulation described in Section 2.

To facilitate the systematic incorporation of trained ANNs into our MIQCP framework, the Optimization & Machine Learning Toolkit (**OMLT**), as developed by Ceccon et al.,⁶⁷ is employed. **OMLT** is a Python-based computational toolkit designed for the representation of machine learning models, including neural networks and gradient-boosted decision trees, within deterministic optimization formulations. The package enables the automatic generation of the requisite decision variables and algebraic constraints for embedding trained ANNs within the **Pyomo**^{68,69} algebraic modeling environment.

4.1 Artificial neural network training

The process flowsheets delineated in Subsubsection 3.2.1 are used to generate the training data sets for the ANNs. To facilitate this, the integrated Aspen Plus®¹⁵–Python interface is employed to execute a fully automated simulation workflow. Following the specification of relevant input parameters and their respective bounds, a Latin Hypercube Sampling (LHS) methodology is implemented to ensure a statistically robust and space-filling sampling of the input domain. We explicitly include boundary (extreme) values to enhance model generalizability.^{24,70} A comprehensive enumeration of all input and output variables associated with the three ANN architectures is provided in the Supplementary Information accompanying this article.

A distinctive feature of the gasification ANN lies in its capacity to predict the syngas composition, specifically, the molar fractions of key constituents such as H₂ and CO, as a function of the chosen biomass feedstock (see Figure 3 and Table C.1. in the Supplementary Information). To incorporate categorical input data pertaining to biomass type, a one-hot encoding scheme is implemented.^{71,72} This encoding methodology transforms discrete categorical variables into binary vectors, wherein each biomass class is uniquely represented by a vector containing a single activated element (value of 1) corresponding to the class identity, with all remaining elements deactivated (value of 0). Such a representation avoids the imposition of artificial ordinal relationships among categories, thereby preserving the nominal nature of the data. Within the gasification ANN framework, this encoding enables the network to differentiate between biomass types and to learn underlying relationships between feedstock characteristics and resultant gas-phase composition.

The data sets comprise 75,000 simulation data points per biomass type for the gasification flowsheet, 50,000 data points for the RWGS process, and 10,000 data points for the FT synthesis flowsheet. As the primary objective of this study is not to determine the minimal data requirements for accurate ANN training, the data set sizes are selected to be sufficiently large to enable accurate approximation of the underlying process models. All ANNs are implemented and trained using the Keras Application Programming Interface (API) within the TensorFlow framework.⁷³ Prior to training, input and output variables are standardized, and

the data is partitioned into training and test subsets following an 80/20 split. Additionally, 20 % of the training subset is reserved for validation during training to monitor generalization and prevent overfitting. Hyperparameter optimization is conducted through systematic tuning procedures, with a full listing of selected hyperparameters provided in the Supplementary Information. It is established in the literature that optimization over embedded ANNs becomes significantly more challenging as the number of hidden layers in the ANNs increases.^{27,32,66,74} To achieve an optimal compromise between computational efficiency during integration into the overarching superstructure optimization framework and predictive accuracy, all ANN architectures employ a single hidden layer with varying numbers of ReLU activation neurons. Model training is performed using the Adam optimization algorithm,⁷⁵ with mean squared error (MSE) employed as the loss function. A summary of key performance indicators for the trained ANNs is presented in Table 4, while representative parity plots illustrating prediction

Table 4 Performance metrics of artificial neural networks. MSE_{train}: mean squared error for training data; MAE: mean absolute error; MAPE: mean absolute percentage error.

performance metric	gasification	RWGS	FT
MSE _{train}	1.0760×10^{-4}	2.8544×10^{-4}	1.6×10^{-3}
R^2	0.99994	0.99992	0.99955
MAE	0.000453	0.000497	0.000315
MAPE	0.004120	0.001713	0.064073

accuracy for each ANN are shown in Figure 6.

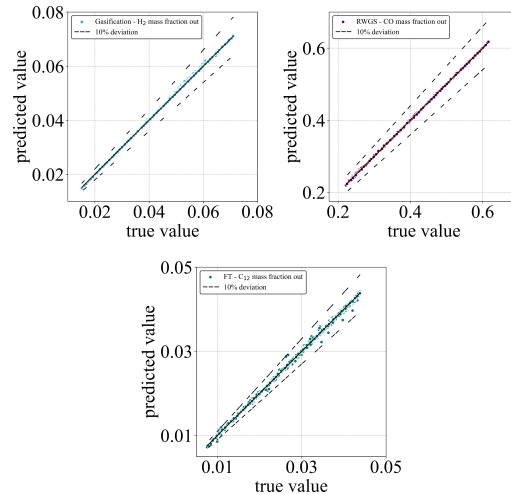


Figure 6 Selected parity plots for the artificial neural networks. Test data points are shown for three selected neural network outputs. (H₂ mass fraction exiting the gasification process after the water scrubbing unit; CO mass fraction in the output of the reverse water-gas shift process via the first outlet port; C₁₂H₂₆ mass fraction of the Fischer-Tropsch output).

It is evident that the ANN architectures with only one hidden layer per network are sufficient to predict the relationships between the inputs and outputs with satisfactory accuracy. Further details regarding network training and performance evaluation are provided in the Supplementary Information.

4.2 Embedding

Following the training of the ANNs, the corresponding decision variables and algebraic constraints necessary for representing the network architecture and input–output behavior are integrated into the overall MIQCP formulation via the OMLT framework,⁶⁷ as detailed in Section 2. This integration involves establishing equality constraints that directly couple the ANN input and output variables (denoted as $f_{j,(input,i)}^{\text{ANN}}$ and $f_{j,(output,o)}^{\text{ANN}}$ for process j and input/output i/o) to the decision variables defined within the superstructure (see Figure 1). For instance, the decision variable representing the reaction temperature in the biomass gasification step is mapped to the seventh input node of the corresponding gasification ANN ($T_{(\text{Gasification},2)} = f_{\text{Gasification},(\text{input},7)}^{\text{ANN}}$). Output variables of the ANNs are then expressed as functions of these linked inputs. As an illustrative example, the mass fractions of hydrocarbon species at the first outlet port of the FT synthesis process are computed via the trained FT ANN model according to the following relation:

$$w_{\text{C}_n\text{H}_{2n+2},(\text{FT},1)}^{\text{out}} = y_{\text{FT}} f_{\text{FT},(\text{output},n+2)}^{\text{ANN}} \quad \forall n = 1, \dots, 30. \quad (59)$$

Important operating parameters such as the reaction temperature, the pressure and the mass fraction of H₂ at the inlet ($T_{(\text{FT},1)}, p_{\text{FT}}, w_{\text{H}_2,(\text{FT},1)}^{\text{in}}$) are taken into account as ANN inputs and thus influence the outputs. Through this formulation, all input and output variables of the embedded ANNs are hard-linked to the superstructure's decision variables, ensuring full integration of data-driven surrogate models within the global optimization framework. A complete enumeration of the associated equality and inequality constraints is provided in the Supplementary Information.

In order to represent the categorical inputs of the gasification ANN, the binary variables used to describe the biomass types (introduced in Section 3.2.1) are mapped to the first three input nodes of the ANN, such that each input node is constrained to assume binary values (0 or 1). In this way, the one-hot encoding paradigm is adhered to and it is ensured that at most one biomass type is active.

The integration of ANNs within the optimization framework facilitates the direct inclusion of both ANN inputs and outputs as decision variables in the higher-level MIQCP formulation. This bidirectional embedding allows for the imposition of explicit constraints on both the input and output domains of the ANNs, thereby enabling optimization not only in the forward predictive direction but also in reverse. Consequently, the introduction of supplementary decision variables at the plant- and unit-operation level substantially broadens the design space and increases the degrees of freedom (e.g., reaction temperature, inlet composition).

All instances of the MIQCP problem incorporating embedded ANNs are solved on an Apple MacBook Pro equipped with an M4 Max system-on-chip, comprising a 16-core CPU, a 40-core GPU, and a unified memory architecture with a total of 48 GB of RAM. The optimization tasks are executed via the **Gurobi Optimizer**,³⁵ version 12.0.1, interfaced through the **Pyomo**^{68,69} modeling framework. The full optimization formulation encompasses approximately 6,000 continuous and 250 binary decision variables, of which 200 binary variables specifically encode the activation patterns of ReLU-based hidden neurons within the embedded ANNs. By leveraging warm-start initialization techniques, utilizing solutions obtained from prior optimization runs, and methodological enhancements outlined in Plate et al.,³² computational solution times are consistently maintained below 500 s.

5 Results

5.1 Cost vs. CO₂ emissions

As detailed in Subsection 2.4, the principal objective of the optimization framework is the derivation of cost-optimal process configurations for the production of the kerosene fraction. To incorporate both economic performance and environmental sustainability, the optimization is extended to yield Pareto optimal solutions that simultaneously account for CO₂ emissions arising from both the production and end-use combustion. The multi-objective optimization problem is addressed via the ϵ -constraint method,⁷⁶ wherein the CO₂ emissions, quantified according to the mass-balances in Subsection 2.5, are systematically constrained. The minimization of annualized CAPEX and OPEX is retained as the primary objective function.

Figure 7 presents the resulting Pareto frontier, depicted in blue, i.e., the specific kerosene production costs (left y-axis) as a function of the corresponding specific CO₂ emissions. Here, “specific” denotes normalization with respect to the mass flow rate of kerosene exiting the FT synthesis stage under the respective optimized operating conditions. Additionally, the right y-axis displays the elemental feedstock flows for both C and H, corresponding to each Pareto-optimal configuration. A third bar is included to indicate the amount of sequestered carbon (denoted as C_{sq}), originating either from direct air capture or from biogenic sources. Cost and carbon footprint of conventional Jet-A1 aviation fuel are included for comparison.^{8,13}

5.1.1 Least-cost reference design (autothermal reforming pathway)

The least-cost design configuration emerges under conditions without constraints on CO₂ emissions, when synthesis gas is generated exclusively via the ATR process. In this scenario, fossil-derived natural gas serves as the primary C and H source for the downstream production of the kerosene fraction. Due to the

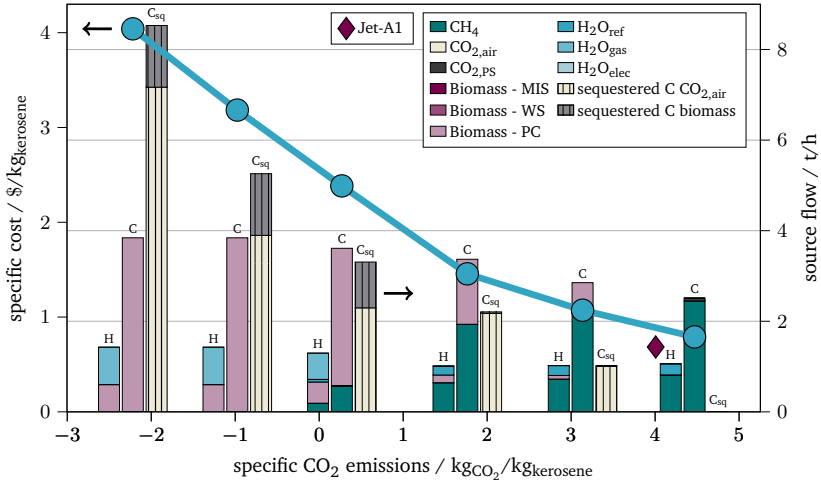


Figure 7 Pareto-optimal designs for specific kerosene cost vs. specific CO_2 emissions (left y-axis). The bars represent the source flows for carbon (C) and hydrogen (H) entering the system (right y-axis). The third bar shows sequestered carbon (C_{sq}) either from atmospheric CO_2 or biomass. As a reference, typical Jet-A1 aviation fuel is shown as a red diamond. (PS: point source; MIS: miscanthus; WS: wheat straw; PC: pine chips; ref: reforming; gas: gasification; elec: electrolysis).

inherently hydrogen-rich composition of syngas produced via ATR, a supplementary RWGS unit of limited capacity is integrated to increase the CO content by converting externally sourced CO_2 (originating from concentrated point sources) with the surplus H_2 . This H_2 originates both from the natural gas feedstock and the steam introduced during the reforming reactions. The resulting ATR-based reference configuration yields a specific production cost of approximately 0.79 \$/kg_{kerosene}, and specific CO_2 emissions of 4.47 kg CO_2 /kg_{kerosene}, accounting for both process-related (1.37 kg CO_2 /kg_{kerosene}) and end-use combustion emissions (3.10 kg CO_2 /kg_{kerosene}). Notably, the analysis does not consider further upgrading of FT products (e.g., hydrocracking), thereby excluding heavier hydrocarbon fractions that cannot be converted to kerosene within the current system boundaries. Consequently, a fraction of the hydrocarbon output is disregarded in the computation of specific cost and emissions, potentially leading to a slight overestimation of these values. Nonetheless, the cost and emission metrics for the ATR reference case agree with reported numbers for fossil-derived kerosene in existing literature.^{8,13}

5.1.2 Net zero and carbon-negative configurations

Progressively constraining CO_2 emissions results in a systematic shift in process design and a considerable increase in the specific cost of kerosene. Near the net-zero emissions point, the most cost-effective pathway is a hybrid configu-

ration that combines ATR with biomass gasification, where the majority of the C and H originate from biomass. In this case, kerosene production costs about 2.38 \$/kg_{kerosene}, which is roughly three times higher than in the unrestricted reference system. In the extreme case, characterized by negative specific CO₂ emissions, the kerosene production cost reaches 4.04 \$/kg_{kerosene}, representing an increase by a factor greater than five relative to the ATR-based reference system. Under this configuration, synthesis gas for the FT process is generated exclusively via gasification of biomass, specifically pine wood chips, thereby eliminating reliance on fossil feedstocks and substantially reducing net GHG emissions. By combining kerosene production with the removal of atmospheric and biogenic carbon, it is essentially possible to produce carbon-negative SAF.

Figure 7 elucidates that the observed reduction in specific CO₂ emissions associated with kerosene production is governed by two principal mechanisms. First, there is a progressive substitution of fossil-derived CH₄ with biomass as the primary C and H source. Along the continuum of the Pareto frontier, spanning from the cost-optimal to the carbon-negative design, hybrid process configurations emerge in which synthesis gas is co-generated via both ATR and biomass gasification in varying proportions. This compositional shift in syngas production exerts a dual impact on process-related GHG emissions. Substitution of CH₄ reduces upstream supply chain emissions associated with the fossil feedstock. Additionally, the biogenic origin of the carbon in the biomass reduces the carbon footprint, as atmospheric CO₂ is taken up during feedstock growth. Nevertheless, the intrinsic carbon neutrality of biomass alone is insufficient to achieve net zero or net-negative CO₂ emissions across the system boundary. This is in part due to the carbon footprint of electricity and heat as well as the supply chain emissions associated with the biomass. To attain further emission abatement, carbon sequestration is incrementally deployed. This system actively stores CO₂, thereby preventing its release into the atmosphere. The vertically striped bars in Figure 7 denote the sources of sequestered carbon, revealing a notable optimization outcome: the model predominantly favors the integration of DAC technology for atmospheric CO₂ extraction and subsequent storage. Any leftover CO₂ from biomass gasification is sequestered. The majority to fulfill the sequestration requirement is then covered by DAC-CS. This outcome reflects an economically rational allocation of carbon flows, prioritizing the utilization of biomass-derived carbon for synthetic fuel production, while relying on DAC to meet constraints on net CO₂ emissions.

In the absence of dedicated carbon sequestration, the mitigation of combustion emissions can be achieved solely through the biogenic carbon uptake intrinsic to biomass utilization or via the incorporation of atmospheric CO₂ through DAC. However, under the parameter assumptions employed in this study, the minimum attainable specific CO₂ emissions, without CS, are limited to 3.08 kgCO₂/kg_{kerosene}. While this value represents a reduction relative to the emissions profile of conventional Jet-A1 fuel, it remains significantly above the net zero emissions threshold. The principal constraint preventing further emissions reductions in the non-sequestration scenario arises from GHG emissions associated with the external supply of biomass, electricity and thermal energy.

If a hypothetical scenario is considered in which the provision of electricity and heat is entirely decarbonized (i.e., associated with zero CO₂ emissions) the net zero target of 0 kgCO₂/kg_{kerosene} becomes theoretically attainable. In this idealized case, atmospheric CO₂ is sourced via DAC, and H demand is met through water electrolysis powered by renewable electricity. Notably, reliance on biomass gasification alone is insufficient to achieve net zero emissions due to residual supply chain emissions associated with the harvesting, processing, and transport of various biomass feedstocks. However, if burden-free biomass (i.e., without supply chain emissions) were available, net zero could also be reached at considerably lower costs than in the DAC-based pathway, which – despite being technically feasible – remains associated with substantially higher production costs. Consequently, a system with net zero emissions necessitates either a substantial reduction of supply chain-related GHG emissions or the systematic integration of carbon sequestration technologies into the fuel production.

A more granular examination of the transition between the intermediate configurations on the Pareto frontier, specifically between the third and fourth points from the right, highlights the benefits of adaptively optimizing the operation of individual subprocesses in response to increasing CO₂ emissions constraints. This analysis reveals a progressive substitution of fossil-derived natural gas with lignocellulosic biomass, particularly pine chips, as the principal feedstock. The preferential selection of pine chips over alternative biomass types is driven by their comparatively low OPEX and their high carbon content, as detailed in Table C.1. in the Supplementary Information. To enable enhanced biogenic carbon sequestration and compliance with more rigorous emission thresholds, the gasification process is reconfigured to produce outlet gas streams with significantly elevated CO₂ mass fractions. From the fourth Pareto point onward, the syngas exiting the gasifier contains at least 47 wt % CO₂, in contrast to the ~6 wt % CO₂ observed at earlier Pareto points. The CO₂ generated in this regime is no longer utilized for synthetic fuel synthesis, it is fed to CS to reduce net emissions. The increase in CO₂ yield from gasification is facilitated by enhanced oxidation of the carbonaceous feedstock, necessitating a higher oxygen-to-biomass feed ratio. A CRD subsystem is deployed to supply the requisite additional O₂. As a result, the gasification process transitions from an oxygen-lean to an oxygen-rich regime. Specifically, the oxygen-to-biomass ratio increases from approximately 0.05 at the third Pareto point (representing the lower operational boundary) to nearly 0.3 at the fourth point, underscoring the substantial process adaptation required to meet low-emission targets through integrated carbon management.

The results depicted in Figure 7 further underscore that the utilization of renewable carbon sources (specifically biomass) is essential for achieving net zero CO₂ emissions in the production of SAFs. In the absence of biomass-based feedstocks, the optimization process favors configurations wherein synthesis gas is generated exclusively via the fossil-based ATR pathway, and CO₂ emissions are mitigated by DAC-CS. While such designs are technically capable of meeting emission constraints, they exhibit reduced economic efficiency relative to hybrid configurations incorporating biomass gasification. For instance, at the fourth Pareto-optimal point from the right, approaching net zero emissions, a

configuration relying solely on ATR-based syngas production incurs a specific kerosene production cost of $2.65 \text{ \$/kg}_{\text{kerosene}}$. In contrast, a mixed feedstock design that integrates both biomass and fossil natural gas yields a lower specific cost of $2.38 \text{ \$/kg}_{\text{kerosene}}$, representing an approximate 11% cost reduction. These findings indicate that, from both an economic and environmental perspective, biomass-enabled process routes offer a superior compromise for SAF production. Note that, as alluded to earlier, biomass supply chain emissions are assumed to be relatively high. When biomass with lower carbon footprint becomes available, biomass-based designs become more favorable compared to the fossil reference.

5.1.3 Comparative analysis of carbon supply pathways

The conclusions from Figure 7 are further substantiated by the comparative analyses presented in Figure 8, which illustrates multiple Pareto-optimal fron-

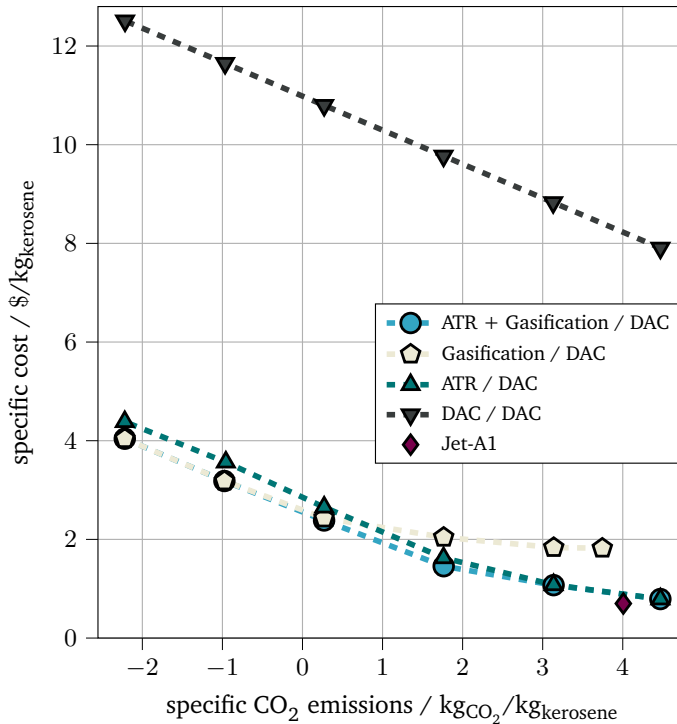


Figure 8 Pareto-optimal designs for specific kerosene cost vs. specific CO₂ emissions for different carbon sources - fossil (ATR), biogenic (gasification), atmospheric (DAC). “/ DAC” indicates that all designs require carbon sequestration to meet emissions targets. Jet-A1 aviation fuel is included for comparison. (ATR: autothermal reforming; DAC: direct air capture).

tiers corresponding to different carbon supply configurations: ATR+Gasification

(blue), Gasification-only (beige), ATR-only (green), and DAC-only (black). In all cases, low CO₂ emission targets are achievable only via DAC-CS, which is indicated by the “/ DAC”. Among these cases, the ATR+Gasification scenario (blue curve) consistently exhibits the lowest specific production costs across the full range of specific CO₂ emissions. This curve corresponds to the fully unconstrained reference Pareto front previously shown in Figure 7. Excluding the ATR process yields the Gasification-only case (beige curve), where biomass serves as the sole carbon source. While this configuration is less favorable than the blue and green cases at higher emission levels due to the relatively high capital and operational costs of biomass conversion, it becomes economically superior under emission constraints. At near net zero emissions, this biomass-based configuration achieves specific kerosene production costs of 2.43 \$/kg_{kerosene}, approximately 9 % lower than the corresponding ATR-only design reliant on DAC-CS (green curve, 2.65 \$/kg_{kerosene}). This confirms the economic and environmental advantages of integrating biomass gasification in SAF pathways targeting low emission levels. In contrast, the ATR-only case (green curve), which excludes biomass gasification, depends entirely on fossil-derived synthesis gas, with net emissions offset via DAC-CS. While production costs are comparable to the unconstrained case at high emission levels, the cost penalty increases significantly as emission constraints tighten, underscoring the diminishing economic viability of fossil-based pathways when combined with DAC-CS as the sole mitigation strategy. Finally, the DAC-only scenario (black curve) excludes both ATR and gasification, thereby relying exclusively on atmospheric CO₂ via DAC as the carbon source, and water electrolysis for H₂. This pathway exhibits the highest production costs across all emission levels, reaching up to 10.8 \$/kg_{kerosene} near net zero conditions. This substantial economic burden renders the DAC-only route uncompetitive relative to configurations incorporating natural gas or biomass. The findings underscore that cost-effective and climate-aligned SAF production depends on introducing C into the system in a thermodynamically favorable form, such as biomass or CH₄, rather than as fully oxidized CO₂. In addition, the carbon footprint of electricity plays a major role, as these supply chain emissions need to be offset by additional DAC. In summary, bio-based and fossil-plus-offset configurations yield comparable production costs at low emissions, with the biomass-based pathway being slightly more economical near net zero (2.43 \$/kg_{kerosene} vs. 2.65 \$/kg_{kerosene} for ATR+DAC). In contrast, pathways relying solely on atmospheric carbon (DAC-only) result in substantially higher costs and remain far from being competitive, highlighting the practical limitations of producing SAF from CO₂ that enters the system in an energetically less favorable form.

5.1.4 CO₂ abatement costs and policy implications

The CO₂ abatement costs presented in this study are calculated relative to the fossil-based ATR configuration (no restrictions on CO₂ emissions), which serves as the reference design. Applying the CO₂ abatement cost formulation in Eq. 55 to the gasification-only configuration at near net-zero emissions yields an esti-

mated abatement cost of approximately $390 \text{ \$/t}_{\text{CO}_2}$. This value is comparable to previously reported ranges in the literature for SAF pathways with similar technology readiness levels.^{3,8} From a policy standpoint, this benchmark indicates that a carbon price of roughly $390 \text{ \$/t}_{\text{CO}_2}$ would be required to incentivize deployment of biomass-based SAF production over fossil-derived alternatives.

Extending this analysis to the two extreme points on the Pareto front shown in Figure 7, namely the fossil-based ATR baseline and the biomass-only configuration with net-negative emissions of $-2.22 \text{ kg}_{\text{CO}_2}/\text{kg}_{\text{kerosene}}$, yields an abatement cost of $485 \text{ \$/t}_{\text{CO}_2}$, which confirms that abatement costs can also be consistently defined for negative-emission SAF designs. A detailed breakdown of CO_2 abatement costs across intermediate points along the Pareto curve is provided in the Supplementary Information accompanying this article. By contrast, process routes relying exclusively on electrolysis-based H_2 and DAC-derived CO_2 exhibit much higher specific production costs of $10.8 \text{ \$/kg}_{\text{kerosene}}$ at near-zero emissions, corresponding to abatement costs of approximately $2,380 \text{ \$/t}_{\text{CO}_2}$. These results highlight not only the significant economic advantage of biomass-based configurations but also their markedly higher cost-effectiveness in terms of avoided emissions compared to DAC-dependent pathways. Nevertheless, the viability of biomass-based approaches must be evaluated within the broader context of intersectoral competition for biomass resources, including demand from the energy, agricultural, and industrial sectors.^{57,77} To capture the implications of such supply constraints, additional Pareto-optimal process configurations were derived under varying biomass availability scenarios. These scenarios elucidate the sensitivity of outcomes to biomass feedstock limitations and highlight the diminishing cost advantage of biomass-based production as resource availability declines. Comprehensive Pareto-optimal design results under biomass supply constraints are provided in the Supplementary Information.

5.1.5 Sensitivity to key parameters

The results shown in this section are highly dependent on the parameters used, particularly with regard to CO_2 footprints of electricity, heat, and biomass. The Supplementary Information contains further emissions and costs of plant designs with varying net zero target, supply chain emissions, biomass carbon footprint, and availability of carbon sequestration.

5.2 Cost breakdown

Figure 9 presents annualized CAPEX and OPEX across three design scenarios. These include: (i) an unconstrained configuration wherein all synthesis pathways are available; (ii) a scenario excluding the ATR process ('w/o ATR'); and (iii) a configuration in which both the ATR and biomass gasification routes are omitted ("w/o ATR, Gasification"). The top part of the figure depicts the costs under unconstrained CO_2 emissions, reflecting purely cost-optimal process allocations. In contrast, the bottom part imposes a constraint of $0 \text{ kg}_{\text{CO}_2}/\text{kg}_{\text{kerosene}}$.

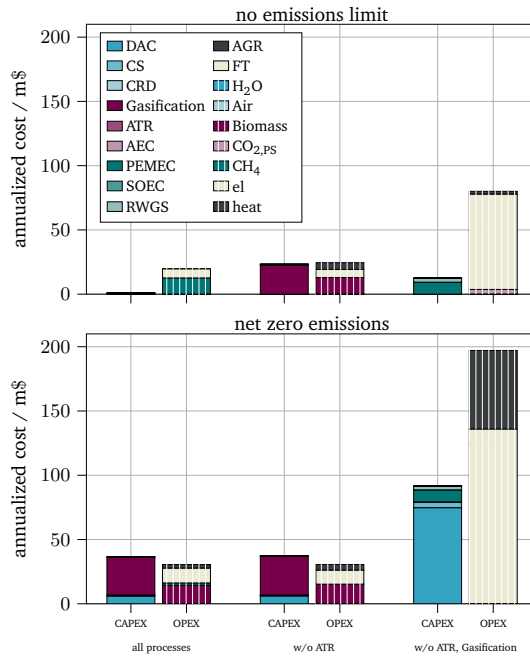


Figure 9 Breakdown of annual CAPEX and OPEX for kerosene production designs. The top diagram shows the cost breakdowns for three different cases without restrictions on CO₂ emissions. On the far left design, no processes are excluded in advance, while in the other two cases first the autothermal reforming (ATR) process and finally both the ATR and the gasification process are excluded. The diagram below shows the cost breakdowns for the same three cases, but the greenhouse gas (GHG) emissions are restricted to approximately 0 kgCO₂/kgkerosene. (DAC: direct air capture; CS: carbon sequestration; CRD: cryogenic distillation; ATR: autothermal reforming; AEC: alkaline electrolyzer; PEMEC: proton-exchange membrane electrolyzer; SOEC: solid-oxide electrolyzer; RWGS: reverse water-gas shift; AGR: acid gas removal ; FT: Fischer-Tropsch; PS: point source; el: electricity).

An examination of the top diagram in Figure 9, corresponding to the scenario without CO₂ emission constraints, reveals that, under the configuration with all processes included, the process design is exclusively reliant on ATR for synthesis gas production. In this configuration, OPEX, primarily driven by CH₄ as the reforming feedstock, constitute the dominant share of the total annualized costs. Upon exclusion of the ATR process, a substantial increase in annual CAPEX is observed, attributable to the capital-intensive biomass gasification infrastructure. In the scenario wherein both the ATR and gasification routes are omitted, the H₂ required for FT synthesis must be supplied entirely via water electrolysis. Concurrently, CO is generated by catalytically activating captured CO₂ through the RWGS reaction, necessitating additional H₂ input. In the absence of carbon constraints, the use of CO₂ from concentrated point sources emerges as the

most cost-effective carbon feedstock. As indicated in Figure 9, the pronounced increase in total system costs for electrolysis-based process routes is caused by the substantial electrical energy demand.

The bottom diagram in Figure 9 reflects scenarios constrained to approximately net zero CO₂ emissions. In the case of the far left configuration, biomass is employed as the principal C and H source for synthesis gas generation, with fossil CH₄ contributing only marginally. In this case, annualized CAPEX and OPEX are nearly equivalent. Exclusion of the ATR process exerts minimal influence on the overall process configuration, as its installed capacity in the first case is already marginal. A comparative assessment of the "w/o ATR" scenarios between the top (no emissions limit) and bottom (net zero emissions) diagrams reveals that the primary distinction lies in the implementation of a DAC-CS combination in the bottom case, which is necessary to meet GHG reduction targets through atmospheric carbon removal. In contrast, achieving net zero emissions without the utilization of biomass (i.e., under the dual exclusion of both ATR and gasification pathways) incurs a dramatic increase in both CAPEX and OPEX. In such a configuration, all H₂ required for FT synthesis must be generated via water electrolysis, resulting in exceptionally high electricity demand, similar to that observed in the unconstrained scenario. However, unlike the top diagram where point-source CO₂ remains viable, the net zero constraint necessitates atmospheric CO₂ exclusively via DAC. This not only increases the electrical energy requirement but also introduces significant thermal energy demand for the desorption stage of the DAC system. Consequently, the combined effect of intensive electricity consumption for electrolysis and the thermal requirements of DAC culminates in exceptionally elevated total annualized costs, rendering the biomass-free, net zero SAF production route economically disadvantageous under the given assumptions.

5.3 Fixed vs. adaptable design

In most superstructure optimization studies, process variables (e.g., reactor temperature, pressure, inlet composition) are fixed prior to optimization,^{3,16,21,33,34} which implies that individual subprocesses cannot respond to varying external conditions such as changing energy prices or resource availability. As a result, important adjustment potentials remain unexploited. The benefits of allowing the subprocesses to adjust have been previously demonstrated in Subsection 5.1. These advantages are made accessible only through the integration of ANNs into the superstructure optimization framework, which enables the inclusion of varying operating modes and decision variables at both the plant wide and individual process unit levels. To further elucidate the impact of incorporating these additional degrees of freedom, a sensitivity analysis is performed comparing two scenarios: an "adaptable case", in which the input and output parameters of the embedded ANNs are optimized to respond to changing external conditions, and a "fixed case", where process parameters such as pressure, temperature, and inlet compositions are predetermined and held constant throughout the optimization.

For this analysis, the ATR process is excluded a priori, and no constraints are imposed on CO₂ emissions.

Figure 10 presents the resulting specific kerosene production costs as a function of electricity price, varied within the range of 0 \$/kWh to 0.2 \$/kWh. The

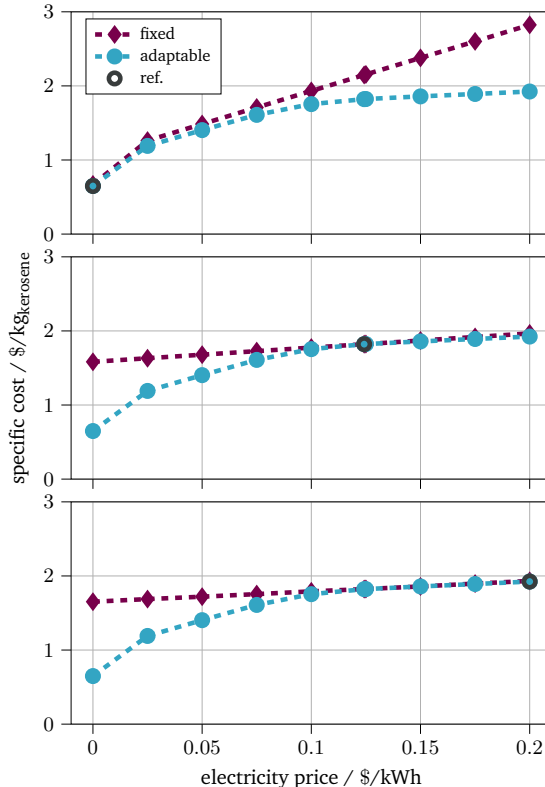


Figure 10 Results of the sensitivity analysis for the specific kerosene production costs as a function of the electricity price for the adaptable (blue) and the fixed case (red). In the adaptable case, all decision variables at plant and process unit level (e.g., pressure, temperature, inlet compositions) of the processes that are represented via ANNs are taken into account. In the fixed case, these degrees of freedom are fixed in advance, depending on the reference case (ref.), and are not part of the actual optimization. All results are generated excluding the autothermal reforming (ATR) process and there are no restrictions regarding CO₂ emissions.

blue curves correspond to the adaptable case, incorporating multiple operational decision variables at the plant and process unit levels (e.g., variations in pressure, temperature, and inlet compositions). In contrast, the red curves represent the fixed case, where these additional degrees of freedom are omitted. For comparative purposes, selected operating points from the adaptable case are used to define the fixed process conditions, indicated as black unfilled reference markers

in Figure 10. Specifically, the top, middle, and bottom subplots show the fixed case using process conditions derived from the adaptable solutions at electricity prices of 0 \$/kWh, 0.124 \$/kWh, and 0.2 \$/kWh, respectively.

The results reveal a distinct nonlinear relationship between the specific cost of kerosene production and electricity price. In the adaptable case, costs range from approximately 0.65 \$/kg_{kerosene} at 0 \$/kWh to 1.92 \$/kg_{kerosene} at 0.2 \$/kWh, with diminishing sensitivity at higher electricity prices. Across all subplots, the adaptable case consistently shows lower costs than the fixed case. In several instances, the adaptable configuration achieves more than 20 % cost savings relative to the fixed scenario. These findings highlight the critical value of simultaneously optimizing system-level design and process-level operating conditions.

To elucidate the mechanisms underlying the superior economic performance of the adaptable case, a detailed evaluation of the optimal operating conditions for the biomass gasification and FT synthesis processes as a function of electricity price is presented. The top diagram of Figure 11 illustrates the optimal FT reactor pressure (left y-axis) and the corresponding molar H₂/CO ratio at the reactor inlet (right y-axis). The bottom diagram depicts the gasification temperature (left y-axis) and the mass-based steam-to-biomass ratio (right y-axis). In the hypothetical scenario where electricity is available at no cost (0 \$/kWh), the synthesis gas is entirely derived from water electrolysis in conjunction with CO₂ activation via the RWGS reaction. Under such conditions, biomass gasification is rendered superfluous and thus omitted from the process configuration. The favorable H₂ availability allows operation of the FT synthesis at an elevated inlet H₂/CO molar ratio of approximately 2.16. However, a high H₂/CO ratio shifts the ASF product distribution towards lower molecular weight hydrocarbons. To counteract this effect and steer the hydrocarbon product distribution back towards the desired kerosene-range fraction (C₈–C₁₆), the FT reactor is operated at an increased pressure (approximately 44 bar), a condition made feasible by the negligible cost of electricity. As electricity prices increase, a transition in both process configuration and operating strategy is observed. The synthesis gas supply gradually shifts from electrolysis and RWGS to biomass gasification. At moderately low electricity prices, a hybrid strategy is employed wherein gasification supplements electrolysis. In this regime, gasification is optimized for high carbon monoxide yield, favoring elevated temperatures and reduced steam-to-biomass ratios. However, once the electricity price exceeds approximately 0.075 \$/kWh, the economic viability of electrolysis-derived H₂ diminishes significantly. At this point, biomass gasification must solely meet the requirements of the FT synthesis. To achieve a synthesis gas composition conducive to high kerosene yields, the gasifier operating temperature is reduced and the steam-to-biomass ratio is increased, promoting enhanced H₂ formation—up to 7 % by mass in the product gas. With rising electricity prices, two additional parallel trends emerge. First, syngas compression becomes a major contributor to OPEX, making it optimal to reduce the FT reactor pressure to approximately 30 bar. At such lower pressures, product selectivity shifts toward lighter hydrocarbons. Second, the optimal H₂/CO molar ratio decreases to around 1.82, reflecting the reduced hydrogen

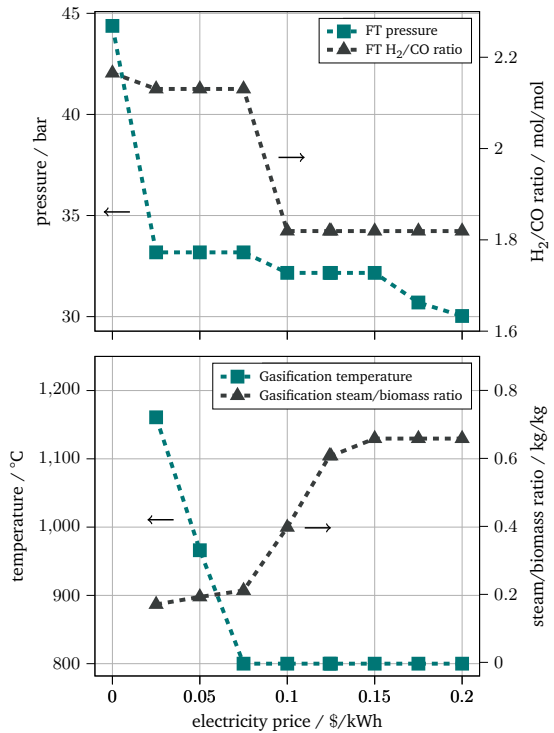


Figure 11 Selected optimal operating parameters of the gasification and Fischer-Tropsch (FT) processes as a function of the electricity price. The top diagram shows the pressure of the FT process (green) and the molar H₂/CO ratio in the inlet (black). The bottom diagram illustrates the temperature of the biomass gasification (green) and the mass-based steam to biomass ratio (black).

content in the syngas as a consequence of high electricity-driven hydrogen costs. Because these trends act in opposite directions with respect to product selectivity, their combined effect allows to maintain favorable yields in the kerosene range.

The results presented in Figure 11 demonstrate the substantial variability in optimal process configurations, not only with respect to the selected processes and their installed capacities, but also in terms of the operation of those processes. These variations are strongly influenced by external parameters, such as electricity pricing and CO₂ emission constraints. It is evident that the process set points, including temperature, pressure, and inlet composition, must be adapted to prevailing techno-economic conditions to ensure cost-effective system performance. In contrast, constraining these operational variables to static values, independent of external influences, can result in suboptimal plant performance and increased specific production costs, as quantified in Figure 10.

5.4 Heat integration

Subsection 2.3 presents an advanced formulation for process level heat integration, in which discrete thermal sources and sinks are defined for each process within the overall synthesis pathway. To quantitatively assess the influence of heat integration on the specific production costs of sustainable kerosene, a parametric sensitivity analysis is conducted with respect to the unit cost of externally supplied thermal energy. The results are depicted in Figure 12, wherein the external heat price is varied between 0 \$/kWh and 0.2 \$/kWh. All scenarios

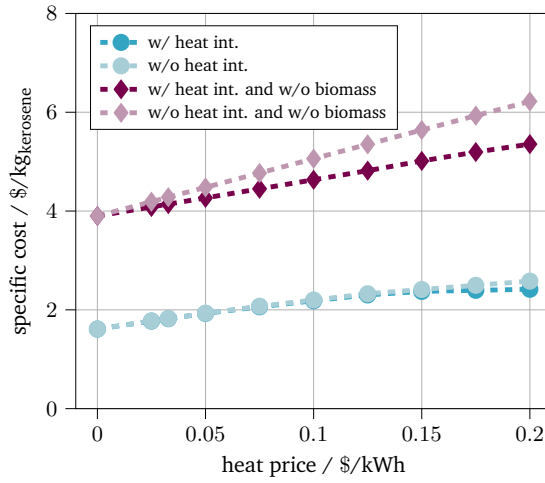


Figure 12 Results of the sensitivity analysis for the specific kerosene production costs as a function of the heat price. The blue curves represent the kerosene costs, once with (w/ heat int.) and once without heat integration (w/o heat int.). The red lines show the same trends, but excluding the use of biomass gasification (w/o biomass) and CO₂ from point sources. All results are generated excluding the autothermal reforming (ATR) process and there are no restrictions regarding CO₂ emissions.

exclude the ATR process and impose no constraints on CO₂ emissions. The blue data points represent cost for system configurations both with (dark blue) and without (light blue) the implementation of heat integration. Costs shown in red correspond to designs that omit the use of biomass as a feedstock and exclude CO₂ from industrial point sources (“w/o biomass”).

Analyzing the costs represented by the blue curve including heat integration, the specific kerosene production costs range from 1.61 \$/kg_{kerosene} at a heat price of 0 \$/kWh to 2.42 \$/kg_{kerosene} at 0.2 \$/kWh, corresponding to an approximate 50 % increase in production costs attributable to the rising cost of externally supplied thermal energy. The light blue curve, which reflects system configurations without thermal integration, follows a comparable trend. At the upper bound of heat prices, the specific cost increases to 2.58 \$/kg_{kerosene}, indicating that heat integration achieves a marginal cost reduction of only 7 %. This limited cost

differential is primarily attributable to the underlying plant design. In both cases, synthesis gas is produced via biomass gasification. Given the constraints imposed by the minimum temperature approach for heat exchange, the only significant thermal integration potential lies between the initial endothermic decomposition step of biomass and the subsequent exothermic gasification step, provided that the gasifier operates under conditions conducive to net heat release. In the absence of heat integration, the sole deviation is the need for external thermal energy input to support biomass decomposition, leading to a modest rise in overall production costs. Thus, under these specific design and operational conditions, the economic incentive for implementing thermal integration remains limited.

In contrast, when the utilization of biomass, point source-derived CO₂, and the ATR process are entirely excluded from the system configuration, the significance of thermal integration becomes markedly pronounced. Under these constraints, all carbon required for FT synthesis must be supplied via atmospheric CO₂, necessitating the deployment of a DAC process. The DAC system imposes a substantial thermal demand, particularly for the desorption phase, which operates at approximately 100 °C. The inherently exothermic nature of the FT synthesis reaction presents a favorable opportunity for thermal integration, enabling recovery and utilization of waste heat to satisfy the DAC heat requirements. In scenarios where heat integration is not considered, the thermal energy demand for CO₂ capture must be fulfilled through external heat supply. A comparative analysis of the two extreme cases, at a heat price of 0.2 \$/kWh, reveals that the specific kerosene production cost increases from 5.35 \$/kg_{kerosene} (with heat integration) to 6.22 \$/kg_{kerosene} (without integration), corresponding to an approximate 14 % cost reduction due to internal heat integration. More broadly, the magnitude of cost deviation between the heat-integrated and non-integrated configurations is consistently greater for the red curves compared to the blue curves, indicating a stronger dependence on thermal integration in systems relying solely on atmospheric CO₂ as the carbon source. This underscores the conclusion that while the benefit of heat integration is design-dependent, it becomes critically important in process configurations characterized by high thermal demand and limited internal heat sources.

Conclusions and outlook

This work introduces an advanced multi-objective superstructure optimization framework considering component mixtures, that integrates ANNs within a MIQCP formulation. By modelling mixtures and embedding data-driven surrogate models into the mathematical optimization structure, the proposed methodology overcomes the inherent limitations of conventional superstructure-based approaches reported in the literature. Specifically, the framework enables the consideration of variable input and output stream compositions, thereby allowing for the simultaneous optimization of process configurations and target product composition. Moreover, the formulation captures complex, nonlinear

input–output relationships of individual process units and facilitates the joint optimization of both discrete system-level decisions (e.g., process selection and capacity allocation) and continuous process operating parameters (e.g., pressure, temperature, and feed composition).

The optimization results indicate that, in the absence of CO₂ emission constraints, least-cost process configurations are characterized by the exclusive deployment of the fossil-based ATR route. This yields low specific production costs for kerosene (~0.79 \$/kg_{kerosene}), but is associated with elevated specific greenhouse gas emissions on the order of 4.47 kg_{CO₂}/kg_{kerosene}. Constraints on carbon emissions necessitate the integration of biomass gasification in conjunction with CO₂ removal via DAC-CS. These system configurations result in significantly higher production costs exceeding 2.3 \$/kg_{kerosene}, while simultaneously achieving substantial reductions in net CO₂ emissions. When supply chain emissions are taken into account, achieving net zero CO₂ emissions is infeasible through biomass utilization alone and carbon sequestration is required.

Furthermore, CO₂ abatement costs (~390 \$/t_{CO₂}) align well with literature values, indicating that high carbon pricing would be required to render bio-based SAF production economically competitive. The analysis highlights that mixed feedstock approaches (e.g., combining natural gas and pine chips) offer optimal trade offs between costs and emissions (~2.38 \$/kg_{kerosene} at near zero CO₂). At zero emissions, a bio-based system is slightly less costly than a combination of synthesis from natural gas and offsets via DAC-CS, while a system reliant on atmospheric carbon is around five times as expensive.

Crucially, the study underlines the value of simultaneous optimization of superstructure topology and process parameters. Designs that leverage flexible process parameters—enabled by embedded ANNs—consistently outperform fixed configurations, achieving up to 20 % cost savings. Sensitivity studies show how operating conditions such as FT reactor pressure and gasification temperature respond to external factors such as electricity prices.

Several limitations inherent to the present study warrant further investigation in subsequent research. Primarily, the optimization of the ANN input and output variables is contingent upon the accuracy and fidelity of the underlying process simulations performed in Aspen Plus®.¹⁵ In particular, the FT reactor is modeled using an empirical surrogate, which could be substituted with a more mechanistically rigorous model to enhance the predictive accuracy of product distribution as a function of key operating parameters. Moreover, only three subprocesses within the superstructure are represented via embedded ANN surrogates. This restriction arises from the increase in computational complexity associated with the inclusion of additional binary decision variables, particularly those introduced by the ReLU ANNs. Future research should aim to improve the computational tractability of the mixed-integer optimization problem, thereby enabling the integration of a larger number of data-driven surrogate models. From a process systems engineering standpoint, the scope of this study is limited to the production of the kerosene fraction of the FT product stream, with a specific focus on linear alkanes (n-alkanes) as the primary target compounds. For a more comprehensive understanding of SAF production pathways, downstream

upgrading processes (such as hydrocracking and hydrogenation) should be incorporated. Additionally, alternative synthesis routes, such as the MtJ pathway, could be explored. This would also enable consideration of a more diverse set of hydrocarbon products, including iso-alkanes and cyclo-alkanes, yielding a product composition that more closely aligns with fuel specifications.

Author contributions

Alexander Klimek: conceptualization, methodology, software, data curation, original draft; **Christoph Plate:** methodology, software; **Sebastian Sager:** methodology, supervision, resources; **Kai Sundmacher:** supervision, resources, review & editing; **Caroline Ganzer:** conceptualization, methodology, supervision, review & editing

Conflicts of interest

There are no conflicts to declare.

Data availability

The data supporting this article have been included as part of the Supplementary Information.

Acknowledgements

We acknowledge financial support from the research initiative "SmartProSys: Intelligent Process Systems for the Sustainable Production of Chemicals" funded by the Ministry for Science, Energy, Climate Protection and the Environment of the State of Saxony-Anhalt, from the European Regional Development Fund (grant Center for Dynamic Systems) under the European Union's Horizon Europe Research and Innovation Program, and from the German Research Foundation DFG within the priority program 2331 "Machine Learning in Chemical Engineering" under grant SA 2016/3-1.

The authors would like to thank **Manuel Garcia-Perez** for his helpful inputs regarding the modeling of gasification processes.

OpenAI's ChatGPT was utilized to aid the development of code and to improve the writing of this manuscript. All outputs were carefully reviewed and edited by the authors to ensure accuracy and scientific rigor.

References

- [¹] D. R. Vardon, B. J. Sherbacow, K. Guan, J. S. Heyne and Z. Abdullah, *Joule*, 2022, **6**, 16–21.
- [²] A. Bauen, N. Bitossi, L. German, A. Harris and K. Leow, *Johnson Matthey Technology Review*, 2020, **64**, 263–278.
- [³] A. Gonzalez-Garay, C. Heuberger-Austin, X. Fu, M. Klokkenburg, D. Zhang, A. van der Made and N. Shah, *Energy & Environmental Science*, 2022, **15**, 3291–3309.
- [⁴] D. Freire Ordóñez, T. Halldanarson, C. Ganzer, N. Shah, N. Mac Dowell and G. Guillén-Gosálbez, *Sustainable Energy & Fuels*, 2022, **6**, 4749–4764.
- [⁵] ASTM International, *Specification for Aviation Turbine Fuel Containing Synthesized Hydrocarbons*, <https://store.astm.org/d7566-22.html>.
- [⁶] J. Holladay, Z. Abdullah and J. Heyne, *Sustainable Aviation Fuel: Review of Technical Pathways*, U.S. Department of Energy, 2020.
- [⁷] S. Bube, S. Voß, G. Quante and M. Kaltschmitt, *Fuel*, 2025, **384**, 133901.
- [⁸] O. Salem, *Energy Technology*, 2023, **11**, 2300348.
- [⁹] R. Sacchi, V. Becattini, P. Gabrielli, B. Cox, A. Dirnachner, C. Bauer and M. Mazzotti, *Nature Communications*, 2023, **14**, 3989.
- [¹⁰] T. N. Do, C. You and J. Kim, *Energy & Environmental Science*, 2022, **15**, 169–184.
- [¹¹] F. G. Albrecht, D. H. König, N. Baucks and R.-U. Dietrich, *Fuel*, 2017, **194**, 511–526.
- [¹²] S. Bube, N. Bullerdiek, S. Voß and M. Kaltschmitt, *Fuel*, 2024, **366**, 131269.
- [¹³] S. Voß, S. Bube and M. Kaltschmitt, *Energy & Fuels*, 2024, **38**, 5263–5278.
- [¹⁴] V. Eyberg, V. Dieterich, S. Bastek, M. Dossow, H. Spliethoff and S. Fendt, *Energy Conversion and Management*, 2024, **315**, 118728.
- [¹⁵] Aspen Technology Inc, *Aspen Plus*, 24.08.2023, <https://www.aspentechn.com/en/products/engineering/aspen-plus>.
- [¹⁶] C. D. Demirhan, W. W. Tso, J. B. Powell and E. N. Pistikopoulos, *Applied Energy*, 2021, **281**, 116020.
- [¹⁷] M. Martín and I. E. Grossmann, *Applied Energy*, 2018, **213**, 595–610.
- [¹⁸] Q. Zhang, M. Martín and I. E. Grossmann, *Computers & Chemical Engineering*, 2018, **122**, 80–92.
- [¹⁹] P. Kenkel, T. Wassermann and E. Zondervan, *Processes*, 2021, **9**, 1348.
- [²⁰] J. M. Restrepo-Flórez and C. T. Maravelias, *Energy & Environmental Science*, 2021, **14**, 493–506.
- [²¹] A. M. Niziolek, O. Onel and C. A. Floudas, *Computers & Chemical Engineering*, 2017, **102**, 169–187.
- [²²] W. Wu, C. A. Henao and C. T. Maravelias, *AIChE Journal*, 2016, **62**, 3199–3214.
- [²³] B. Wang, B. H. Gebreslassie and F. You, *Computers & Chemical Engineering*, 2013, **52**, 55–76.
- [²⁴] K. McBride and K. Sundmacher, *Chemie Ingenieur Technik*, 2019, **91**, 228–239.
- [²⁵] I. Fahmi and S. Cremaschi, *Computers & Chemical Engineering*, 2012, **46**,

- 105–123.
- [26] C. A. Henao and C. T. Maravelias, *AIChE Journal*, 2011, **57**, 1216–1232.
 - [27] A. M. Schweidtmann and A. Mitsos, *Journal of Optimization Theory and Applications*, 2018, **180**, 925–948.
 - [28] A. M. Schweidtmann, D. Bongartz and A. Mitsos, *Book Chapter: Optimization with Trained Machine Learning Models Embedded*, In: *Encyclopedia of Optimization*, Springer Nature Switzerland, Cham, 2022.
 - [29] J. Granacher, I. D. Kantor and F. Maréchal, *Frontiers in Chemical Engineering*, 2021, **3**, 778876.
 - [30] H. A. Pedrozo, S. B. Rodriguez Reartes, Q. Chen, M. S. Diaz and I. E. Grossmann, *Computers & Chemical Engineering*, 2020, **141**, 107015.
 - [31] Z. Hao, C. Zhang and A. A. Lapkin, *AIChE Journal*, 2022, **68**, 1–15.
 - [32] C. Plate, M. Hahn, A. Klimek, C. Ganzer, K. Sundmacher and S. Sager, *An analysis of optimization problems involving ReLU neural networks*, <http://arxiv.org/pdf/2502.03016v1>.
 - [33] C. Ganzer and N. Mac Dowell, *Sustainable Energy & Fuels*, 2020, **4**, 3888–3903.
 - [34] T. Svitnič and K. Sundmacher, *Applied Energy*, 2022, **326**, 120017.
 - [35] Gurobi Optimization, *The Leader in Decision Intelligence Technology - Gurobi Optimization*, 2023, <https://www.gurobi.com/>.
 - [36] D. C. Rosenfeld, H. Böhm, J. Lindorfer and M. Lehner, *Renewable Energy*, 2020, **147**, 1511–1524.
 - [37] O. Onel, A. M. Niziolek, J. A. Elia, R. C. Baliban and C. A. Floudas, *Industrial & Engineering Chemistry Research*, 2015, **54**, 359–385.
 - [38] W. Doherty, A. Reynolds and D. Kennedy, *Book Chapter: Aspen Plus Simulation of Biomass Gasification in a Steam Blown Dual Fluidised Bed*, In: *Materials and Processes for Energy: Communicating Current Research and Technological Developments*, Formatec Research Centre, 2013.
 - [39] A. H. Tanzil, K. Brandt, M. Wolcott, X. Zhang and M. Garcia-Perez, *Biomass and Bioenergy*, 2021, **145**, 105942.
 - [40] S. Yang, B. Li, J. Zheng and R. K. Kankala, *Journal of Cleaner Production*, 2018, **205**, 364–374.
 - [41] D.-Y. Peng and D. B. Robinson, *Industrial & Engineering Chemistry Fundamentals*, 1976, **15**, 59–64.
 - [42] J. Boston and P. Mathias, *Proceedings of the 2nd International Conference on Phase Equilibria and Fluid Properties in the Chemical Process Industries*, 1980.
 - [43] A. A. K T, S. Poyilil, M. C and A. P, *Process Integration and Optimization for Sustainability*, 2023, **7**, 255–268.
 - [44] O. Y. Elsernagawy, A. Hoadley, J. Patel, T. Bhatelia, S. Lim, N. Haque and C. Li, *Journal of CO₂ Utilization*, 2020, **41**, 101280.
 - [45] *Greener Fischer-Tropsch processes for fuels and feedstocks*, ed. P. M. Maitlis and A. de Klerk, Wiley-VCH Verlag & Co. KGaA, Weinheim, 2013.
 - [46] C. Sun, Z. Luo, A. Choudhary, P. Pfeifer and R. Dittmeyer, *Industrial & Engineering Chemistry Research*, 2017, **56**, 13075–13085.
 - [47] R. Yang, L. Zhou, J. Gao, X. Hao, B. Wu, Y. Yang and Y. Li, *Catalysis Today*, 2017, **298**, 77–88.

- [48] C. Hamelinck, A. Faaij, H. den Uil and H. Boerrigter, *Energy*, 2004, **29**, 1743–1771.
- [49] A. de Klerk, *Fischer-Tropsch Refining*, Wiley, 2011.
- [50] N. Böcker, M. Grahl, A. Tota, P. Häussinger, P. Leitgeb and B. Schmücker, *Ullmann's Encyclopedia of Industrial Chemistry*, Wiley-VCH, 7th edn, 2010, pp. 1–27.
- [51] M. J. Palys and P. Daoutidis, *Computers & Chemical Engineering*, 2022, **165**, 107948.
- [52] Climeworks, *Capturing CO₂ from air*, 25.02.2025, <https://climeworks.com/carbon-removal-technology>.
- [53] M. Fasihi, O. Efimova and C. Breyer, *Journal of Cleaner Production*, 2019, **224**, 957–980.
- [54] S. Shiva Kumar and V. Himabindu, *Materials Science for Energy Technologies*, 2019, **2**, 442–454.
- [55] A. Buttler and H. Spliethoff, *Renewable and Sustainable Energy Reviews*, 2018, **82**, 2440–2454.
- [56] J. Kim, J. Park, M. Qi, I. Lee and I. Moon, *Industrial & Engineering Chemistry Research*, 2021, **60**, 7257–7274.
- [57] T. Svitnič, K. Beer, K. Sundmacher and M. Böcher, *Sustainable Production and Consumption*, 2024, **44**, 123–150.
- [58] A. O. Oni, K. Anaya, T. Giwa, G. Di Lullo and A. Kumar, *Energy Conversion and Management*, 2022, **254**, 115245.
- [59] X. Liu, S. Yang, Z. Hu and Y. Qian, *Computers & Chemical Engineering*, 2015, **83**, 48–57.
- [60] M. Gatti, E. Martelli, F. Marechal and S. Consonni, *Applied Thermal Engineering*, 2014, **70**, 1123–1140.
- [61] I. Sharma, A. F. Hoadley, S. M. Mahajani and A. Ganesh, *Journal of Cleaner Production*, 2016, **119**, 196–206.
- [62] F. A. N. Fernandes, *Chemical Engineering & Technology*, 2006, **29**, 449–453.
- [63] I. M. Mujtaba, N. Aziz and M. A. Hussain, *Chemical Engineering Research and Design*, 2006, **84**, 635–644.
- [64] M. Fischetti and J. Jo, *Constraints*, 2018, **23**, 296–309.
- [65] R. Anderson, J. Huchette, W. Ma, C. Tjandraatmadja and J. P. Vielma, *Mathematical Programming*, 2020, **183**, 3–39.
- [66] B. Grimstad and H. Andersson, *Computers & Chemical Engineering*, 2019, **131**, 106580.
- [67] F. Ceccon, J. Jalving, J. Haddad, A. Thebelt, C. Tsay, C. D. Laird and R. Misener, *Journal of Machine Learning Research*, 2022, **23**, 1–8.
- [68] M. L. Bynum, G. A. Hackebeil, W. E. Hart, C. D. Laird, B. L. Nicholson, J. D. Siirola, J.-P. Watson and D. L. Woodruff, *Pyomo - optimization modeling in Python*, Springer, Cham, Third edition edn, 2021, vol. volume 67.
- [69] W. E. Hart, J.-P. Watson and D. L. Woodruff, *Mathematical Programming Computation*, 2011, **3**, 219–260.
- [70] L. Lu, C. M. Anderson-Cook, M. Martin and T. Ahmed, *Quality and Reliability Engineering International*, 2022, **38**, 1165–1188.
- [71] S. Ascher, W. Sloan, I. Watson and S. You, *Applied Energy*, 2022, **320**,

119289.

- [⁷²] E. I. Sanchez Medina, S. Linke, M. Stoll and K. Sundmacher, *Digital Discovery*, 2022, **1**, 216–225.
- [⁷³] KerasTeam, *Keras: Deep Learning for Humans*, 10.01.2024, <https://keras.io/>.
- [⁷⁴] C. Tsay, J. Kronqvist, A. Thebelt and R. Misener, *Partition-based formulations for mixed-integer optimization of trained ReLU neural networks*, Advances in Neural Information Processing Systems 34 (NeurIPS 2021), <https://arxiv.org/pdf/2102.04373.pdf>.
- [⁷⁵] D. P. Kingma and J. Ba, *Adam: A Method for Stochastic Optimization*, <https://arxiv.org/pdf/1412.6980>.
- [⁷⁶] Y. H. Yv, L. S. Lasdon and D. Da, *IEEE Transactions on Systems, Man, and Cybernetics*, 1971, 296–297.
- [⁷⁷] K. Beer, M. Böcher, C. Ganzer, A. Blöbaum, L. Engel, T. de Paula Sieverding, K. Sundmacher and E. Matthies, *Forest Policy and Economics*, 2025, **177**, 103521.

Electronic Supplementary Information. Superstructure Optimization with Embedded Neural Networks for Sustainable Aviation Fuel Production.

Alexander Klimek,^a Christoph Plate,^{bc} Sebastian Sager,^{bc} Kai Sundmacher^{ad} and
Caroline Ganzer^{*a}

^a Max Planck Institute for Dynamics of Complex Technical Systems, Department of Process Systems
Engineering, Sandtorstr. 1, 39106 Magdeburg, Germany.

^b Max Planck Institute for Dynamics of Complex Technical Systems, Mathematical Optimization and
Machine Learning Group, Sandtorstr. 1, 39106 Magdeburg, Germany.

^c Otto von Guericke University, Chair of Mathematical Algorithmic Optimization, Universitätsplatz 2,
39106 Magdeburg, Germany.

^d Otto von Guericke University, Chair for Process Systems Engineering, Universitätsplatz 2, 39106
Magdeburg, Germany.

*corresponding author; E-mail: cganzer@mpi-magdeburg.mpg.de

A. Data

A.1. Nomenclature

Greek symbols

	description	unit
α	chain growth probability	— or %
β	specific CAPEX	\$/capacity
Γ	process scale	kg/h
γ	specific OPEX	\$/kg or \$/kWh
ΔT	temperature difference	K or °C
δ	specific energy	MJ/kg
ϵ	binary variable for the activation status of an ANN neuron	—
θ	project lifetime	years
λ	specific CO ₂ -equivalent emission intensities	kgCO ₂ -eq/kg or kgCO ₂ -eq/kWh
ν	specific consumption/production	kg/h/reference capacity
σ	activation function of an ANN	—
τ	annual plant operating time	h

Latin symbols

	description	unit
b	bias vector of an ANN	—
CF	correction factor	—
CR	capital recovery factor	—

	description	unit
e	specific work/electricity generation/consumption	kW/reference capacity
f	function	—
K	cost	\$
k	specific cost	\$/kg
\dot{M}	mass flow	kg/h
n	number of carbon atoms	—
p	pressure	bar
\dot{Q}	thermal duty	kW
q	specific heat generation/consumption	kW/reference capacity
r	interest rate	— or %
S	selectivity	— or %
T	temperature	K
W	weight matrix of an ANN	—
\dot{W}	work/electricity flow	kW
w	mass fraction	—
x	binary variable for the selection of a biomass type/mole fraction/vector of ANN inputs	—
y	binary variable for the decision whether to install a process or not	—
z	binary variable that indicates whether a heat exchange link is active or not	—

Sets

	description
\mathcal{C}	set of components
$\mathcal{C}^{\text{biomass}}$	set of different biomass types
$\mathcal{C}^{\text{diesel}}$	set of hydrocarbons considered as diesel fraction
$\mathcal{C}^{\text{gasoline}}$	set of hydrocarbons considered as gasoline fraction
\mathcal{C}^{HC}	set of hydrocarbons considered as FT output

	description
\mathcal{C}^K	set of key reaction components
$\mathcal{C}^{\text{kerosene}}$	set of hydrocarbons considered as kerosene fraction
\mathcal{C}^{src}	set of source components
\mathcal{H}	set of possible process heat sources/sinks
\mathcal{I}	set of possible process inlet ports
\mathcal{J}	set of processes
\mathcal{J}^{ANN}	set of processes represented via an artificial neural network
$\mathcal{J}^{\text{heat}}$	set of suitable processes for heat integration
$\mathcal{J}^{\text{heat,cold}}$	set of process heat sinks for heat integration
$\mathcal{J}^{\text{heat,hot}}$	set of process heat sources for heat integration
$\mathcal{J}^{\text{heat,s}}$	set of process heat sources/sinks for heat integration
\mathcal{J}^I	set of existing process inlet ports
\mathcal{J}^O	set of existing process outlet ports
\mathcal{J}^{OI}	set of existing connections between process outlet and inlet ports
\mathcal{O}	set of possible process outlet ports

Superscript and subscript indices

	description
α	index for components
h	index for heat sources/sinks
i	index for process inlet ports/neurons within an ANN/ANN inputs
j	index for processes
l	index for ANN layers
n	index for number of carbon atoms
o	index for process outlet ports/ANN outputs
ANN	artificial neural network
ab	abatement
cap	CAPEX
comp	component
el	electricity
elec	electrolysis

	description
eq	equivalent
flow	flow
gas	gasification
HC	hydrocarbon
in	inlet
kerosene	kerosene
op	OPEX
out	outlet
ref	reforming
sq	sequestered
src	source
tot	total

Acronyms and abbreviations

	description
AEC	alkaline electrolysis cells
AGR	acid gas removal
ANN	artificial neural network
API	application programming interface
ASF	Anderson-Schulz-Flory
ASTM	American Society for Testing and Materials
ASU	air separation unit
ATJ	alcohol-to-jet
ATR	autothermal reforming
CAPEX	capital expenditure
CRD	cryogenic distillation
CS	carbon sequestration
DAC	direct air capture
FC	fixed carbon
FT	Fischer-Tropsch
GHG	greenhouse gas
HEFA	hydroprocessed esters and fatty acids
heat int.	heat integration

	description
LB	lower bound
LHS	latin hypercube sampling
MAE	mean absolute error
MAPE	mean absolute percentage error
MILP	mixed-integer linear programming
MINLP	mixed-integer nonlinear programming
MIQCP	mixed-integer quadratically constrained programming
MIS	misanthus
MSE	mean squared error
MtJ	methanol-to-jet
MtO	methanol-to-olefins
OMLT	Optimization & Machine Learning Toolkit
OPEX	operating expenditure
PC	pine chips
PEMEC	proton exchange membrane electrolysis cells
PR-BM	Peng-Robinson-Boston-Mathias
PS	point source
ReLU	rectified linear unit
RWGS	reverse water-gas shift
ref.	reference
SAF	sustainable aviation fuel
SMR	steam methane reforming
SOEC	solid oxide electrolysis cells
SPK	synthetic paraffinic kerosene
UB	upper bound
VM	volatile matter
WS	wheat straw
wt.	weight

A.2. Set definitions

Set of all components of the system:

$$\mathcal{C} = \{\text{H}_2\text{O}, \text{H}_2\text{O}_{\text{waste}}, \text{Air}, \text{CO}_{2,\text{air}}, \text{CO}_2, \text{Miscanthus}, \text{WheatStraw}, \text{PineChips}, \text{SolidWaste}, \text{H}_2, \text{O}_2, \text{N}_2, \text{CO}, \text{H}_2\text{S}, \text{HCl}, \text{NH}_3, \text{CH}_4, \text{C}_2\text{H}_6, \text{C}_3\text{H}_8, \text{C}_4\text{H}_{10}, \text{C}_5\text{H}_{12}, \text{C}_6\text{H}_{14}, \text{C}_7\text{H}_{16}, \text{C}_8\text{H}_{18}, \text{C}_9\text{H}_{20}, \text{C}_{10}\text{H}_{22}, \text{C}_{11}\text{H}_{24}, \text{C}_{12}\text{H}_{26}, \text{C}_{13}\text{H}_{28}, \text{C}_{14}\text{H}_{30}, \text{C}_{15}\text{H}_{32}, \text{C}_{16}\text{H}_{34}, \text{C}_{17}\text{H}_{36}, \text{C}_{18}\text{H}_{38}, \text{C}_{19}\text{H}_{40}, \text{C}_{20}\text{H}_{42}, \text{C}_{21}\text{H}_{44}, \text{C}_{22}\text{H}_{46}, \text{C}_{23}\text{H}_{48}, \text{C}_{24}\text{H}_{50}, \text{C}_{25}\text{H}_{52}, \text{C}_{26}\text{H}_{54}, \text{C}_{27}\text{H}_{56}, \text{C}_{28}\text{H}_{58}, \text{C}_{29}\text{H}_{60}, \text{C}_{30}\text{H}_{62}, \text{C}_{30+}\}.$$

Set of all source components of the system:

$$\mathcal{C}^{\text{src}} = \{\text{H}_2\text{O}, \text{Air}, \text{CO}_{2,\text{air}}, \text{CO}_2, \text{Miscanthus}, \text{WheatStraw}, \text{PineChips}, \text{CH}_4\} \subseteq \mathcal{C}.$$

Set of different biomass types of the system:

$$\mathcal{C}^{\text{biomass}} = \{\text{Miscanthus}, \text{WheatStraw}, \text{PineChips}\} \subseteq \mathcal{C}.$$

Set of all hydrocarbons (n-alkanes) considered as FT output:

$$\mathcal{C}^{\text{HC}} = \{\text{CH}_4, \text{C}_2\text{H}_6, \text{C}_3\text{H}_8, \text{C}_4\text{H}_{10}, \text{C}_5\text{H}_{12}, \text{C}_6\text{H}_{14}, \text{C}_7\text{H}_{16}, \text{C}_8\text{H}_{18}, \text{C}_9\text{H}_{20}, \text{C}_{10}\text{H}_{22}, \text{C}_{11}\text{H}_{24}, \text{C}_{12}\text{H}_{26}, \text{C}_{13}\text{H}_{28}, \text{C}_{14}\text{H}_{30}, \text{C}_{15}\text{H}_{32}, \text{C}_{16}\text{H}_{34}, \text{C}_{17}\text{H}_{36}, \text{C}_{18}\text{H}_{38}, \text{C}_{19}\text{H}_{40}, \text{C}_{20}\text{H}_{42}, \text{C}_{21}\text{H}_{44}, \text{C}_{22}\text{H}_{46}, \text{C}_{23}\text{H}_{48}, \text{C}_{24}\text{H}_{50}, \text{C}_{25}\text{H}_{52}, \text{C}_{26}\text{H}_{54}, \text{C}_{27}\text{H}_{56}, \text{C}_{28}\text{H}_{58}, \text{C}_{29}\text{H}_{60}, \text{C}_{30}\text{H}_{62}, \text{C}_{30+}\} \subseteq \mathcal{C}.$$

Set of all hydrocarbons (n-alkanes) considered as gasoline fraction:

$$\mathcal{C}^{\text{gasoline}} = \{\text{C}_1\text{H}_4, \text{C}_2\text{H}_6, \text{C}_3\text{H}_8, \text{C}_4\text{H}_{10}, \text{C}_5\text{H}_{12}, \text{C}_6\text{H}_{14}, \text{C}_7\text{H}_{16}\} \subseteq \mathcal{C}.$$

Set of all hydrocarbons (n-alkanes) considered as kerosene fraction:

$$\mathcal{C}^{\text{kerosene}} = \{\text{C}_8\text{H}_{18}, \text{C}_9\text{H}_{20}, \text{C}_{10}\text{H}_{22}, \text{C}_{11}\text{H}_{24}, \text{C}_{12}\text{H}_{26}, \text{C}_{13}\text{H}_{28}, \text{C}_{14}\text{H}_{30}, \text{C}_{15}\text{H}_{32}, \text{C}_{16}\text{H}_{34}\} \subseteq \mathcal{C}.$$

Set of all hydrocarbons (n-alkanes) considered as diesel fraction:

$$\mathcal{C}^{\text{diesel}} = \{\text{C}_{17}\text{H}_{36}, \text{C}_{18}\text{H}_{38}, \text{C}_{19}\text{H}_{40}, \text{C}_{20}\text{H}_{42}, \text{C}_{21}\text{H}_{44}, \text{C}_{22}\text{H}_{46}, \text{C}_{23}\text{H}_{48}, \text{C}_{24}\text{H}_{50}, \text{C}_{25}\text{H}_{52}, \text{C}_{26}\text{H}_{54}, \text{C}_{27}\text{H}_{56}, \text{C}_{28}\text{H}_{58}, \text{C}_{29}\text{H}_{60}, \text{C}_{30}\text{H}_{62}, \text{C}_{30+}\} \subseteq \mathcal{C}.$$

Set of all processes of the system:

$$\mathcal{J} = \{\text{DAC, CS, CRD, Gasification, ATR, AEC, PEMEC, SOEC, RWGS, AGR, FT}\}.$$

Set of all processes of the system represented via an artificial neural network (ANN):

$$\mathcal{J}^{\text{ANN}} = \{\text{Gasification, RWGS, FT}\} \subseteq \mathcal{J}.$$

Set of possible inlet ports of the processes of the system:

$$\mathcal{I} = \{1, 2, 3, 4, 5\}.$$

Set of possible outlet ports of the processes of the system:

$$\mathcal{O} = \{1, 2, 3\}.$$

Set of all existing process inlet ports of the system:

$$\begin{aligned} \mathcal{J}^I = & \{(\text{DAC}, 1), (\text{CS}, 1), (\text{CRD}, 1), (\text{Gasification}, 1), (\text{Gasification}, 2), \\ & (\text{Gasification}, 3), (\text{Gasification}, 4), (\text{Gasification}, 5), (\text{ATR}, 1), (\text{AEC}, 1), \\ & (\text{PEMEC}, 1), (\text{SOEC}, 1), (\text{RWGS}, 1), (\text{AGR}, 1), (\text{FT}, 1) \} \subseteq \mathcal{J} \times \mathcal{I}. \end{aligned}$$

Set of all existing process outlet ports of the system:

$$\begin{aligned} \mathcal{J}^O = & \{(\text{DAC}, 1), (\text{CS}, 1), (\text{CRD}, 1), (\text{CRD}, 2), (\text{Gasification}, 1), (\text{Gasification}, 2), \\ & (\text{Gasification}, 3), (\text{ATR}, 1), (\text{ATR}, 2), (\text{AEC}, 1), (\text{AEC}, 2), (\text{PEMEC}, 1), \\ & (\text{PEMEC}, 2), (\text{SOEC}, 1), (\text{SOEC}, 2), (\text{RGWS}, 1), (\text{RWGS}, 2), (\text{AGR}, 1), \\ & (\text{AGR}, 2), (\text{AGR}, 3), (\text{FT}, 1), (\text{FT}, 2), (\text{FT}, 3) \} \subseteq \mathcal{J} \times \mathcal{O}. \end{aligned}$$

Set of all existing connections between process outlet and inlet ports:

$$\begin{aligned} \mathcal{J}^{OI} = & \{(\text{DAC}, 1, \text{CS}, 1), (\text{DAC}, 1, \text{Gasification}, 3), (\text{DAC}, 1, \text{RWGS}, 1), \\ & (\text{CRD}, 2, \text{Gasification}, 4), (\text{CRD}, 2, \text{ATR}, 1), (\text{Gasification}, 1, \text{AGR}, 1), \\ & (\text{ATR}, 1, \text{AGR}, 1), (\text{ATR}, 2, \text{RWGS}, 1), (\text{AEC}, 1, \text{RWGS}, 1), (\text{AEC}, 1, \text{FT}, 1), \\ & (\text{AEC}, 2, \text{Gasification}, 4), (\text{AEC}, 2, \text{ATR}, 1), (\text{PEMEC}, 1, \text{RGWS}, 1), \\ & (\text{PEMEC}, 1, \text{FT}, 1), (\text{PEMEC}, 2, \text{Gasification}, 4), (\text{PEMEC}, 2, \text{ATR}, 1), \\ & (\text{SOEC}, 1, \text{RWGS}, 1), (\text{SOEC}, 1, \text{FT}, 1), (\text{SOEC}, 2, \text{Gasification}, 4), \\ & (\text{SOEC}, 2, \text{ATR}, 1), (\text{RWGS}, 1, \text{AGR}, 1), (\text{AGR}, 1, \text{FT}, 1), \\ & (\text{AGR}, 2, \text{CS}, 1) \} \subseteq \mathcal{J}^O \times \mathcal{J}^I. \end{aligned}$$

Set of key reaction components of processes that are not represented via an ANN:

$$\mathcal{C}^K = \{(\text{CO}_2, \text{DAC}), (\text{CO}_2, \text{CS}), (\text{N}_2, \text{CRD}), (\text{H}_2, \text{ATR}), (\text{H}_2, \text{AEC}), (\text{H}_2, \text{PEMEC}), (\text{H}_2, \text{SOEC}), (\text{CO}_2, \text{AGR})\} \subseteq \mathcal{C} \times \mathcal{J}.$$

Set of possible heat sources/sinks of the processes considered for possible heat integration:

$$\mathcal{H} = \{1, 2, 3\}.$$

Set of all suitable processes for possible heat integration:

$$\mathcal{J}^{\text{heat}} = \{\text{DAC}, \text{Gasification}, \text{ATR}, \text{SOEC}, \text{RWGS}, \text{FT}\} \subseteq \mathcal{J}.$$

Set of all process heat sources/sinks considered for possible heat integration:

$$\mathcal{J}^{\text{heat,s}} = \{(\text{DAC}, 1), (\text{Gasification}, 1), (\text{Gasification}, 2), (\text{Gasification}, 3), (\text{ATR}, 1), (\text{SOEC}, 1), (\text{RWGS}, 1), (\text{RWGS}, 2), (\text{FT}, 1), (\text{FT}, 2)\} \subseteq \mathcal{J}^{\text{heat}} \times \mathcal{H}.$$

Set of all process heat sources considered for possible heat integration:

$$\mathcal{J}^{\text{heat,hot}} = \{(\text{Gasification}, 2), (\text{Gasification}, 3), (\text{ATR}, 1), (\text{RWGS}, 2), (\text{FT}, 1), (\text{FT}, 2)\} \subseteq \mathcal{J}^{\text{heat,s}}.$$

Set of all process heat sinks considered for possible heat integration:

$$\mathcal{J}^{\text{heat,cold}} = \{(\text{DAC}, 1), (\text{Gasification}, 1), (\text{Gasification}, 2), (\text{SOEC}, 1), (\text{RWGS}, 1)\} \subseteq \mathcal{J}^{\text{heat,s}}.$$

A.3. Parameters

Table A.6.: Specific electricity generation/consumption e_j of processes j that are not represented via an ANN in kW/reference capacity.

process j	reference capacity	e_j / kW/reference capacity	ref.
DAC	1 kg _{CO₂} /h	-0.4	[1]
CS	1 kg _{CO₂} /h	-0.132	[2]
CRD	1 kg _{N₂} /h	-0.12	[3]
ATR	1 kg _{H₂} /h	-0.5413	[4]
AEC	1 kg _{H₂} /h	-50	[3]
PEMEC	1 kg _{H₂} /h	-45.42	[1]
SOEC	1 kg _{H₂} /h	-34.65	[1]
AGR	1 kg _{CO₂} /h	-0.01964	[5]

Table A.7.: Specific heat generation/consumption $q_{(j,h)}$ of process heat source/sink (j,h) where processes are not represented via an ANN in kW/reference capacity.

process heat source/sink (j, h)	reference capacity	$q_{(j,h)}$ / kW/reference capacity	ref.
(DAC,1)	1 kg _{CO₂} /h	-2	[1]
(ATR,1)	1 kg _{H₂} /h	2.369	[6]
(SOEC,1)	1 kg _{H₂} /h	-14	[7]

Table A.8.: Temperature level $T_{(j,h)}$ of process heat source/sink (j, h) where the temperature is not calculated via an ANN in °C.

process heat source/sink (j, h)	$T_{(j,h)} / ^\circ\text{C}$	ref.
(DAC,1)	100	[1]
(ATR,1)	900	[8, 9]
(SOEC,1)	100*	[1]
(Gasification,1)	450	[10]
(Gasification,3)	300	[10]
(RWGS,2)	25	-
(FT,2)	60	-

* It is assumed that most of the heat is required during the evaporation of the water.
The remaining heat to keep the process at operating temperature is negligible [1].

Table A.9.: Specific consumption/production $\nu_{\alpha,j}$ of component α in process j where processes are not represented via an ANN in kg/h/reference capacity.

Table A.10.: Specific CAPEX β_j of processes j that are not represented via an ANN (without AGR) in \$/reference capacity.

process j	reference capacity	β_j / \$/reference capacity	ref.
DAC	1 kg _{CO₂} /h	7,260	[11]
CS	1 kg _{CO₂} /h	490	[2]
CRD	1 kg _{N₂} /h	260	[12]
ATR	1 kg _{H₂} /h	3,500	[2]
AEC	1 kg _{H₂} /h	67,260	[7]
PEMEC	1 kg _{H₂} /h	73,750	[12]
SOEC	1 kg _{H₂} /h	273,600	[7]

Table A.11.: Specific OPEX $\gamma_{\alpha}^{\text{src}}$ of source components/ressources α in \$/kg.

component α	$\gamma_{\alpha}^{\text{src}}$ / \$/kg	ref.
H ₂ O	0.0016	[7]
Air	0	-
CO _{2,air}	0	-
CO ₂	0.029	[7]
Miscanthus	0.18*	[13, 14]
WheatStraw	0.1796*	[13, 14]
PineChips	0.1664*	[13, 14]
CH ₄	0.44	[15]

* Costs are calculated using an average biomass cost of 10\$/GJ from Meys et al. [13] and average higher heating values of miscanthus, wheat straw and pine chips from Nebeská et al. [14].

Table A.12.: Specific CO₂ emissions $\lambda_{\alpha}^{\text{comp}}$ of source components/resources α in kgCO₂-eq/kg.

component α	$\lambda_{\alpha}^{\text{comp}} / \text{kgCO}_{2\text{-eq}}/\text{kg}$	ref.
H ₂ O	0	-
Air	0	-
CO _{2,air}	-1	-
CO ₂	0.120	[7]
Miscanthus	-1.0545*	[16, 17]
WheatStraw	-1.0169*	[16, 17]
PineChips	-1.1855*	[16, 17]
CH ₄	0.39138	[18]

* CO₂ uptakes of different biomass types are calculated based on data from Vassilev et al. [17] and average CO₂ supply chain emissions for biomass of 0.495 kgCO₂/kg_{biomass} from Cumicheo et al. [16] are added to these uptakes.

Table A.13.: Specific OPEX (γ) and CO₂ emissions (λ) of electricity and heat.

parameter	value / unit	ref.
γ^{el}	0.1242 \$/kWh	[19]
γ^{heat}	0.0328 \$/kWh	[7]
λ^{el}	0.36 kgCO ₂ -eq/kWh	[7]
λ^{heat}	0.248 kgCO ₂ -eq/kWh	[7]

Table A.14.: Physical properties (specific energy δ_α and specific CO₂ emissions $\lambda_\alpha^{\text{comp}}$) of hydrocarbons (298.15 K) considered as FT output.

component α	physical property / unit	
	δ_α [20] /	$\lambda_\alpha^{\text{comp}}$ /
	MJ/kg	kgCO ₂ -eq/kg
CH ₄	50.03004471	2.7427
C ₂ H ₆	47.51104436	2.9265
C ₃ H ₈	46.33268113	2.9934
C ₄ H ₁₀	45.71859182	3.0280
C ₅ H ₁₂	44.97473884	3.0492
C ₆ H ₁₄	44.73459093	3.0635
C ₇ H ₁₆	44.55638715	3.0737
C ₈ H ₁₈	44.42010972	3.0815
C ₉ H ₂₀	44.32128104	3.0875
C ₁₀ H ₂₂	44.2368075	3.092
C ₁₁ H ₂₄	44.16563944	3.096
C ₁₂ H ₂₆	44.11030182	3.1
C ₁₃ H ₂₈	44.05871994	3.103
C ₁₄ H ₃₀	44.01796038	3.105
C ₁₅ H ₃₂	43.98084202	3.107
C ₁₆ H ₃₄	43.9462466	3.109
C ₁₇ H ₃₆	43.92096837	3.1105
C ₁₈ H ₃₈	43.89587426	3.1120
C ₁₉ H ₄₀	43.87349335	3.1133
C ₂₀ H ₄₂	43.85293715	3.1145
C ₂₁ H ₄₄	43.69810597	3.1155
C ₂₂ H ₄₆	43.6886146	3.1165
C ₂₃ H ₄₈	43.64913953	3.1174
C ₂₄ H ₅₀	43.67199057	3.1182
C ₂₅ H ₅₂	43.63631662	3.1189
C ₂₆ H ₅₄	43.63064088	3.1200
C ₂₇ H ₅₆	43.59911881	3.1202
C ₂₈ H ₅₈	43.62049943	3.1208
C ₂₉ H ₆₀	43.59148855	3.1214
C ₃₀ H ₆₂	43.58805312	3.1219
C ₃₀₊	43.5	3.1220

B. Model formulation

B.1. Process-specific constraints

In addition to the general constraints of the mixed-integer quadratically constrained programming (MIQCP) formulation, further process-specific constraints are introduced to ensure that only specified components are converted or generated in specific processes. The following subsections list all the process-specific constraints, whereby w describes the mass fraction of a component α within a mass flow and y represents the binary decision variable for the installation of a process j . Thus, in the case of installing a process ($y_j = 1$), the inlet and outlet mass fractions of the individual ports need to sum to one. If the corresponding process is not installed ($y_j = 0$), the mass fractions are consequently set to zero.

B.1.1. Direct air capture (DAC)

$$w_{\text{CO}_2,\text{air},(\text{DAC},1)}^{\text{in}} = y_{\text{DAC}} \quad (\text{B.1})$$

$$w_{\text{CO}_2,(\text{DAC},1)}^{\text{out}} = y_{\text{DAC}} \quad (\text{B.2})$$

B.1.2. Carbon sequestration (CS)

$$w_{\text{CO}_2,(\text{CS},1)}^{\text{in}} = y_{\text{CS}} \quad (\text{B.3})$$

$$w_{\text{CO}_2,(\text{CS},1)}^{\text{out}} = y_{\text{CS}} \quad (\text{B.4})$$

B.1.3. Cryogenic distillation (CRD)

$$w_{\text{Air},(\text{CRD},1)}^{\text{in}} = y_{\text{CRD}} \quad (\text{B.5})$$

$$w_{\text{N}_2,(\text{CRD},1)}^{\text{out}} = y_{\text{CRD}} \quad (\text{B.6})$$

$$w_{\text{O}_2,(\text{CRD},2)}^{\text{out}} = y_{\text{CRD}} \quad (\text{B.7})$$

B.1.4. Gasification

$$w_{\alpha,(\text{Gasification},1)}^{\text{in}} = x_{\alpha} \quad \forall \alpha \in \mathcal{C}^{\text{biomass}} \quad (\text{B.8})$$

$$\sum_{\alpha \in \mathcal{C}^{\text{biomass}}} x_{\alpha} = y_{\text{Gasification}} \quad (\text{B.9})$$

$$w_{\text{H}_2\text{O},(\text{Gasification},2)}^{\text{in}} = y_{\text{Gasification}} \quad (\text{B.10})$$

$$w_{\text{CO}_2,(\text{Gasification},3)}^{\text{in}} = y_{\text{Gasification}} \quad (\text{B.11})$$

$$w_{\text{O}_2,(\text{Gasification},4)}^{\text{in}} = y_{\text{Gasification}} \quad (\text{B.12})$$

$$w_{\text{H}_2\text{O},(\text{Gasification},5)}^{\text{in}} = y_{\text{Gasification}} \quad (\text{B.13})$$

$$\begin{aligned} w_{\text{H}_2,(\text{Gasification},1)}^{\text{out}} + w_{\text{CO},(\text{Gasification},1)}^{\text{out}} + w_{\text{CO}_2,(\text{Gasification},1)}^{\text{out}} + w_{\text{H}_2\text{O}_{\text{waste}},(\text{Gasification},1)}^{\text{out}} \\ + w_{\text{N}_2,(\text{Gasification},1)}^{\text{out}} + w_{\text{HCl},(\text{Gasification},1)}^{\text{out}} + w_{\text{H}_2\text{S},(\text{Gasification},1)}^{\text{out}} \\ + w_{\text{CH}_4,(\text{Gasification},1)}^{\text{out}} = y_{\text{Gasification}} \end{aligned} \quad (\text{B.14})$$

$$w_{\text{CO}_2,(\text{Gasification},2)}^{\text{out}} + w_{\text{H}_2\text{O}_{\text{waste}},(\text{Gasification},2)}^{\text{out}} + w_{\text{NH}_3,(\text{Gasification},2)}^{\text{out}} = y_{\text{Gasification}} \quad (\text{B.15})$$

$$w_{\text{SolidWaste},(\text{Gasification},3)}^{\text{out}} = y_{\text{Gasification}} \quad (\text{B.16})$$

The CAPEX for the gasification process is determined based on the total inlet mass flow using the following equation:

$$K_{\text{Gasification}}^{\text{cap}} = 13,300 \frac{\$}{\text{kg/h}} \cdot \dot{M}_{\text{Gasification}}^{\text{in,tot}}. \quad (\text{B.17})$$

B.1.5. Autothermal reforming (ATR)

For the ATR process, we assume that a second outlet stream can be split from the product gas, which can be sent directly to the RWGS process to increase the CO content:

$$w_{\text{CH}_4,(\text{ATR},1)}^{\text{in}} + w_{\text{H}_2\text{O},(\text{ATR},1)}^{\text{in}} + w_{\text{O}_2,(\text{ATR},1)}^{\text{in}} = y_{\text{ATR}}, \quad (\text{B.18})$$

$$w_{\text{H}_2,(\text{ATR},1)}^{\text{out}} + w_{\text{CO},(\text{ATR},1)}^{\text{out}} + w_{\text{CO}_2,(\text{ATR},1)}^{\text{out}} + w_{\text{H}_2\text{O}_{\text{waste}},(\text{ATR},1)}^{\text{out}} = y_{\text{ATR}}, \quad (\text{B.19})$$

$$w_{\text{H}_2,(\text{ATR},2)}^{\text{out}} + w_{\text{CO}_2,(\text{ATR},2)}^{\text{out}} = y_{\text{ATR}}. \quad (\text{B.20})$$

Due to the unavailability of reliable cost scaling data for the AGR process as a function of process scale, its CAPEX is instead determined based on the total mass flow at the process inlet

$$K_{\text{AGR}}^{\text{cap}} = 243.5 \frac{\$}{\text{kg/h}} \cdot \dot{M}_{\text{AGR}}^{\text{in,tot}}, \quad (\text{B.21})$$

with the cost coefficient derived from the techno-economic data reported by Onel et al. [21].

B.1.6. Electrolysis

$$w_{\text{H}_2\text{O},(j,1)}^{\text{in}} = y_j, \quad \forall j \in \{\text{AEC, PEMEC, SOEC}\} \quad (\text{B.22})$$

$$w_{\text{H}_2,(j,1)}^{\text{out}} = y_j, \quad \forall j \in \{\text{AEC, PEMEC, SOEC}\} \quad (\text{B.23})$$

$$w_{\text{O}_2,(j,2)}^{\text{out}} = y_j, \quad \forall j \in \{\text{AEC, PEMEC, SOEC}\} \quad (\text{B.24})$$

B.1.7. Reverse water-gas shift (RWGS)

$$w_{\text{H}_2,(\text{RWGS},1)}^{\text{in}} + w_{\text{CO}_2,(\text{RWGS},1)}^{\text{in}} = y_{\text{RWGS}} \quad (\text{B.25})$$

$$w_{\text{H}_2,(\text{RWGS},1)}^{\text{out}} + w_{\text{CO}_2,(\text{RWGS},1)}^{\text{out}} + w_{\text{CO},(\text{RWGS},1)}^{\text{out}} + w_{\text{H}_2\text{O}_{\text{waste}},(\text{RWGS},1)}^{\text{out}} = y_{\text{RWGS}} \quad (\text{B.26})$$

$$w_{\text{H}_2\text{O}_{\text{waste}},(\text{RWGS},2)}^{\text{out}} = y_{\text{RWGS}} \quad (\text{B.27})$$

The CAPEX for the RWGS process is determined based on the total inlet mass flow using the following equation:

$$K_{\text{RWGS}}^{\text{cap}} = 2,070 \frac{\$}{\text{kg/h}} \cdot \dot{M}_{\text{RWGS}}^{\text{in,tot}}. \quad (\text{B.28})$$

B.1.8. Acid gas removal (AGR)

Based on Liu et al. [5] we assume a CO₂ capture rate of 62 % (mass-based) for the AGR process. This means that a pure CO₂ outlet stream exits the AGR process via the second outlet port (modelled via Eq. B.31 and Eq. B.32), which can be fed directly to the CS process and sequestered. The remaining CO₂ leaves the system with the other impurities via the boundaries as a sink flow.

$$\begin{aligned} w_{\text{H}_2,(\text{AGR},1)}^{\text{in}} + w_{\text{CO},(\text{AGR},1)}^{\text{in}} + w_{\text{CO}_2,(\text{AGR},1)}^{\text{in}} + w_{\text{H}_2\text{S},(\text{AGR},1)}^{\text{in}} + w_{\text{H}_2\text{O}_{\text{waste}},(\text{AGR},1)}^{\text{in}} \\ + w_{\text{N}_2,(\text{AGR},1)}^{\text{in}} + w_{\text{HCl},(\text{AGR},1)}^{\text{in}} + w_{\text{CH}_4,(\text{AGR},1)}^{\text{in}} = y_{\text{AGR}} \end{aligned} \quad (\text{B.29})$$

$$w_{\text{H}_2,(\text{AGR},1)}^{\text{out}} + w_{\text{CO},(\text{AGR},1)}^{\text{out}} = y_{\text{AGR}} \quad (\text{B.30})$$

$$w_{\text{CO}_2,(\text{AGR},2)}^{\text{out}} = y_{\text{AGR}} \quad (\text{B.31})$$

$$w_{\text{CO}_2,(\text{AGR},2)}^{\text{out}} \dot{M}_{\text{AGR},2}^{\text{out}} = 0.62 \cdot w_{\text{CO}_2,\text{AGR}}^{\text{in,tot}} \dot{M}_{\text{AGR}}^{\text{in,tot}} \quad (\text{B.32})$$

$$\begin{aligned} w_{\text{H}_2\text{S},(\text{AGR},3)}^{\text{out}} + w_{\text{CO}_2,(\text{AGR},3)}^{\text{out}} + w_{\text{N}_2,(\text{AGR},3)}^{\text{out}} + w_{\text{HCl},(\text{AGR},3)}^{\text{out}} + w_{\text{CH}_4,(\text{AGR},3)}^{\text{out}} \\ + w_{\text{H}_2\text{O}_{\text{waste}},(\text{AGR},3)}^{\text{out}} = y_{\text{AGR}} \end{aligned} \quad (\text{B.33})$$

B.1.9. Fischer-Tropsch (FT)

$$w_{\text{H}_2,(\text{FT},1)}^{\text{in}} + w_{\text{CO},(\text{FT},1)}^{\text{in}} = y_{\text{FT}} \quad (\text{B.34})$$

$$\sum_{\alpha \in \mathcal{C}^{\text{HC}}} w_{\alpha,(\text{FT},1)}^{\text{out}} + w_{\text{H}_2\text{O}_{\text{waste}},(\text{FT},1)}^{\text{out}} = y_{\text{FT}} \quad (\text{B.35})$$

$$w_{\text{H}_2,(\text{FT},2)}^{\text{out}} + w_{\text{CO},(\text{FT},2)}^{\text{out}} = y_{\text{FT}} \quad (\text{B.36})$$

$$w_{\text{H}_2\text{O}_{\text{waste}},(\text{FT},3)}^{\text{out}} = y_{\text{FT}} \quad (\text{B.37})$$

The CAPEX for the FT process is determined based on the total inlet mass flow using the following equation:

$$K_{\text{FT}}^{\text{cap}} = 183 \frac{\$}{\text{kg/h}} \cdot \dot{M}_{\text{FT}}^{\text{in,tot}}. \quad (\text{B.38})$$

C. Process flowsheet simulations

C.1. Biomass gasification

The gasification process is simulated for three different types of biomass: miscanthus (MIS), wheat straw (WS), and pine chips (PC). The three types of biomass are characterized by different compositions, as shown in Tab. C.1.

Table C.1.: Proximate and ultimate analysis of different biomass types [17] used for the gasification ANN.

biomass type	proximate analysis				ultimate analysis					
	moisture	VM	FC	ash	C	O	H	N	S	Cl
miscanthus	11.4	81.2	15.8	3.0	47.724	42.7964	5.82	0.388	0.1455	0.1261
wheat straw	10.1	74.8	18.1	7.1	45.8926	39.96558	5.6669	0.6503	0.15793	0.56669
pine chips	7.6	72.4	21.6	6.0	49.632	38.023	5.734	0.47	0.0846	0.0564

C.2. Fischer-Tropsch (FT)

The chain growth probability and the resulting Anderson-Schulz-Flory (ASF) distribution are modeled as a function of reaction pressure, temperature and gas phase composition using an empirical FT reactor model.

In order to establish a relatively simple relationship between the product composition (for the sake of simplicity, we only consider n-alkanes as products) and the reaction conditions for cobalt-catalyzed FT synthesis, we apply an empirical model based on Hamelinck et al. [22]. This model considers product selectivity as a function of the H₂/CO ratio in the syngas, reaction pressure p_{FT} , and reaction temperature T_{FT} [22]. These parameters are linked to the selectivity of products with five and more carbon atoms $S_{\text{C}_{5+}}$ via the following linear equation:

$$S_{\text{C}_{5+}} = 1.7 - 0.0024 \cdot T_{\text{FT}} - 0.088 \cdot \frac{[\text{H}_2]}{[\text{CO}]} + 0.18 \cdot ([\text{H}_2] + [\text{CO}]) + 0.0078 \cdot p_{\text{FT}}, \quad (\text{C.1})$$

where [H₂] and [CO] represent the mole fractions of the two components in the feed gas. The impact of the parameters is evident in this equation. As indicated by the negative sign, an increase in H₂ content and temperature results in a decrease in $S_{\text{C}_{5+}}$, which is

equivalent to the product distribution shifting towards lighter products and an increased methane production. Conversely, an increase in pressure and CO content leads to an increase in heavier products.

The chain growth probability α can be connected to the selectivity $S_{\text{C}_{5+}}$ using the following correlation [22]:

$$\alpha \approx 0.75 - 0.373 \cdot \sqrt{-\log(S_{\text{C}_{5+}})} + 0.25 \cdot S_{\text{C}_{5+}}. \quad (\text{C.2})$$

The mole fractions x_n or mass fractions w_n for all hydrocarbons in the range from five to 30 carbon atoms are then determined by the ASF distribution:

$$x_n = (1 - \alpha) \alpha^{(n-1)}, \quad (\text{C.3})$$

$$w_n = \alpha^{(n-1)} (1 - \alpha)^2 n, \quad (\text{C.4})$$

where n denotes the number of carbon atoms. For hydrocarbons with a chain length of one to four carbon atoms, methane and ethane in particular, empirical measurements deviate from the ASF distribution. While methane formation is often underestimated by the ASF approach, C_2 selectivity is usually overestimated [23]. In order to take this into account, the mass fractions of methane and the C_2 to C_4 hydrocarbons are not calculated according to Eq. C.4. Instead, the selectivity with regard to the short chain products is determined via:

$$S_{\text{C}_{1-4}} = 1 - S_{\text{C}_{5+}}. \quad (\text{C.5})$$

The actual mass fractions are then calculated following de Klerk and adjusted to the selectivity $S_{\text{C}_{1-4}}$ resulting from the process conditions [23]. The reference values for the mass fractions of the C_1 to C_4 components are provided in Tab. C.2.

Table C.2.: Reference mass fractions for the calculation of the FT reactor outlet mass fractions of the C_1 to C_4 components [23].

component	reference mass fraction / wt%
CH_4	5.6
C_2H_6	1.1
C_3H_8	2.067
C_4H_{10}	3.133

The sum of the reference mass fractions of the C_1 to C_4 products (0.119 in this case) is

divided by $S_{C_{1-4}}$ to obtain a correction factor:

$$CF = \frac{0.119}{S_{C_{1-4}}}. \quad (\text{C.6})$$

This correction factor is then multiplied with the reference mass fractions, resulting in the actual mass fractions of the C₁ to C₄ n-alkanes in the reactor outlet.

The original model also includes olefins. They are linked to the n-alkanes by an olefin/paraffin factor. Since only n-alkanes are considered in this work for reasons of simplification and the fraction of olefins in the total product mass is small, the olefins and thus the olefin-paraffin ratio are neglected. The mass fractions of the olefins are simply attributed to the corresponding n-alkanes with the same chain length.

Using the empirical approach described above, the mass fractions of all C₁ to C₃₀ n-alkanes in the outlet of the FT reactor can be calculated as a function of the reaction conditions (gas phase composition, pressure, and temperature). The FT reactor is modeled as a stoichiometric reactor in Aspen Plus®, where all reaction equations of the C₁ to C₃₀ n-alkanes are taken into account [20]. An Excel-calculator block routine is used to determine the product composition based on the empirical model. Unlike mechanistic-kinetic models, the empirical model used in our work does not consider CO conversion as a function of reaction conditions. For this reason, single-pass CO conversion is set at 70 %, based on typical values for cobalt-catalyzed FT synthesis, regardless of reaction conditions [22]. By calculating the mass and mole fractions of the individual products the CO conversion can be allocated proportionally to all the FT synthesis reactions. As a result, the FT Reactor Aspen Plus® simulation not only provides the output composition, but also the heat of reaction released in the reactor. Fig. C.1 shows ASF distributions as output of the FT Aspen Plus® flowsheet simulation based on the empirical reactor model for three sets of reaction conditions.

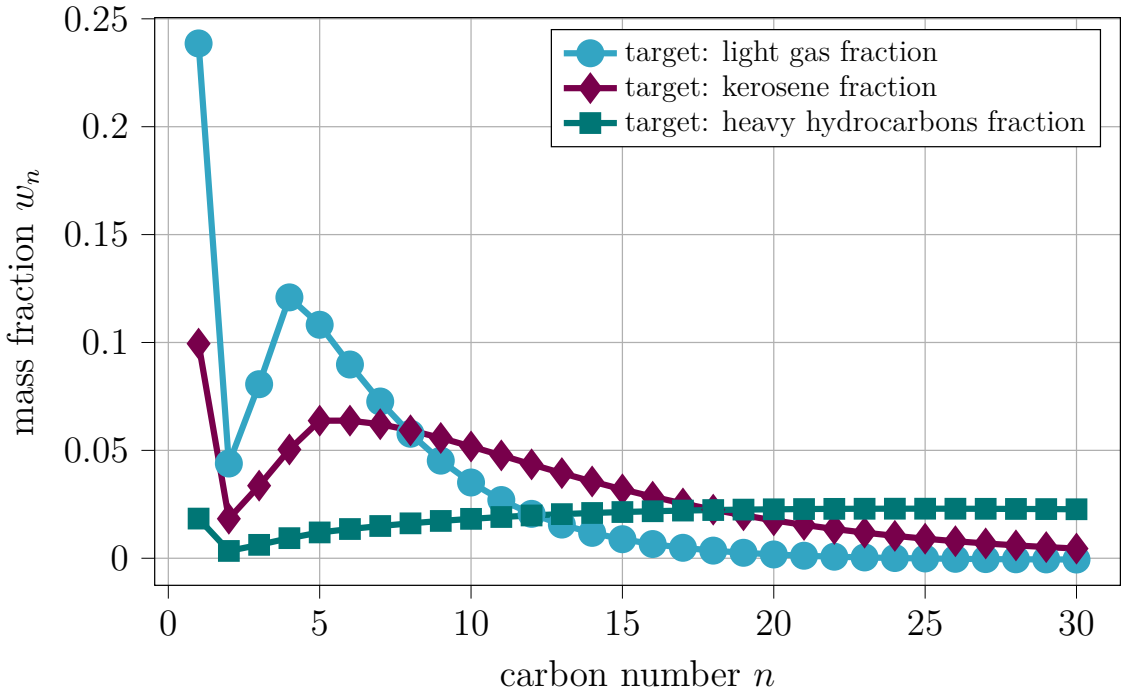


Figure C.1.: Corrected Anderson-Schulz-Flory (ASF) distribution for C_1-C_{30} n-alkanes as output of the Fischer-Tropsch (FT) Aspen Plus® flowsheet simulation using the empirical FT reactor model. The reaction conditions used to target the light gas fraction are: molar $H_2/CO = 2.28$, $T_{FT} = 300^\circ\text{C}$, $p_{FT} = 30$ bar. The reaction conditions used to target the kerosene fraction are: molar $H_2/CO = 1.86$, $T_{FT} = 230^\circ\text{C}$, $p_{FT} = 38$ bar. The reaction conditions used to target the heavy hydrocarbons fraction are: molar $H_2/CO = 1.82$, $T_{FT} = 200^\circ\text{C}$, $p_{FT} = 50$ bar.

D. Artificial neural networks

D.1. Outputs

D.1.1. Gasification

Outputs of the biomass gasification ANN:

- mass flow SCR-GAS/BIOMASS inflow
- H₂ mass fraction SCR-GAS out
- CO mass fraction SCR-GAS out
- CO₂ mass fraction SCR-GAS out
- H₂O mass fraction SCR-GAS out
- N₂ mass fraction SCR-GAS out
- HCl mass fraction SCR-GAS out
- H₂S mass fraction SCR-GAS out
- mass flow SOUR-H₂O/BIOMASS inflow
- CO₂ mass fraction SOUR-H₂O out
- H₂O mass fraction SOUR-H₂O out
- mass flow LP-WATER/BIOMASS inflow
- net work PUMP-H₂O/BIOMASS inflow
- net heating duty HEAT-GAS/BIOMASS inflow
- net heating duty HEAT-H₂O/BIOMASS inflow
- net cooling duty GASIFIER/BIOMASS inflow
- net cooling duty COOL-SG/BIOMASS inflow

D.1.2. Reverse water-gas shift (RWGS)

Outputs of the RWGS ANN:

- mass flow SG-RWGS/TOTAL-IN inflow
- H₂ mass fraction SG-RWGS out
- CO₂ mass fraction SG-RWGS out
- CO mass fraction SG-RWGS out
- net work C-RWGS/TOTAL-IN inflow
- net heating duty HWT-RWGS/TOTAL-IN inflow
- net heating duty RE-RWGS/TOTAL-IN inflow
- net cooling duty CWT-RWGS/TOTAL-IN inflow

D.1.3. Fischer-Tropsch (FT)

Outputs of the FT ANN:

- mass flow FT-C/SYNG-IN inflow
- H₂O mass fraction FT-C out
- C_nH_{2n+2} $\forall n = 1, \dots, 30$ mass fractions FT-C out
- mass flow FT-PURGE/SYNG-IN inflow
- H₂ mass fraction FT-PURGE out
- net work MS-COMP/SYNG-IN inflow
- net cooling duty MS-COMP/SYNG-IN inflow
- net cooling duty FT-REACT/SYNG-IN inflow
- net cooling duty FT-COOL/SYNG-IN inflow

D.2. Hyperparameters

Table D.1.: Hyperparameters of best performing gasification, RWGS, and FT ANNs.

hyperparameter	gasification	RWGS	FT
# hidden ReLU layers	1	1	1
# input neurons	7	2	3
# hidden ReLU neurons	75	25	100
# output neurons*	17	8	38
ℓ^1 regularization coefficient	1×10^{-5}	1×10^{-4}	1×10^{-4}
initial learning rate**	1×10^{-4}	1×10^{-4}	1×10^{-4}
maximum learning rate**	1×10^{-2}	1×10^{-2}	1×10^{-2}
batch size	40	15	5
epochs	1000	1000	1000

*Linear activation function is used for all the output neurons.

**A cyclic learning rate, implemented in the Python package Keras, is used for ANN training [24]. The step size, which determines the duration of a single cycle for the cyclic learning rate, is determined by doubling the number of training data points and dividing it by the batch size.

D.3. Parity plots

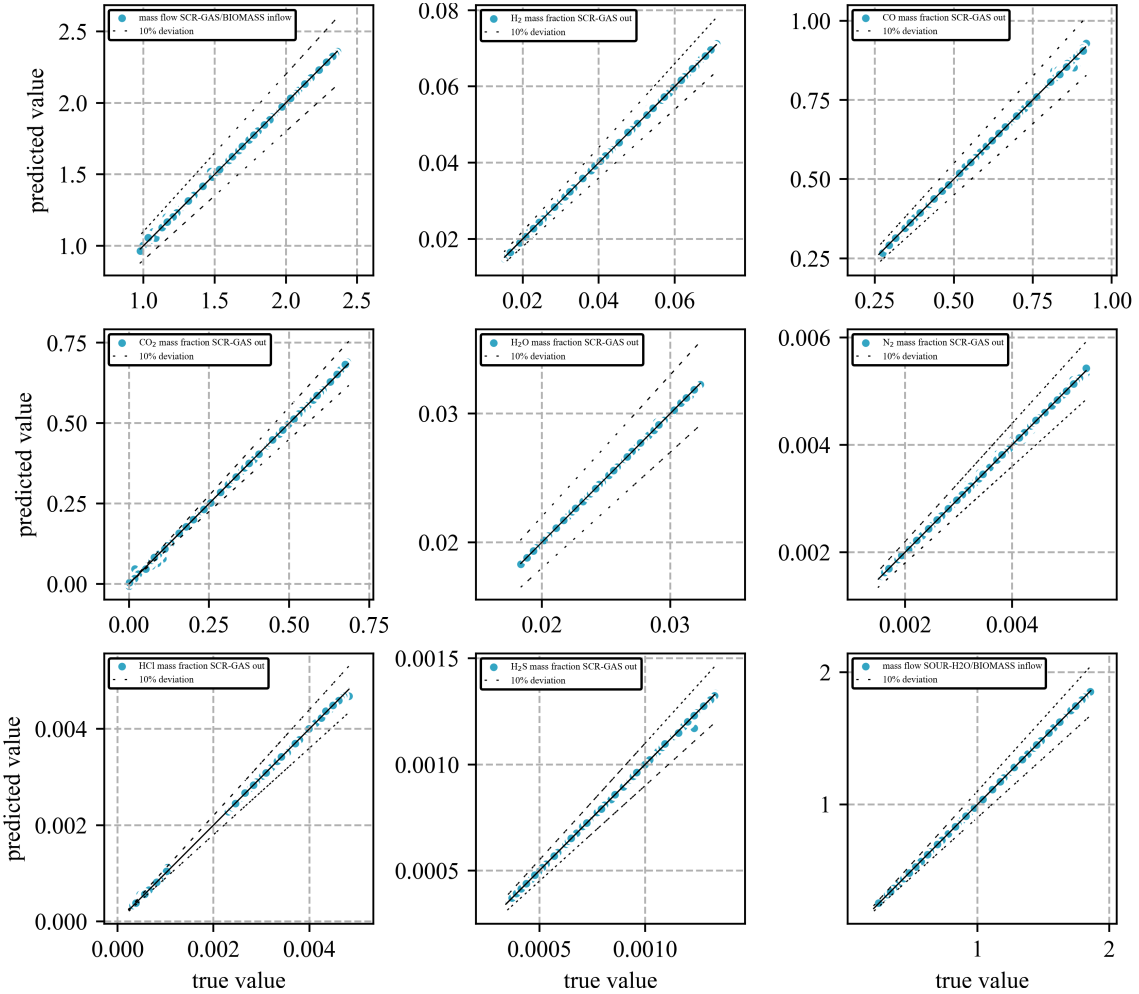


Figure D.1.: Parity plots of the biomass gasification artificial neural network. Test data points are shown for the first nine neural network outputs.

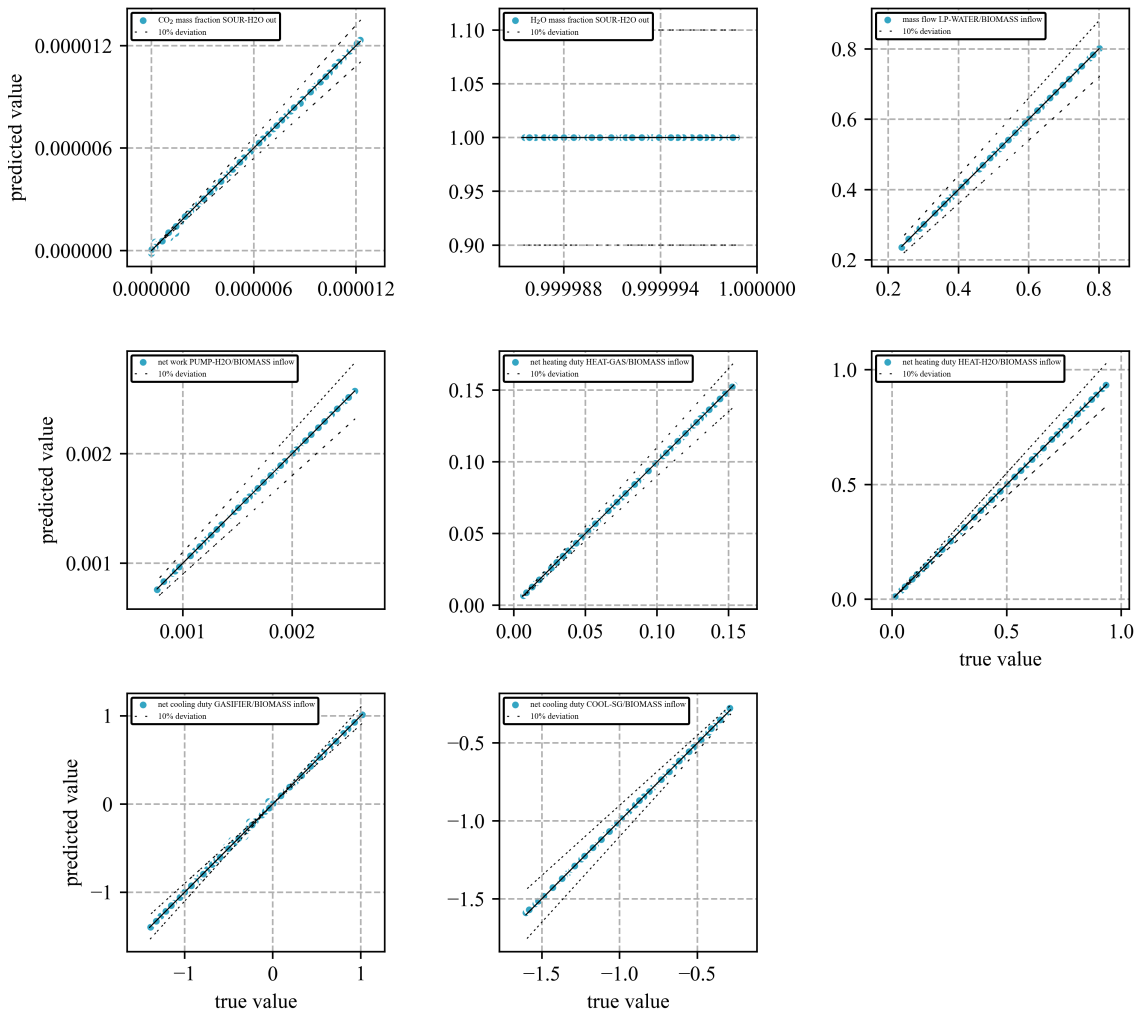


Figure D.2.: Parity plots of the biomass gasification artificial neural network. Test data points are shown for the last eight neural network outputs.

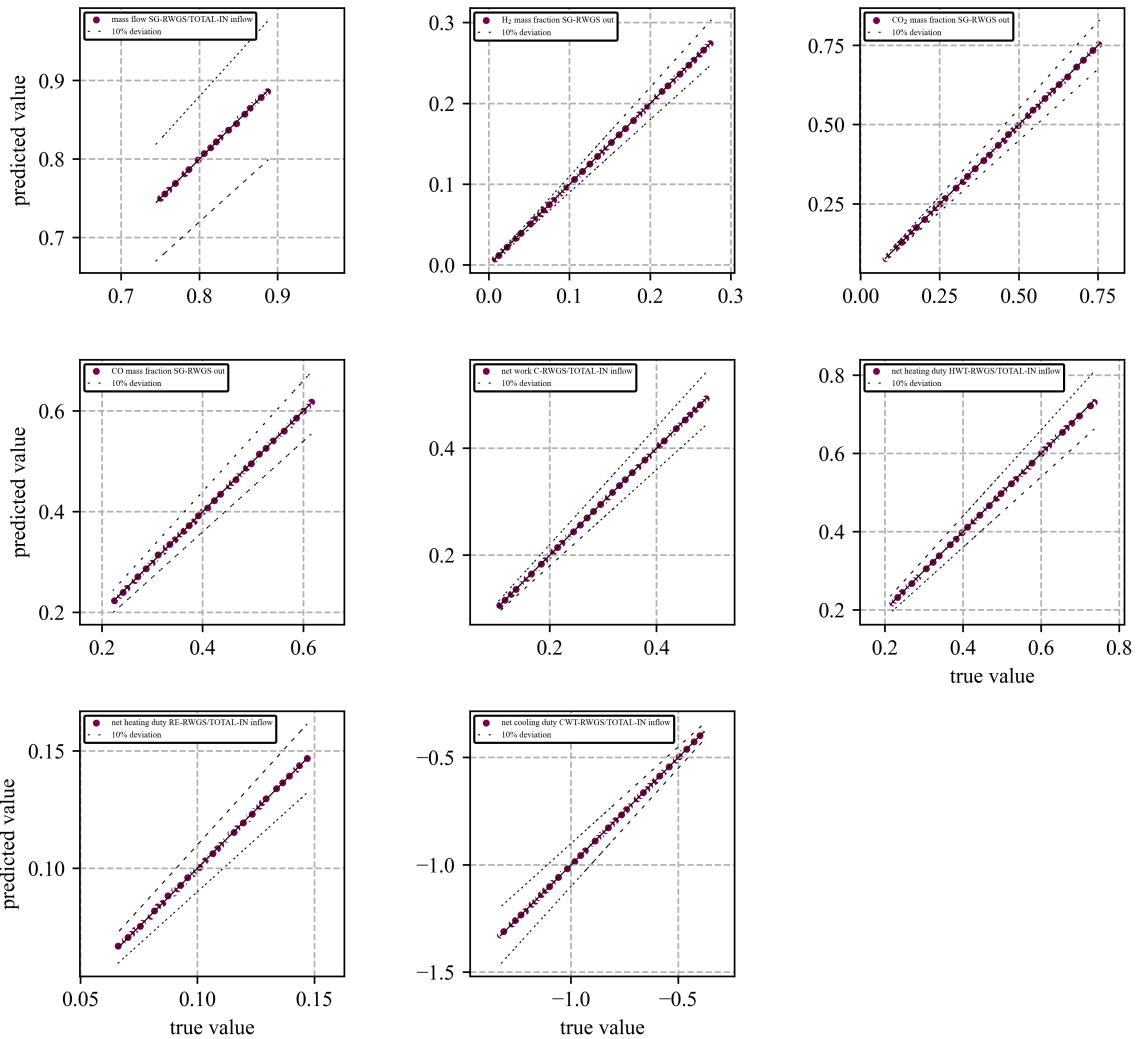


Figure D.3.: Parity plots of the reverse water-gas shift artificial neural network. Test data points are shown for all neural network outputs.

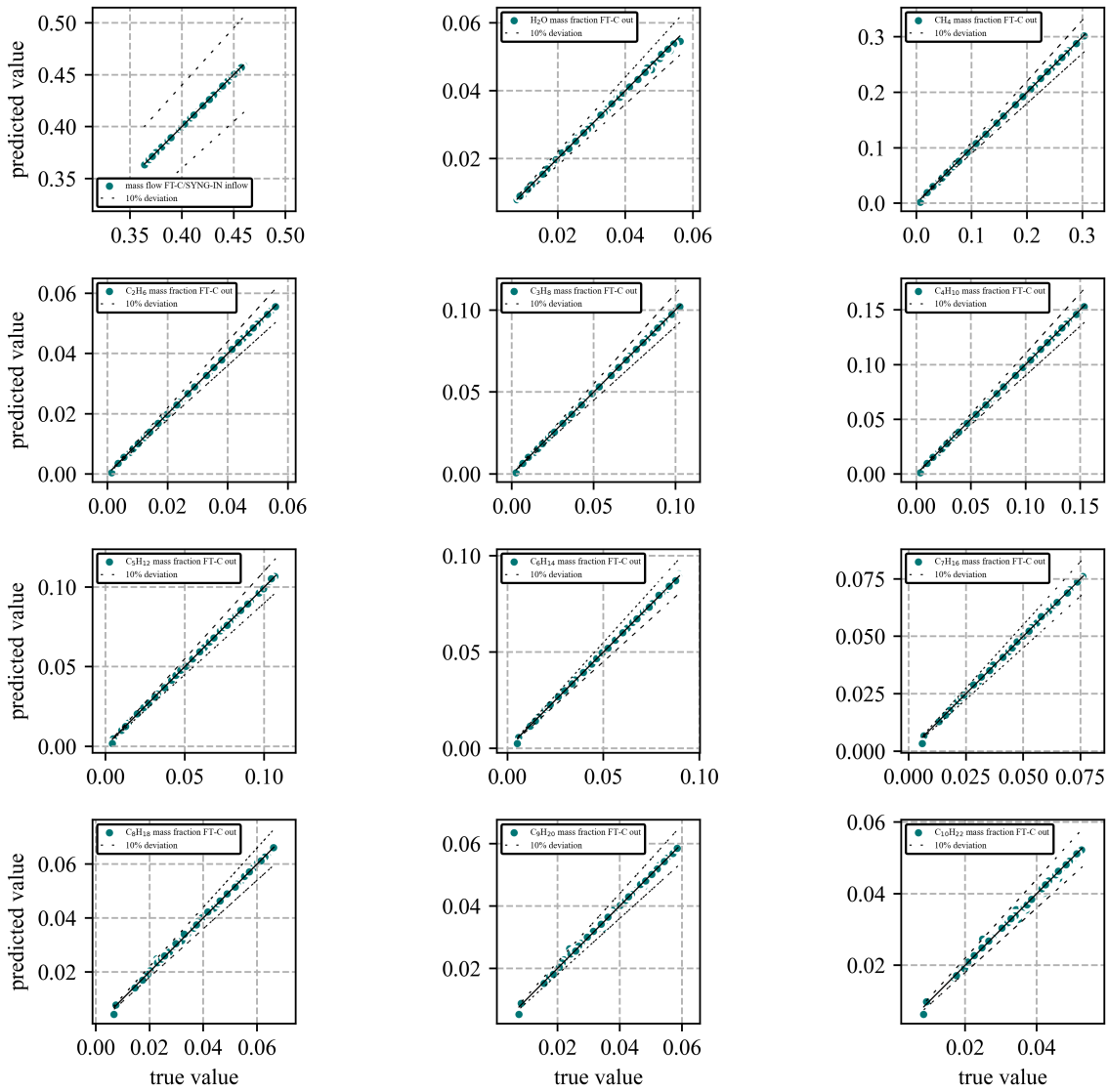


Figure D.4.: Parity plots of the Fischer-Tropsch artificial neural network. Test data points are shown for the first twelve neural network outputs.

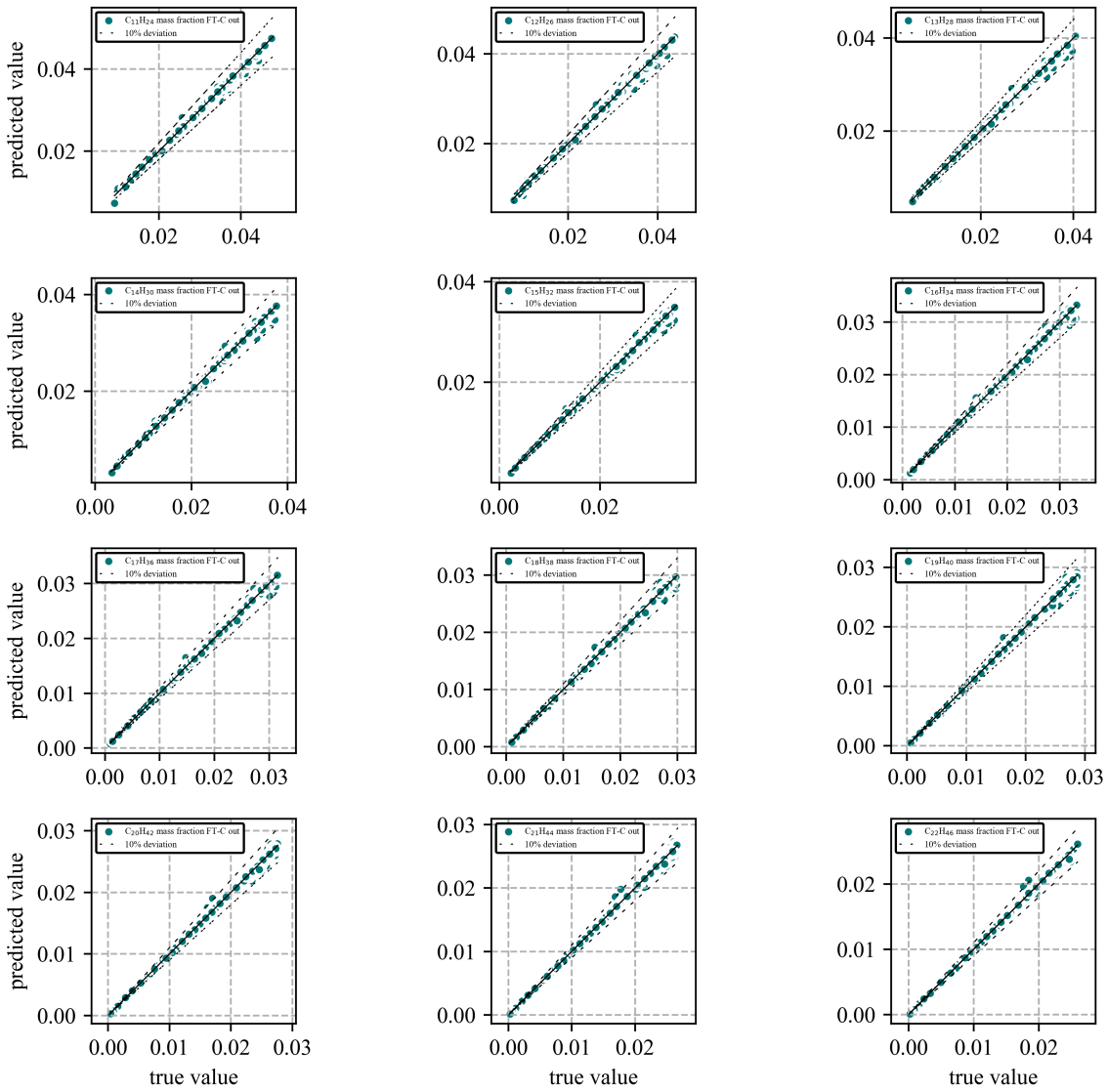


Figure D.5.: Parity plots of the Fischer-Tropsch artificial neural network. Test data points are shown for outputs 13-24.

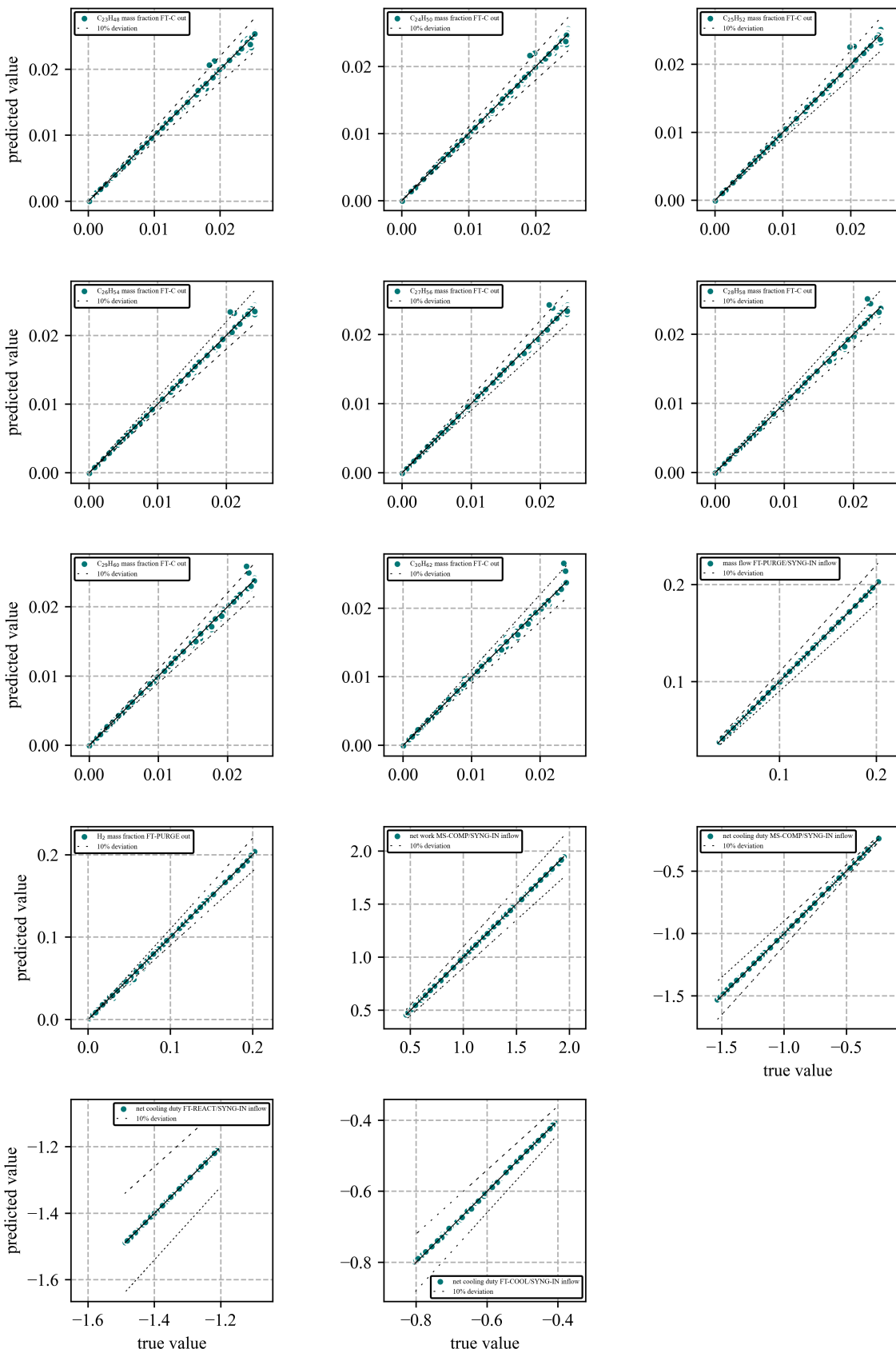


Figure D.6.: Parity plots of the Fischer-Tropsch artificial neural network. Test data points are shown for outputs 25-38.

D.4. Embedding of artificial neural networks in the superstructure optimization framework

To embed the trained ANNs in the MIQCP superstructure optimization, the decision variables describing the ANN inputs and outputs (denoted by $f_{j,(input,i)}^{\text{ANN}}$ and $f_{j,(output,o)}^{\text{ANN}}$ for process j and input/output i/o) are linked to the decision variables in the superstructure via equality constraints. All of these equality constraints for embedding the ANNs for the gasification, RWGS and FT process are listed below. Since not all ANN outputs are dependent on the mass flow entering the flowsheets (e.g., component mass fractions within outlet streams), the inlet mass flow is not used as input for the ANNs in order to avoid numerical problems during optimization. Instead, the inlet mass flow is optimized as a decision variable of the MIQCP formulation. The ANN outputs depending on this mass flow (e.g., work and heat requirements) are determined by ratios with respect to this inlet mass flow (see also outputs of the trained ANNs based on the Aspen Plus® flowsheet simulations in Section D.1).

D.4.1. Gasification

$$x_{\text{Miscanthus}} = f_{\text{Gasification},(\text{input},1)}^{\text{ANN}}, \quad (\text{D.1})$$

$$x_{\text{WheatStraw}} = f_{\text{Gasification},(\text{input},2)}^{\text{ANN}}, \quad (\text{D.2})$$

$$x_{\text{PineChips}} = f_{\text{Gasification},(\text{input},3)}^{\text{ANN}}, \quad (\text{D.3})$$

$$\dot{M}_{(\text{Gasification},2)}^{\text{in}} = f_{\text{Gasification},(\text{input},4)}^{\text{ANN}} \dot{M}_{(\text{Gasification},1)}^{\text{in}}, \quad (\text{D.4})$$

$$\dot{M}_{(\text{Gasification},3)}^{\text{in}} = f_{\text{Gasification},(\text{input},5)}^{\text{ANN}} \dot{M}_{(\text{Gasification},1)}^{\text{in}}, \quad (\text{D.5})$$

$$\dot{M}_{(\text{Gasification},4)}^{\text{in}} = f_{\text{Gasification},(\text{input},6)}^{\text{ANN}} \dot{M}_{(\text{Gasification},1)}^{\text{in}}, \quad (\text{D.6})$$

$$T_{(\text{Gasification},2)} = f_{\text{Gasification},(\text{input},7)}^{\text{ANN}}, \quad (\text{D.7})$$

$$\dot{M}_{(\text{Gasification},1)}^{\text{out}} = f_{\text{Gasification},(\text{output},1)}^{\text{ANN}} \dot{M}_{(\text{Gasification},1)}^{\text{in}}, \quad (\text{D.8})$$

$$w_{\text{H}_2,(\text{Gasification},1)}^{\text{out}} = y_{\text{Gasification}} f_{\text{Gasification},(\text{output},2)}^{\text{ANN}}, \quad (\text{D.9})$$

$$w_{\text{CO},(\text{Gasification},1)}^{\text{out}} = y_{\text{Gasification}} f_{\text{Gasification},(\text{output},3)}^{\text{ANN}}, \quad (\text{D.10})$$

$$w_{\text{CO}_2,(\text{Gasification},1)}^{\text{out}} = y_{\text{Gasification}} f_{\text{Gasification},(\text{output},4)}^{\text{ANN}}, \quad (\text{D.11})$$

$$w_{\text{H}_2\text{O}_{\text{waste}},(\text{Gasification},1)}^{\text{out}} = y_{\text{Gasification}} f_{\text{Gasification},(\text{output},5)}^{\text{ANN}}, \quad (\text{D.12})$$

$$w_{\text{N}_2,(\text{Gasification},1)}^{\text{out}} = y_{\text{Gasification}} f_{\text{Gasification},(\text{output},6)}^{\text{ANN}}, \quad (\text{D.13})$$

$$w_{\text{HCl},(\text{Gasification},1)}^{\text{out}} = y_{\text{Gasification}} f_{\text{Gasification},(\text{output},7)}^{\text{ANN}}, \quad (\text{D.14})$$

$$w_{\text{H}_2\text{S},(\text{Gasification},1)}^{\text{out}} = y_{\text{Gasification}} f_{\text{Gasification},(\text{output},8)}^{\text{ANN}}, \quad (\text{D.15})$$

$$\dot{M}_{(\text{Gasification},2)}^{\text{out}} = f_{\text{Gasification},(\text{output},9)}^{\text{ANN}} \dot{M}_{(\text{Gasification},1)}^{\text{in}}, \quad (\text{D.16})$$

$$w_{\text{CO}_2,(\text{Gasification},2)}^{\text{out}} = y_{\text{Gasification}} f_{\text{Gasification},(\text{output},10)}^{\text{ANN}}, \quad (\text{D.17})$$

$$w_{\text{H}_2\text{O}_{\text{waste}},(\text{Gasification},2)}^{\text{out}} = y_{\text{Gasification}} f_{\text{Gasification},(\text{output},11)}^{\text{ANN}}, \quad (\text{D.18})$$

$$\dot{M}_{(\text{Gasification},5)}^{\text{in}} = f_{\text{Gasification},(\text{output},12)}^{\text{ANN}} \dot{M}_{(\text{Gasification},1)}^{\text{in}}, \quad (\text{D.19})$$

$$\dot{W}_{\text{Gasification}} = f_{\text{Gasification},(\text{output},13)}^{\text{ANN}} \dot{M}_{(\text{Gasification},1)}^{\text{in}}, \quad (\text{D.20})$$

$$\dot{W}_{\text{Gasification}} \leq 0 \quad (\text{D.21})$$

The heat demand required for the first heat integration port of the gasification process is comprised of the heat demand for heating the gasification agents to 450 °C and the heat demand for the biomass decomposition step. The ratio of the heat requirement for the decomposition step to the biomass inlet flow is approximately constant, other heat requirements are calculated according to the gasification ANN:

$$\begin{aligned} \dot{Q}_{(\text{Gasification},1)} &= \left(f_{\text{Gasification},(\text{output},14)}^{\text{ANN}} + f_{\text{Gasification},(\text{output},15)}^{\text{ANN}} \right. \\ &\quad \left. - 1.552 \right) \dot{M}_{(\text{Gasification},1)}^{\text{in}}, \end{aligned} \quad (\text{D.22})$$

$$\dot{Q}_{(\text{Gasification},2)} = f_{\text{Gasification},(\text{output},16)}^{\text{ANN}} \dot{M}_{(\text{Gasification},1)}^{\text{in}}, \quad (\text{D.23})$$

$$\dot{Q}_{(\text{Gasification},3)} = f_{\text{Gasification},(\text{output},17)}^{\text{ANN}} \dot{M}_{(\text{Gasification},1)}^{\text{in}}. \quad (\text{D.24})$$

D.4.2. Reverse water-gas shift (RWGS)

$$T_{(\text{RWGS},1)} = f_{\text{RWGS},(\text{input},1)}^{\text{ANN}}, \quad (\text{D.25})$$

$$w_{\text{H}_2,(\text{RWGS},1)}^{\text{in}} = y_{\text{RWGS}} f_{\text{RWGS},(\text{input},2)}^{\text{ANN}}, \quad (\text{D.26})$$

$$\dot{M}_{(\text{RWGS},1)}^{\text{out}} = f_{\text{RWGS},(\text{output},1)}^{\text{ANN}} \dot{M}_{(\text{RWGS},1)}^{\text{in}}, \quad (\text{D.27})$$

$$w_{\text{H}_2,(\text{RWGS},1)}^{\text{out}} = y_{\text{RWGS}} f_{\text{RWGS},(\text{output},2)}^{\text{ANN}}, \quad (\text{D.28})$$

$$w_{\text{CO}_2,(\text{RWGS},1)}^{\text{out}} = y_{\text{RWGS}} f_{\text{RWGS},(\text{output},3)}^{\text{ANN}}, \quad (\text{D.29})$$

$$w_{\text{CO},(\text{RWGS},1)}^{\text{out}} = y_{\text{RWGS}} f_{\text{RWGS},(\text{output},4)}^{\text{ANN}}, \quad (\text{D.30})$$

$$\dot{W}_{\text{RWGS}} = f_{\text{RWGS},(\text{output},5)}^{\text{ANN}} \dot{M}_{(\text{RWGS},1)}^{\text{in}}, \quad (\text{D.31})$$

$$\dot{W}_{\text{RWGS}} \leq 0, \quad (\text{D.32})$$

$$\dot{Q}_{(\text{RWGS},1)} = \left(f_{\text{RWGS},(\text{output},6)}^{\text{ANN}} + f_{\text{RWGS},(\text{output},7)}^{\text{ANN}} \right) \dot{M}_{(\text{RWGS},1)}^{\text{in}}, \quad (\text{D.33})$$

$$\dot{Q}_{(\text{RWGS},2)} = f_{\text{RWGS},(\text{output},8)}^{\text{ANN}} \dot{M}_{(\text{RWGS},1)}^{\text{in}} \quad (\text{D.34})$$

D.4.3. Fischer-Tropsch (FT)

$$T_{(\text{FT},1)} = f_{\text{FT},(\text{input},1)}^{\text{ANN}}, \quad (\text{D.35})$$

$$p_{\text{FT}} = f_{\text{FT},(\text{input},2)}^{\text{ANN}}, \quad (\text{D.36})$$

$$w_{\text{H}_2,(\text{FT},1)}^{\text{in}} = y_{\text{FT}} f_{\text{FT},(\text{input},3)}^{\text{ANN}}, \quad (\text{D.37})$$

$$\dot{M}_{(\text{FT},1)}^{\text{out}} = f_{\text{FT},(\text{output},1)}^{\text{ANN}} \dot{M}_{(\text{FT},1)}^{\text{in}}, \quad (\text{D.38})$$

$$w_{\text{H}_2\text{O}_{\text{waste}},(\text{FT},1)}^{\text{out}} = y_{\text{FT}} f_{\text{FT},(\text{output},2)}^{\text{ANN}}, \quad (\text{D.39})$$

$$w_{\text{C}_n\text{H}_{2n+2},(\text{FT},1)}^{\text{out}} = y_{\text{FT}} f_{\text{FT},(\text{output},n+2)}^{\text{ANN}} \quad \forall n = 1, \dots, 30, \quad (\text{D.40})$$

$$\dot{M}_{(\text{FT},2)}^{\text{out}} = f_{\text{FT},(\text{output},33)}^{\text{ANN}} \dot{M}_{(\text{FT},1)}^{\text{in}}, \quad (\text{D.41})$$

$$w_{\text{H}_2,(\text{FT},2)}^{\text{out}} = y_{\text{FT}} f_{\text{FT},(\text{output},34)}^{\text{ANN}}, \quad (\text{D.42})$$

$$\dot{W}_{\text{FT}} = f_{\text{FT},(\text{output},35)}^{\text{ANN}} \dot{M}_{(\text{FT},1)}^{\text{in}}, \quad (\text{D.43})$$

$$\dot{W}_{\text{FT}} \leq 0, \quad (\text{D.44})$$

$$\dot{Q}_{(\text{FT},1)} = \left(f_{\text{FT},(\text{output},36)}^{\text{ANN}} + f_{\text{FT},(\text{output},37)}^{\text{ANN}} \right) \dot{M}_{(\text{FT},1)}^{\text{in}}, \quad (\text{D.45})$$

$$\dot{Q}_{(\text{FT},2)} = f_{\text{FT},(\text{output},38)}^{\text{ANN}} \dot{M}_{(\text{FT},1)}^{\text{in}} \quad (\text{D.46})$$

E. Results

E.1. CO₂ abatement costs

Table E.1.: CO₂ abatement costs, specific CO₂ emissions, and specific cost for Pareto optimal designs on the curve for specific kerosene costs vs. CO₂ emissions (Fig. 7). Counting starts from the right of the Pareto curve (the first point corresponds to the design with the lowest costs and highest CO₂ emissions and the sixth point belongs to the design with the highest costs and lowest CO₂ emissions). CO₂ abatement costs are always calculated in relation to our fossil ATR reference design.

design number	CO ₂ abatement costs / \$/t _{CO_2}	specific CO ₂ emissions / kg _{CO_2} /kg _{kerosene}	specific cost / \$/kg _{kerosene}
1	-	4.47	0.79
2	211	3.14	1.07
3	246	1.76	1.46
4	379	0.27	2.38
5	440	-0.98	3.18
6	486	-2.22	4.04

Table E.2.: Specific CO₂ emissions, specific cost, and CO₂ abatement costs for various cases with regard to carbon sequestration, CO₂ footprints, and GHG emission targets. CO₂ abatement costs are always calculated in relation to our fossil ATR reference design. Results are generated excluding the fossil ATR process.

case	sequestration permitted	supply chain emissions biomass	CO ₂ emissions electricity and heat	net zero target	specific CO ₂ emissions / kgCO ₂ /kgkerosene	specific cost / \$/kgkerosene	CO ₂ abatement costs / \$/tCO ₂
1	✓	✓	✓	✗	3.74	1.82	1,408.68
2	✓	✓	✓	✓	0	2.58	399.04
3	✓	✓	✗	✗	1.54	1.82	350.86
4	✓	✓	✗	✓	0	1.95	258.03
5	✓	✗	✓	✗	2.29	1.82	472.23
6	✓	✗	✓	✓	0	2.09	290.92
7	✓	✗	✗	✗	0	1.82	234.87
8	✓	✗	✗	✓	0	1.82	234.87
9	✗	✓	✓	✗	3.74	1.82	1,408.68
10	✗	✓	✓	✓		infeasible	
11	✗	✗	✓	✗	2.29	1.82	472.23
12	✗	✗	✓	✓		infeasible	
13	✗	✓	✗	✗	1.54	1.82	350.86
14	✗	✓	✗	✓	0	4.49	844.74
15	✗	✗	✗	✗	0	1.82	234.87
16	✗	✗	✗	✓	0	1.82	234.87

E.2. Pareto-optimal solutions

E.2.1. Cost vs. biomass usage

Fig. E.1 shows the Pareto curve and the corresponding C and H sources for specific kerosene cost vs. biomass usage, excluding the fossil ATR process and without any restrictions on CO₂ emissions. The specific cost ranges from 1.82 \$/kg_{kerosene} (no restrictions on biomass) to 3.52 \$/kg_{kerosene} (no use of biomass permitted). With increasing restrictions on the amount of biomass, C from point sources and H from electrolysis are used.

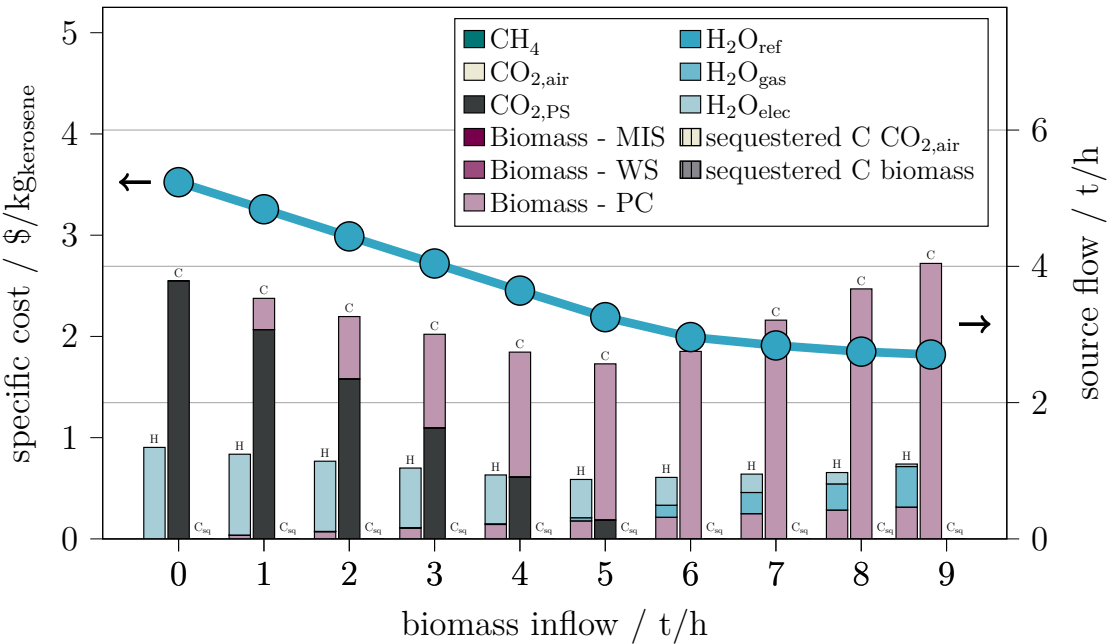


Figure E.1.: Pareto-optimal designs for specific kerosene cost vs. biomass usage (left y-axis). The bars represent the source flows for carbon (C) and hydrogen (H) entering the system (right y-axis). The third bar shows sequestered carbon (C_{sq}) either from CO₂ from the air or from biomass. Results are generated **excluding the fossil autothermal reforming (ATR) process and without any restrictions on CO₂ emissions**. (PS: point source; MIS: miscanthus; WS: wheat straw; PC: pine chips; ref: reforming; gas: gasification; elec: electrolysis).

Fig. E.2 shows the Pareto curve and the corresponding C and H sources for specific kerosene cost vs. biomass usage, excluding the fossil ATR process, external CO₂ from point sources, and without any restrictions on CO₂ emissions. Compared to Fig. E.1, C is now provided via DAC with increasing restrictions on biomass use. The specific cost ranges from 1.82 \$/kg_{kerosene} (no restrictions on biomass) to 4.14 \$/kg_{kerosene} (no use of biomass permitted). The higher costs arise due to the fact that CO₂ from DAC is more expensive than CO₂ from point sources.

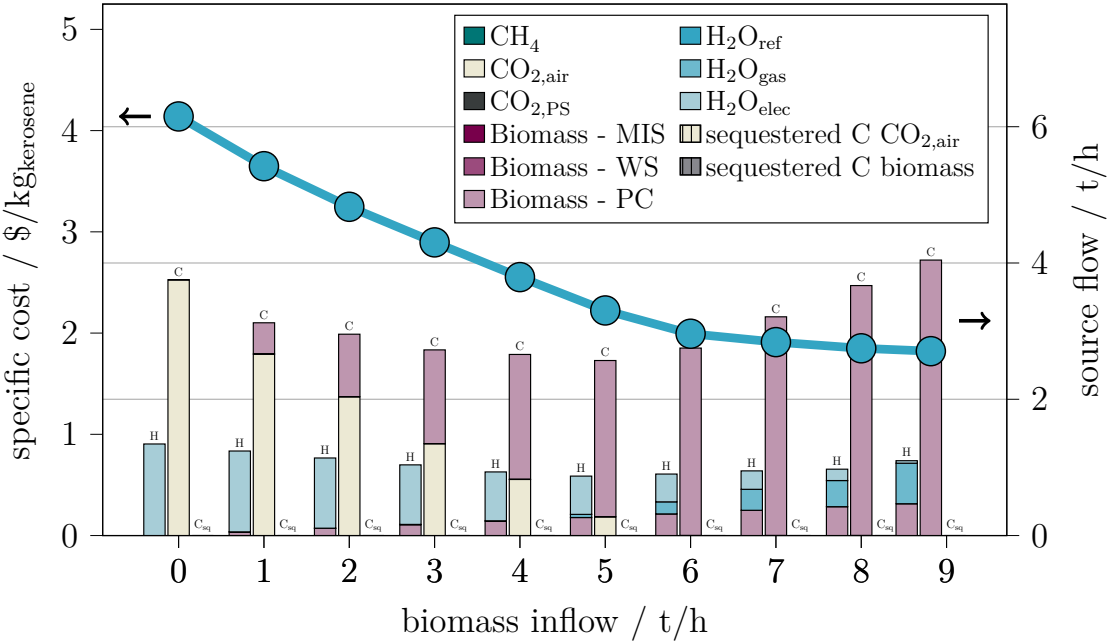


Figure E.2.: Pareto-optimal designs for specific kerosene cost vs. biomass usage (left y-axis). The bars represent the source flows for carbon (C) and hydrogen (H) entering the system (right y-axis). The third bar shows sequestered carbon (C_{sq}) either from CO₂ from the air or from biomass. Results are generated **excluding the fossil autothermal reforming (ATR) process, external CO₂ from point sources, and without any restrictions on CO₂ emissions**. (PS: point source; MIS: miscanthus; WS: wheat straw; PC: pine chips; ref: reforming; gas: gasification; elec: electrolysis).

Fig. E.3 shows the Pareto curve and the corresponding C and H sources for specific kerosene cost vs. biomass usage, excluding the fossil ATR process. Additionally, CO_2 emissions are set to $0 \text{ kg}_{\text{CO}_2}/\text{kg}_{\text{kerosene}}$. The specific cost ranges from $2.58 \$/\text{kg}_{\text{kerosene}}$ (no restrictions on biomass) to $11 \$/\text{kg}_{\text{kerosene}}$ (no use of biomass permitted). This cost increase is driven by the additional need for carbon sequestration (due to the high CO_2 emissions associated with the provision of electricity for water electrolysis) to achieve the net-zero target.

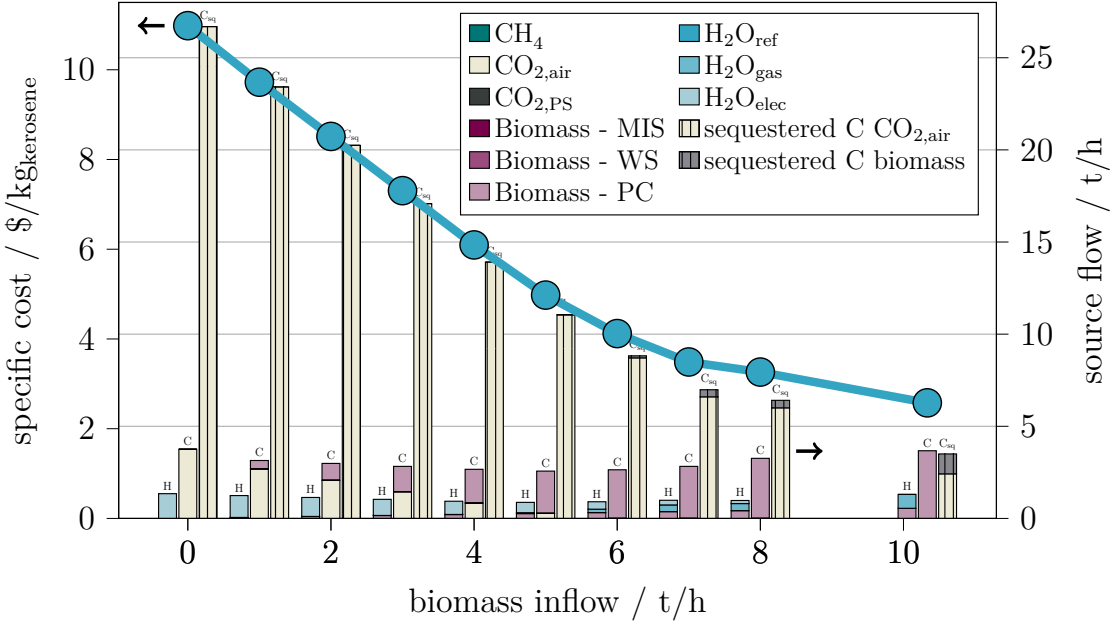


Figure E.3.: Pareto-optimal designs for specific kerosene cost vs. biomass usage (left y-axis). The bars represent the source flows for carbon (C) and hydrogen (H) entering the system (right y-axis). The third bar shows sequestered carbon (C_{sq}) either from CO_2 from the air or from biomass. Results are generated **excluding the fossil autothermal reforming (ATR) process**. CO_2 emissions are set to $0 \text{ kg}_{\text{CO}_2}/\text{kg}_{\text{kerosene}}$. (PS: point source; MIS: miscanthus; WS: wheat straw; PC: pine chips; ref: reforming; gas: gasification; elec: electrolysis).

E.2.2. Cost vs. CO₂ emissions

Fig. E.4 shows the Pareto curve and the corresponding C and H sources for specific kerosene cost vs. specific CO₂ emissions, excluding the fossil ATR and the gasification process. The specific cost ranges from 3.52 \$/kg_{kerosene} (no restrictions on CO₂ emissions) to 12.5 \$/kg_{kerosene} ($-2.22 \text{ kgCO}_2/\text{kg}_{\text{kerosene}}$). In all cases, H is produced by electrolysis, while C is initially obtained from point sources and enters the system via DAC as emissions are increasingly restricted. Due to the high electricity requirements of electrolysis, the heat requirements of DAC, and the associated CO₂ footprints, it is necessary to sequester a large amount of C from the air in order to achieve the emission targets. This leads to a drastic rise in specific cost for carbon negative kerosene compared to the biomass-based route.

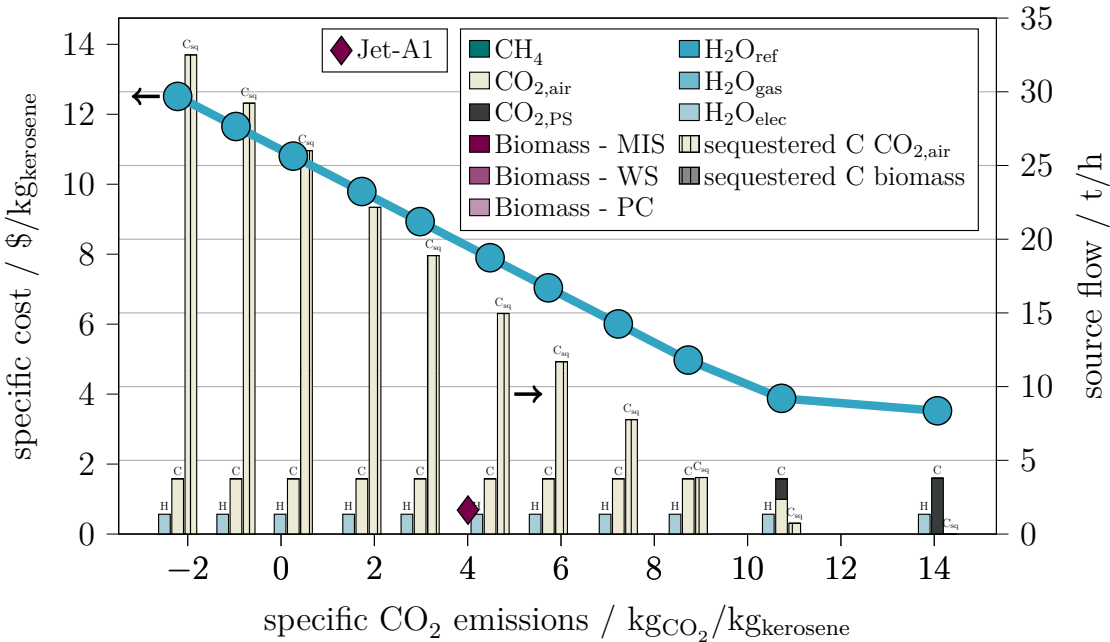


Figure E.4.: Pareto-optimal designs for specific kerosene cost vs. specific CO₂ emissions (left y-axis). The bars represent the source flows for carbon (C) and hydrogen (H) entering the system (right y-axis). The third bar shows sequestered carbon (C_{seq}) either from CO₂ from the air or from biomass. Results are generated **excluding the fossil autothermal reforming (ATR) process and the gasification process**. (PS: point source; MIS: miscanthus; WS: wheat straw; PC: pine chips; ref: reforming; gas: gasification; elec: electrolysis).

Fig. E.5 shows the Pareto curve and the corresponding C and H sources for specific kerosene cost vs. specific CO_2 emissions, excluding the fossil ATR and the gasification process. Furthermore, CO_2 emissions related to the provision of electricity and heat are set to $0 \text{ kg}_{\text{CO}_2\text{-eq}}/\text{kWh}$. The specific cost range from $3.52 \$/\text{kg}_{\text{kerosene}}$ (no restrictions on CO_2 emissions) to $4.46 \$/\text{kg}_{\text{kerosene}}$ ($-2.22 \text{ kg}_{\text{CO}_2}/\text{kg}_{\text{kerosene}}$). The sources for C and H are in any case the same as in Fig. E.4. However, the cost curve is significantly flatter, as the CO_2 footprints of electricity and heat are neglected, reducing the amount of C that needs to be sequestered to achieve the emission targets.

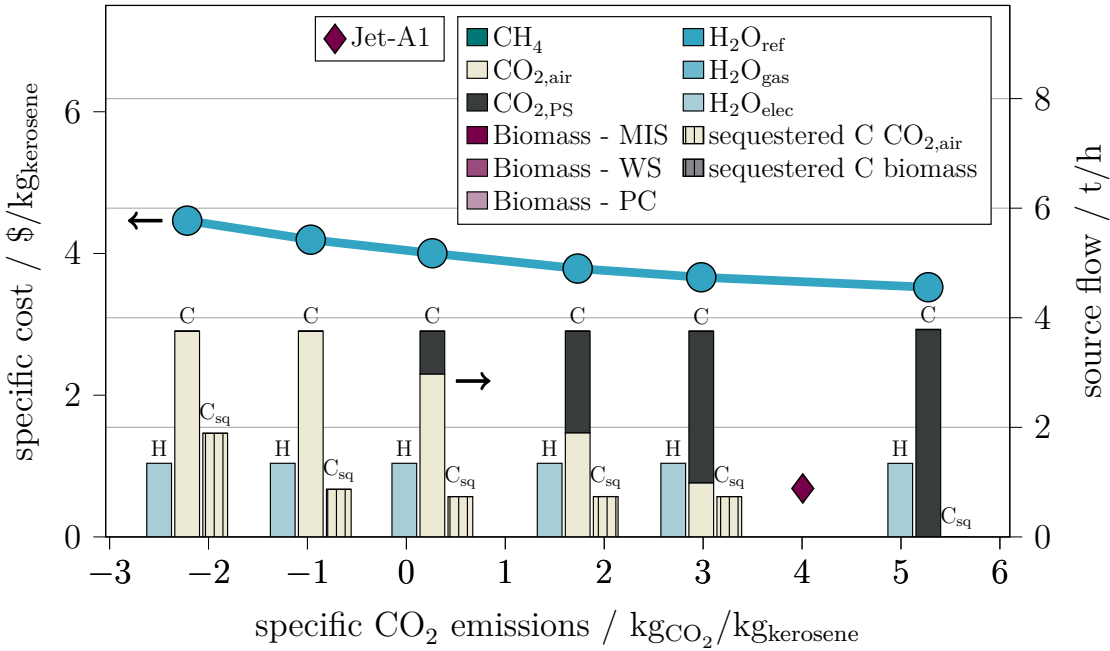


Figure E.5.: Pareto-optimal designs for specific kerosene cost vs. specific CO_2 emissions (left y-axis). The bars represent the source flows for carbon (C) and hydrogen (H) entering the system (right y-axis). The third bar shows sequestered carbon (C_{sq}) either from CO_2 from the air or from biomass. Results are generated **excluding the fossil autothermal reforming (ATR) process and the gasification process. Furthermore, CO_2 emissions related to the provision of electricity and heat are set to $0 \text{ kg}_{\text{CO}_2\text{-eq}}/\text{kWh}$.** (PS: point source; MIS: miscanthus; WS: wheat straw; PC: pine chips; ref: reforming; gas: gasification; elec: electrolysis).

References

- [1] T. Svitnič and K. Sundmacher. “Renewable methanol production: Optimization-based design, scheduling and waste-heat utilization with the FluxMax approach”. In: *Applied Energy* 326 (2022), p. 120017. ISSN: 0306-2619. DOI: [10.1016/j.apenergy.2022.120017](https://doi.org/10.1016/j.apenergy.2022.120017).
- [2] C. D. Demirhan, W. W. Tso, J. B. Powell, and E. N. Pistikopoulos. “A multi-scale energy systems engineering approach towards integrated multi-product network optimization”. In: *Applied Energy* 281 (2021), p. 116020. ISSN: 0306-2619. DOI: [10.1016/j.apenergy.2020.116020](https://doi.org/10.1016/j.apenergy.2020.116020).
- [3] M. J. Palys, I. Mitrai, and P. Daoutidis. “Renewable hydrogen and ammonia for combined heat and power systems in remote locations: Optimal design and scheduling”. In: *Optimal Control Applications and Methods* (2021), pp. 1–20. ISSN: 0143-2087. DOI: [10.1002/oca.2793](https://doi.org/10.1002/oca.2793).
- [4] A. O. Oni, K. Anaya, T. Giwa, G. Di Lullo, and A. Kumar. “Comparative assessment of blue hydrogen from steam methane reforming, autothermal reforming, and natural gas decomposition technologies for natural gas-producing regions”. In: *Energy Conversion and Management* 254 (2022), p. 115245. ISSN: 0196-8904. DOI: [10.1016/j.enconman.2022.115245](https://doi.org/10.1016/j.enconman.2022.115245).
- [5] X. Liu, S. Yang, Z. Hu, and Y. Qian. “Simulation and assessment of an integrated acid gas removal process with higher CO₂ capture rate”. In: *Computers & Chemical Engineering* 83 (2015), pp. 48–57. ISSN: 0098-1354. DOI: [10.1016/j.compchemeng.2015.01.008](https://doi.org/10.1016/j.compchemeng.2015.01.008).
- [6] T. Svitnič, K. Beer, K. Sundmacher, and M. Böcher. “Optimal design of a sector-coupled renewable methanol production amid political goals and expected conflicts: Costs vs. land use”. In: *Sustainable Production and Consumption* 44 (2024), pp. 123–150. ISSN: 23525509. DOI: [10.1016/j.spc.2023.12.003](https://doi.org/10.1016/j.spc.2023.12.003).
- [7] A. Gonzalez-Garay, C. Heuberger-Austin, X. Fu, M. Klokkenburg, D. Zhang, A. van der Made, and N. Shah. “Unravelling the potential of sustainable aviation fuels to decarbonise the aviation sector”. In: *Energy & Environmental Science* 15.8 (2022), pp. 3291–3309. ISSN: 1754-5692. DOI: [10.1039/D1EE03437E](https://doi.org/10.1039/D1EE03437E).

- [8] P. Kenkel, T. Wassermann, and E. Zondervan. “Biogas Reforming as a Precursor for Integrated Algae Biorefineries: Simulation and Techno-Economic Analysis”. In: *Processes* 9.8 (2021), p. 1348. ISSN: 2227-9717. DOI: 10.3390/pr9081348.
- [9] J. Kim, J. Park, M. Qi, I. Lee, and I. Moon. “Process Integration of an Autothermal Reforming Hydrogen Production System with Cryogenic Air Separation and Carbon Dioxide Capture Using Liquefied Natural Gas Cold Energy”. In: *Industrial & Engineering Chemistry Research* 60.19 (2021), pp. 7257–7274. ISSN: 0888-5885. DOI: 10.1021/acs.iecr.0c06265.
- [10] D. Yang, P. Balaprakash, and S. Leyffer. “Modeling design and control problems involving neural network surrogates”. In: *Computational Optimization and Applications* 83.3 (2022), pp. 759–800. DOI: 10.1007/s10589-022-00404-9.
- [11] C. Ganzer and N. Mac Dowell. “A comparative assessment framework for sustainable production of fuels and chemicals explicitly accounting for intermittency”. In: *Sustainable Energy & Fuels* 4.8 (2020), pp. 3888–3903. ISSN: 2398-4902. DOI: 10.1039/C9SE01239G.
- [12] K. H. R. Rouwenhorst, P. M. Krzywda, N. E. Benes, G. Mul, and L. Lefferts. “Ammonia, 4. Green Ammonia Production”. In: *Ullmann's Encyclopedia of Industrial Chemistry*. 7. edition, release 2015. Weinheim and Wiley online library: Wiley-VCH, 2010, pp. 1–20. ISBN: 3527306730. DOI: 10.1002/14356007.w02_w02.
- [13] R. Meys, A. Kätelhön, M. Bachmann, B. Winter, C. Zibunas, S. Suh, and A. Bardow. “Achieving net-zero greenhouse gas emission plastics by a circular carbon economy”. In: *Science* 374.6563 (2021), pp. 71–76. DOI: 10.1126/science.abg9853.
- [14] D. Nebeská, J. Trögl, D. Žofková, A. Voslařová, J. Štojdl, and V. Pidlisnyuk. “Calorific values of Miscanthus x giganteus biomass cultivated under suboptimal conditions in marginal soils”. In: *Studia Oecologica* 13.1 (2020), pp. 61–67. ISSN: 1802-212X. DOI: 10.21062/ujep/429.2020/a/1802-212x/so/13/1/61.
- [15] Trading Economics. *EU Natural Gas TTF - Price - Chart - Historical Data - News*. 30.04.2025. URL: <https://tradingeconomics.com/commodity/eu-natural-gas>.
- [16] C. Cumicheo, N. Mac Dowell, and N. Shah. “Natural gas and BECCS: A comparative analysis of alternative configurations for negative emissions power generation”. In: *International Journal of Greenhouse Gas Control* 90 (2019), p. 102798. ISSN: 1750-5836. DOI: 10.1016/j.ijggc.2019.102798.
- [17] S. V. Vassilev, D. Baxter, L. K. Andersen, and C. G. Vassileva. “An overview of the chemical composition of biomass”. In: *Fuel* 89.5 (2010), pp. 913–933. ISSN: 0016-2361. DOI: 10.1016/j.fuel.2009.10.022.

- [18] C. D. Demirhan, W. W. Tso, J. B. Powell, and E. N. Pistikopoulos. “Sustainable ammonia production through process synthesis and global optimization”. In: *AICHE Journal* 65.7 (2019), e16498. DOI: 10.1002/aic.16498.
- [19] S. Voß, S. Bube, and M. Kaltschmitt. “Hybrid Biomass- and Electricity-Based Kerosene Production-A Techno-Economic Analysis”. In: *Energy & Fuels* 38.6 (2024), pp. 5263–5278. ISSN: 0887-0624. DOI: 10.1021/acs.energyfuels.3c04876.
- [20] Aspen Technology Inc. *Aspen Plus*. 30.04.2024. URL: <https://www.aspentechn.com/en/products/engineering/aspen-plus>.
- [21] O. Onel, A. M. Niziolek, J. A. Elia, R. C. Baliban, and C. A. Floudas. “Biomass and Natural Gas to Liquid Transportation Fuels and Olefins (BGTL+C2_C4): Process Synthesis and Global Optimization”. In: *Industrial & Engineering Chemistry Research* 54.1 (2015), pp. 359–385. ISSN: 0888-5885. DOI: 10.1021/ie503979b.
- [22] C. Hamelinck, A. Faaij, H. den Uil, and H. Boerrigter. “Production of FT transportation fuels from biomass; technical options, process analysis and optimisation, and development potential”. In: *Energy* 29.11 (2004), pp. 1743–1771. ISSN: 0360-5442. DOI: 10.1016/j.energy.2004.01.002.
- [23] A. de Klerk. *Fischer-Tropsch Refining*. Wiley, 2011. ISBN: 9783527326051. DOI: 10.1002/9783527635603.
- [24] KerasTeam. *Keras: Deep Learning for humans*. 30.04.2025. URL: <https://keras.io/>.